Lehigh University
Lehigh Preserve

Theses and Dissertations

2017

Experimental and Computational Investigation of Composite Beam Response to Fire

Amy Kordosky
Lehigh University

Follow this and additional works at: http://preserve.lehigh.edu/etd

Part of the Civil and Environmental Engineering Commons

Recommended Citation

Kordosky, Amy, "Experimental and Computational Investigation of Composite Beam Response to Fire" (2017). *Theses and Dissertations*. 2670.
http://preserve.lehigh.edu/etd/2670

This Thesis is brought to you for free and open access by Lehigh Preserve. It has been accepted for inclusion in Theses and Dissertations by an authorized administrator of Lehigh Preserve. For more information, please contact preserve@lehigh.edu.

www.manaraa.com

Experimental and Computational Investigation of Composite Beam Response to Fire

By Amy Kordosky

Advised by Dr. Spencer Quiel

A Thesis

Presented to the Graduate and Research Committee

Of Lehigh University

In Candidacy for the Degree of

Master of Science

In Structural Engineering

Lehigh University

May 2017

المنارة للاستشارات

www.manaraa.com

This thesis is accepted and approved in partial fulfillment of the requirements for the Master of Science.

Date:

Thesis Advisor:

Chairperson of Department:

www.manaraa.com

Table of Contents

www.manaraa.com

المنارة للاستشارات
www.manaraa.com

List of Tables

المنارة للاستشارات
www.manaraa.com

List of Figures

www.manaraa.com

المنارة للاستشارات
www.manaraa.com

المنارة للاستشارات
www.manaraa.com

Abstract

This thesis presents three experimental studies on composite floor beams in fire that were performed in the Lehigh University ATLSS Furnace. The experiments include a predesigned W8x10 beam with limited existing damage subject to a realistic parametric fire curve with a decay phase, and two W12x26 beams – one bare steel and one insulated with a spray on fire resistant material - designed and tested with an E119 standard fire curve. The complete design and record of the tests are provided, including data on specimen temperatures and deflections.

SAFIR 2016 was used to model the systems thermal and structural behavior at various levels of intensity. 2D beam, 3D beam, and 3D shell models were created to test the level of accuracy and predictability of the models. The 2D structural models were proven to be incapable of predicting accurate behavior of a composite system. MATLAB 2015 was used to verify temperature predictions using a three lumped mass calculation approach, and was shown to equal or exceed the performance of the thermal finite element models.

A parametric study was conducted using the results from the two W12x26 test beams. The lengths of these beams were extended from the 11’-0” able to be accommodated in the furnace out to 15-0”’, 20’-0”, 25’-0”, and 30’-0” to study how the realistic lengths change the behavior of the tests. Validated SAFIR 3D beam and shell models were used to predict behavior, and show the differences and values between the two types of models.

www.manaraa.com

1.0 Introduction

Steel as a material is particularly susceptible to losses in strength and stiffness when subjected to fire. Combined with the restraint of thermal expansion, these effects lead to decreased performance at elevated temperature conditions. Also, steel members are relatively thin in comparison to concrete or wood members, making them more susceptible to heat quickly due to having lower thermal mass. Steel structures have historically and will continue to be a primary focus area in fire resistant building design.

Structural damage by fire is not a new concept, but performance based design techniques in response to fire is a relatively young field in the United States. Generally, a prescriptive approach is used by designers to satisfy fire rating requirements based upon standard fire tests. As an industry, there is a need to move towards performance based design to save time, material, and money in the design and construction of steel framed buildings. Typical performance-based approaches, such as those discussed by Buchanan (2002), Johann et al. (2005), and Rini and Lamont (2008) among others, have outlined basic tools and strategies for fire selection, heat transfer, and structural behavior.

The current state of practice prescribes beam ratings based on restrained or unrestrained, loaded or unloaded, and thermal or structural criteria. Many designers find it difficult to apply these criteria to a realistic structure. Fire protection for a beam that is designated as unrestrained and evaluated for thermal criteria only is generally considered to produce the most conservative design; this evaluation says very little, however, about the structural capacity or performance of that assembly during a fire. This all-or-nothing approach allows very little flexibility in the design. Performance based design provides the option to

المنارة للاستشارات

www.manaraa.com

engineer the system according to the fire exposure and tailor the passive fire protection as needed per a range of design objectives.

Generally, beams and columns require the highest fire ratings in a building, followed by floors and roofs (Gewain et al., 2003). Secondary framing members are currently protected from fire in most steel buildings. This can be done by various methods from active and passive fire protection techniques. Spray on fire resistant material (SFRM) is a common way for steel composite floor beams to be protected from extreme temperature, but the process can be expensive and time consuming. The current state of practice designs fire protection for beams using a standard fire curve which doesn't consider the ignition of active fire protection or the decay of the fire. Incorporating realistic fire curves into a performance based design of fire protection has the potential to decrease or even eliminate passive fire protection on filler floor beams. Fire protection could also be increased in some cases in order to stay above a particular damage threshold on service critical buildings like emergency centers or hospitals.

Composite floor systems are commonly used in building design because they provide more strength and stiffness than a non-composite system. The composite action between the steel beam and concrete slab allows the unit to effectively act as one cross-section, increasing the flexural capacity and stiffness of the floor system. During a fire, the concrete slab acts as a heat sink, and protects the top flange of the steel beam from heating uniformly with the rest of the beam. This action induces a thermal gradient along the depth of the beam. A thru-depth thermal gradient also emerges in other locations of a building, like a perimeter column, where one or two faces of the column are exposed to ambient air while the others are directly exposed to the fire. Current standard practice uses the maximum temperature of the steel as

المنارة للاستشارات
www.manaraa.com

an evaluation metric in the standard test, but most calculations focus on the average temperature of the steel uniformly distributed. However, many critical members experience a temperature gradient. This gradient causes the members to act as beam columns, carrying both axial load and moment along their length (Garlock and Quiel, 2007). Plastic capacity envelopes for combined axial load and moment can also experience significant warping (Garlock and Quiel 2008). Since these members are typically not designed for the unexpected combinations of axial load and moment, the elements can experience structural issues during a fire. As such, current prescriptive methods may be overly conservative and inadequate in predicting time of failure and realistic damage mechanisms in composite beams.

Large full scale tests on a composite steel-framed building were performed in the Cardington Lab Facility in 2000. As a result of these tests, it was recommended that more comprehensive parametric studies on composite structures under fire be performed as a continuation of the Cardington tests (The University of Edinburgh, 2000). This thesis will fulfill Cardington’s call to action, and will include a description of the three tests performed in the ATLSS Research Laboratory located at Lehigh University, the models created and verified by the test data, and a parametric study of the behavior of composite beams in fire using real building conditions. This thesis will incorporate 2D beam, 3D beam, and 3D shell models created with SAFIR 2016 (Franssen, 2005) that capably demonstrate composite behavior both thermally and structurally, thus creating new insight on the readiness of performance-based approaches for the current practice of structural fire design. SAFIR uses uncoupled analyses of, first, a thermal model of each member exposed to fire and, second, a structural model of the frame composed of those members.

www.manaraa.com

The remainder of this thesis consists of six chapters. Chapter 2 discusses past research by others that is relevant to this project. Chapter 3 will introduce the experimental facilities and test setup at Lehigh University's ATLSS Laboratory that were used for this project. Chapter 4 presents the experimental and computational work done for a W8x10 composite beam subject to a realistic fire curve, which accounts for the deployment of active fire protection and includes a realistic decay phase. Chapter 5 presents the design, testing, modeling, and analysis of two W12x26 beams, one as unprotected and the other with passive fire protection. It includes detailed comparisons of specimen temperature and structural behavior to various levels of predicted outcomes. Chapter 6 outlines a parametric study that illustrates how realistic boundary conditions, gravity loading, and span lengths affect the behavior of the composite floor system. This evaluation will compare how these systems would be rated using a prescriptive and performance based approach. Lastly, Chapter 7 concludes this thesis, summarizes the final outcomes of the studies, and presents future directions to build upon the experiments and current findings.

www.manaraa.com

2.0 Background

As shown to follow, much of the past research that has been performed on composite floor beams in fire either hasn't accounted for the slab, hasn't incorporated 3D models, or hasn't considered realistic fire curves with a decay phase. Typically, structural fire research on composite floor systems in steel buildings uses the ASTM E119 standard fire curve (ASTM, 2014) as the idealized representation of the fire's temperature-time history. Some studies have taken a more realistic approach to representing the fire. For example, Chang et al. (2005) used a parametric fire curve with a decay phase, which was then used as input for 2D finite element models to evaluate beam-to-column connection performance. This study will also consider a real fire curve with a decay phase in Chapter 4 to experimentally demonstrate composite floor beam response. Models using 3D beam and shell elements are then used to more realistically predict behavior and potential failure.

Research on composite beam systems under fire will often include the concrete slab as modeled thermally, but not structurally. In those studies, the concrete slab is used to induce a thermal gradient through the depth of the floor but is neglected during the structural analysis. The structural benefits to the floor's fire-induced performance are thus ignored. Ghojel and Wong (2005) developed equations regarding the heat transfer between the steel and concrete to create an accurate heat-transfer model within a composite beam. Moss et al. (2004) modeled both a steel and composite beam against various end conditions and fire loads to indicate which beams experienced better performance at elevated temperatures. Banerjee (2012) incorporates the slab into the thermal model to see how it affects the temperature gradient and rise of the steel.

المنارة للاستشارات
www.manaraa.com

Bailey (2004) discusses slab behavior when steel perimeter beams are protected and steel non-perimeter beams are unprotected. The paper established a new design method that accounts for the membrane action in the slab and beam system together, and emphasizes the slab's significant role in the composite floor beam analysis. Bailey's goal was to protect the required beams, and leave the rest unprotected in order to reduce weight and construction time, and potentially reduce construction costs. Lamont et al. (2007) enhanced this idea by performing a case study to show a design approach to engineer the fire protection on the secondary framing beams in an office building. The E119 standard fire curve was used along with two parametric fire curves to see how the secondary beams would behave in different fire scenarios, and were designed according to this behavior. They concluded that some of the beams required fire protection, where others did not, based upon their placement throughout the building frame.

Ellobody (2011) developed a 3D finite element model to investigate the behavior of unprotected steel composite slim floor beams exposed to various fire curves. The model was validated by comparison to test data - 48 beams were analyzed, and the results were tabulated to evaluate the degree of damage as a function of the fire curve.

Wang et al. (2016) tested two beams that were the same other than their percent composite ratios. Although some differences occurred in the steel concrete interface throughout the test, both beams failed at similar times and exhibited similar behaviors. The study showed that the percentage of composite action of the beam at ambient temperature does not play a large role during the fire. The steel beam heats up quicker than the concrete slab, allowing the composite percentage to increase with temperature.

www.manaraa.com

Usmani (2001) explains many fundamental relationships and responses of composite beams subject to temperature rise, but does not further the conversation from beams to full structures, or show how the behavioral responses would change in these scenarios. Johann et al. (2006) lays out an approach to performance based design of fire protection for a structural system. The process is laid out in flow charts that provide a step-by-step list of tasks in order to arrive at a fully functional fire resistant design. However, Johann et al. does not give the specifics of how to fulfill each step, and more research and understanding is needed to accurately impose this model into a real building design. Chapter 6 of this thesis describes how to analyze a beam in a realistic building scenario in order to fulfill realistic performance based design requirements.

Various research has been done on the effects of thermal gradients on steel structures. Garlock & Quiel (2007) examined the change in steel section mechanics due to thermal gradient. That study showed that the effective centroid of a steel cross-section will migrate towards the cooler part of the section due to the increasingly reduced stiffness and strength of the steel at the hotter portions. This shift caused additional bending moment in the section because the location of the axial load application (assumed at the geometric centroid) is now eccentric to the gradient-induced effective centroid. The study analyzed both beams and columns, therefore examining thermal gradients induced over the strong and weak axis of the element respectively.

Dwaikat et al. (2011) present the results of four steel columns that undergo thermal gradients throughout their depth. They used sprayed-on fire resistance material on three sides of column specimens to create the thru-depth thermal gradient, and analyzed how the plastic

المنارة للاستشارات

www.manaraa.com

axial-moment capacities began to subsequently warp. Garlock & Quiel (2008) computationally demonstrated the shape change in the axial load and moment diagram failure envelopes due to thermal gradients, as well as the moment reversal that takes place in steel members with an induced gradient. Their research showed that using the original failure envelope to analyze beam-columns under fire is conservative in some scenarios and unconservative in others, and therefore the warping of the envelope must be considered on a case-by-case basis. In this thesis, the gradient in the composite beam will be considered in all computational modeling, and the concepts of warped axial load and moment plastic envelopes will be utilized.

In prescriptive fire design, one has the choice of categorizing a structural assembly as "restrained or unrestrained" in order to decipher the necessary fire protection. The UL Fire Directory gives hundreds of examples of different types of systems that have been tested to pertain to a given fire rating (UL, 2016). However, many realistic and commonly used connections in practice do not fall into the category of completely fixed or pinned, but somewhere in between. Gewain et al. (2003) studied many different examples of fire exposed buildings and emphasized the lack of research and standardized test results available for structural connections. Gewain and Troup (2001) explain the confusion between the restrained and unrestrained assembles, and how they relate to real building systems. They point out how the laboratory set-up of end conditions performed according to the ASTM E119 does not accurately model the boundary conditions of typical floor construction. They also note that testing one beam in a standardized furnace according to the ASTM E119 specifications does not represent or replicate a full structural system scenario, and this can have significant implications in behavior during a fire.

المنارة للاستشارات
www.manaraa.com

In the early 2000's, researchers at the University of Canterbury began to study how steel connections behave in extreme heat. Seputro (2001) used SAFIR to analyze steel members with three and four sided heating and various end conditions. That study examined the unrestrained pin-roller connection, the fully restrained fixed-fixed condition, and two intermediate conditions of pin-pin and fixed-slide. All of these connections were analyzed in different types of fire conditions (linear ramp up fire, ISO 834 standard fire, and a parametric fire) to see how the connection types differ in varying intensity of fire. Wastney (2002) modeled beams within a frame system that had more realistic connections types by varying the end column stiffness. That study considered an unprotected steel beam with and without composite action subjected to a standard fire curve, using the same four end conditions as Seputro. Wastney correlated the different end conditions with different column stiffness's, and found relationships between the stiffness and restraint. Moss et al. (2004) used the same study done previously by Septuro and Wastney to show how the end conditions can cause large changes in how the beam behaves, and when and where the plastic hinges form. This thesis will further enhance the idea of modeling a full structural system by making the concrete slab continuous over beams and providing axial stiffness similar to what would exist in a real building. A shear tab connection is used and shown to exhibit behavior between a rotationally restrained and unrestrained condition. Additional models are shown with true pinned and true fixed connections to bound the solution of the tested beam with a shear tab connection.

This paper will enhance the previous work done in order to advance performance-based design as an alternative to the current standard prescriptive techniques. Beam failure times are compared using various design techniques, and examples are provided to determine the failure

المنارة للاستشارات

www.manaraa.com

time and system longevity when using performance based criteria. SAFIR models of varying complexity are discussed and validated against experimental results. Recommendations are made regarding the use of these computational models to conservatively predict and better understand the behavior of composite floors under fire.

www.manaraa.com

3.0 Experimental Facility

All of the structural furnace tests were performed in Lehigh University's ATLSS Engineering Research Center. The ATLSS Furnace is modular - its sides are panelized and can be reconfigured via bolted flange connections to create a furnace hearth that is sized appropriately for a given test (Catella, 2008). For this test, it was set up to be 4.57 meters long, 1.83 meters wide, and 2.13 meters tall (15'x6'x7'), as shown in Figure 1. It is noted that, in the photograph, one face of the furnace has been removed to show one of the composite floor specimens that was tested during this project.

Figure 1 – Modular furnace test fixture at ATLSS.

As shown in Figure 1 the steel test frame supports a concrete slab on corrugated metal deck, which forms the "lid" of the furnace. The specimen consisted of a steel beam with a concrete slab on top, and was connected to columns at both ends. The columns spanned through the height of the furnace and were pinned via clevis connections at the top and bottom to a heavy self-reacting frame. The furnace is well suited for evaluating the performance of

www.manaraa.com

floor subassemblies (with slab included) under fire. Additional schematic drawings of the furnace and test fixture are shown in Figure 2 and Figure 3.

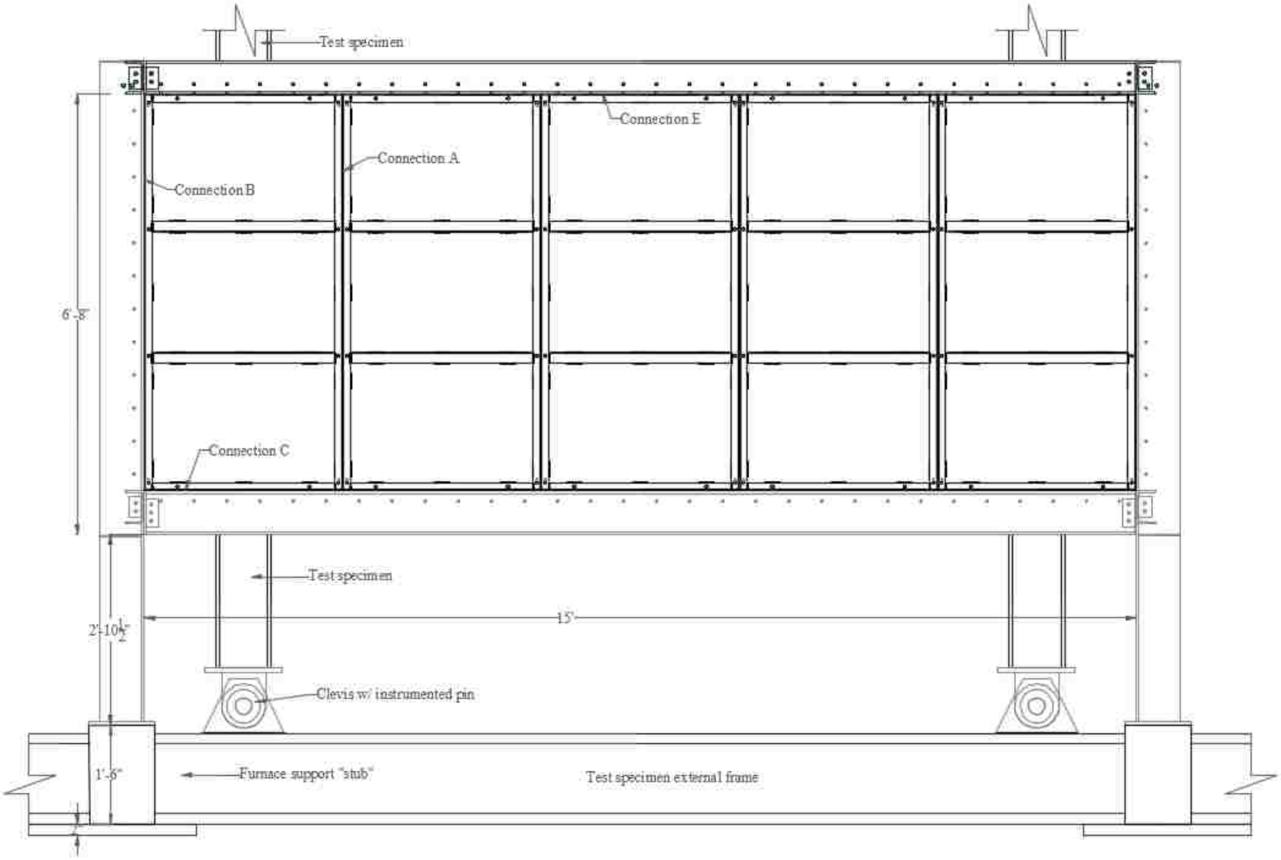

www.manaraa.com

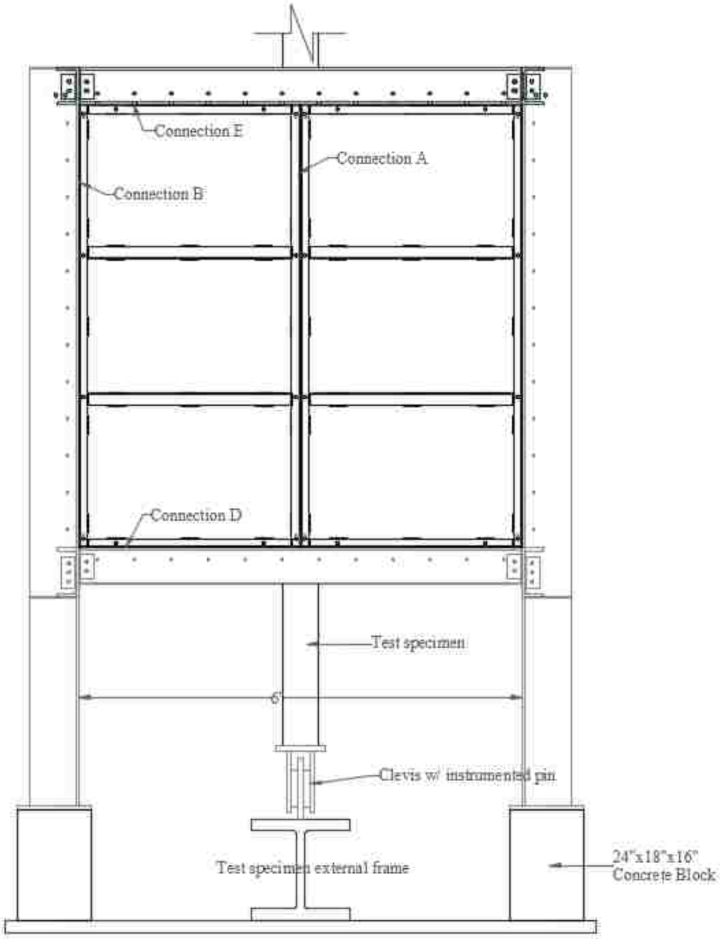

Figure 2 – Elevations of the modular test furnace at the ATLSS Center – Front and Side View.

المنارة للاستشارات
www.manaraa.com

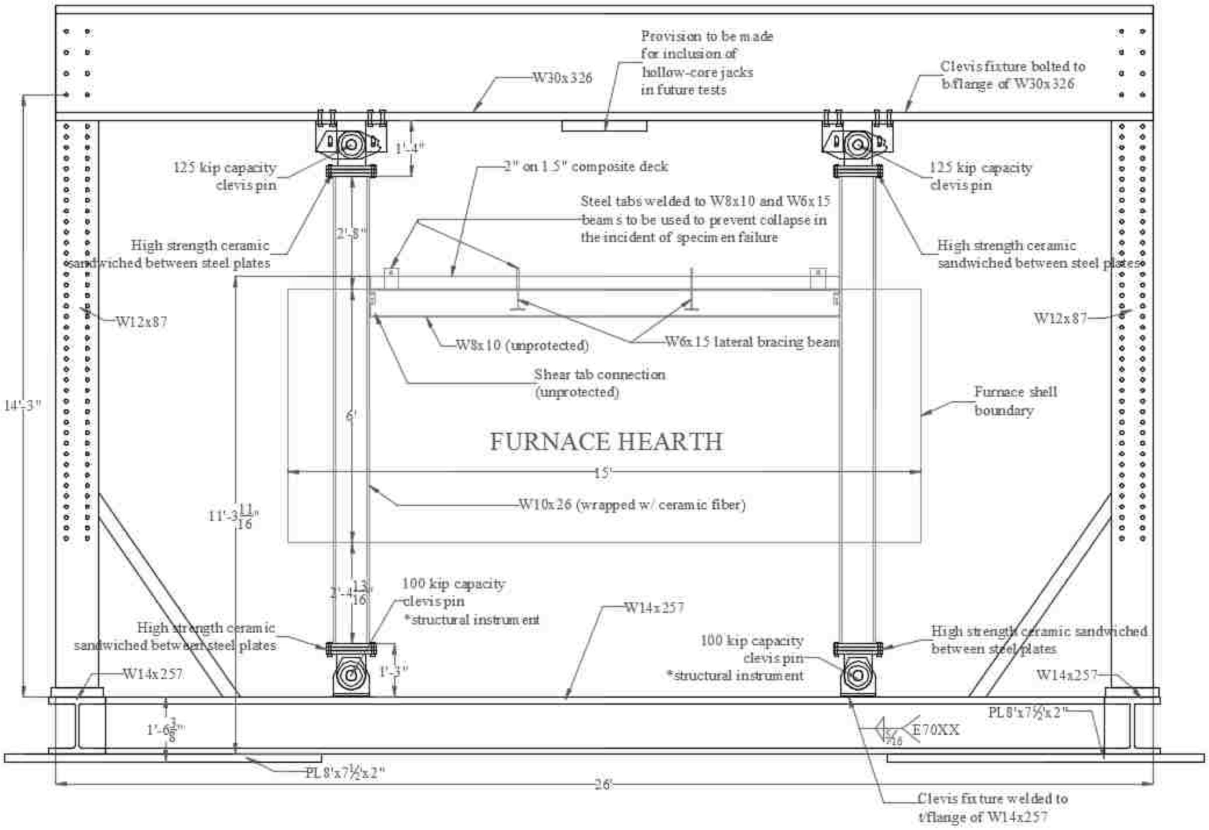

Figure 3 – Elevation of the self-reacting test frame for the modular furnace.

The furnace shell is constructed of 9.525 mm (3/8") thick steel plates (typical of high temperature industrial furnaces), with the exterior surface (cold face) stiffened by steel channels and angles. The modularity of this test system is derived from the modularity of the furnace shell, which is comprised of smaller panels that are reconfigurable to form different hearth configurations. The shell is held in place by a structural steel support frame. The interior surfaces of the furnace walls are lined with ceramic fiber refractory (commercially available in modules that are 6" thick), which are treated with a hardening solution to prolong service life (Catella, 2008).

The modular furnace test fixture uses two medium velocity pre-mixed Maxon Kinemax 3" Series G burners. Each burner has a capacity of 2.5 GJ/hr when fired on-ratio, where on-ratio

www.manaraa.com

refers to having the proper volume ratio of methane gas to air for perfect combustion to take place, so that combustion produces only CO_2 and H_2O with no leftover reactants. In general, on-ratio firing is approximately 10:1 air to gas. The burners have a turndown ratio of 96:1, meaning that each burner has a minimum capacity of 26 MJ/hr. This turndown ratio is important for experiments that require less power (Catella, 2008). Figure 4 shows one of the burners when firing.

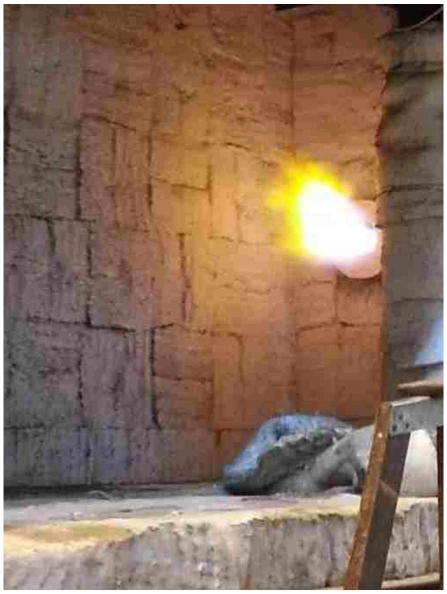

Figure 4 – Maxon Kinemax 3” Series G Burner while Ignited.

Air is supplied to the burners by a 5 HP blower. Natural gas is continuously supplied to the burner control system by the ATLSS Center’s main utility in the laboratory. A temperature controller is used to monitor and control the temperature within the furnace. The temperature controller is programmable to provide a user-specified time-temperature history.

www.manaraa.com

4.0 Test 1

The first test performed in the ATLSS furnace for this project evaluated the capabilities of the test equipment and the performance of a composite floor beam specimen. Prior to this project, the furnace had not been used in nine years, and modifications were made in order to reduce vibrations in the furnace wall and provide an adequate fuel line to the burners (Catella, 2008). The specimen, as described next, had been sitting in the furnace since its previous use nine years ago and was inherited for use in this project. This specimen had been previously tested in 2007, but there was no visual damage to the beam or concrete slab. The specimen was not designed by any current staff or students in ATLSS, and therefore the safety measures in place and the design of the specimen were partially unknown. The specimen had been heated three times in the past. The first time was by Catella, during a low temperature test where the furnace was ramped up to 400°F in 5 minutes, held for an additional 5 minutes, and then allowed to cool naturally after the burners where shut off. The second time was also performed by Catella, when the beam was tested for 32.5 minutes and reached a maximum temperature of about 1250°F**.** The third time was by the current research group when the furnace was ignited for about the first 5 minutes of the E119 standard curve in order to make sure the furnace was able to ramp heat sufficiently and no issues would come about during the specimen test. After these three instances, the beam had a residual deflection of about 1/2" at the beam center line, but was otherwise undamaged. The decision was made to not push the beam until structural failure, but instead to investigate whether the beam could withstand a realistic compartment fire curve. A description of the specimen, the test, and the results follow.

المنارة للاستشارات
www.manaraa.com

4.1 Test Setup and Specimen

4.1.1 Steel Composite Floor Beam Prototype

The inherited specimen consisted of a 3.35 meter (11'-1") long W8x10 beam with a 50.8 mm (2") concrete slab on top of a 38.1 mm (1.5") metal deck. The W8x10 beam was reduced by a half scale factor from the original prototype specimen, with each dimension reduced by the factor according to power of the dimension. For example, the area of the beam was reduced by a factor of 2^2, or 4, and the moment of inertia was reduced by a factor of 2^4, or 16. The system was designed with twelve 12.7 mm (½") diameter, 50.8 mm (2") long studs to create composite action. The slab had W2.1 x W2.1, 6"x6" welded wire fabric as reinforcement, due to the availability at the time it was made. Three concrete cylinders were made during the slab pour and tested to determine the crushing strength. The average crushing strength was determined to be 47.8 MPa (6.94 ksi). The beam was connected to W10x26 columns at either end with a shear tab connection as shown in Figure 5. The shear strength of the bolts was determined with three tests and averaged to be 446.4 MPa (64.75 ksi) (Catella, 2008).

The connections and columns were wrapped with a 6" thick ceramic fiber blanket throughout the test to keep them cold, and the beam was left completely unprotected (bare steel) as shown in Figure 6. The columns were wrapped to simulate the primary gravity members with passive fire protection. The removal of protection on these primary members is not recommended, and not the focus of this paper. The connections were wrapped in order to avoid a connection critical system. In many systems, even if the filler beams are left unprotected, the connections would receive some protection due to the spray overshoot from the primary gravity members. Since the application of the SFRM is done from a large hose, the

المنارة للاستشارات
www.manaraa.com

overshoot of the SFRM will provide some protection to the connections. The initial deflection of the specimen was about 50.8 mm (½") at the center due to previous tests.

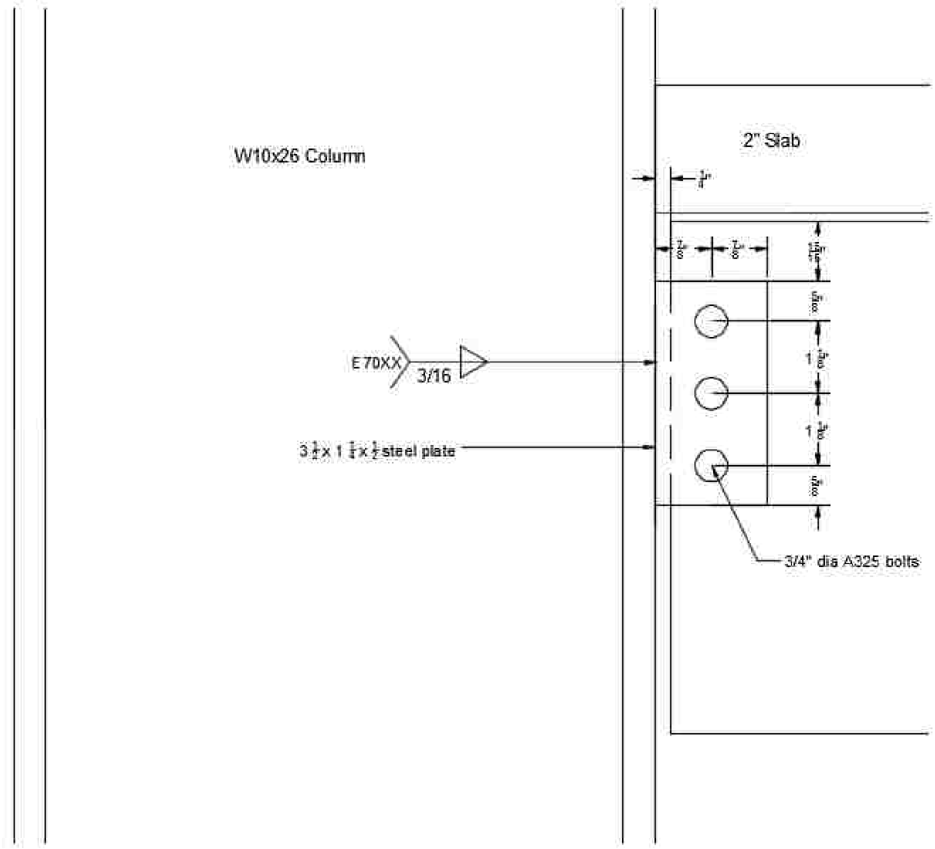

Figure 5 – Diagram of Shear Tab Connection

Figure 6 – Protective Ceramic Blankets on Columns and Beam Connections

المنارة للاستشارات
www.manaraa.com

The specimen was loaded with 20,017 N (4.5 kips) in two locations to create a moment similar to what would be seen in an office building. The induced load pushed the beam to 25% of the flexural capacity. The justification for this load percentage can be seen in section 5.12. The loading setup is shown in Figure 7.

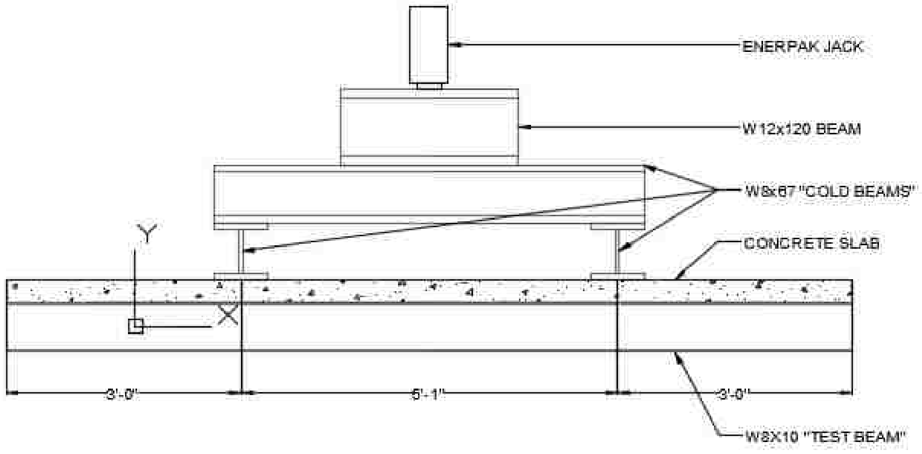

Figure 7 – Specimen loading diagram

A realistic fire curve (see section 4.1.2) was programmed into the control panel for the burner system. This curve simulated a 20 minute ramping fire, and then a decay phase. After the furnace was shut off, the beam was allowed to cool and relax into a stable state.

There were 53 thermocouples used during the test to measure the temperature of the specimen, connection, ambient air in the furnace, columns, and other locations on the outside of the furnace. The locations of the thermocouples are as follows:

- 3 on web (north, mid, south)
- 6 on bottom flange (2 north, 2 mid, 2 south)
- 6 on top flange (2 north, 2 mid, 2 south)
- 3 on concrete deck (north, mid, south)

المنارة للاستشارات
www.manaraa.com

- 9 ambient hanging throughout furnace
- 14 on connection (1 on each bolt, 2 on each weld, 2 on each shear tab)
- 4 on columns (2 on each column)
- 1 on overhead frame
- 1 on sidewall of furnace
- 4 on clevis connections (1 on each)
- 2 on LVDT's (1 on each)

There were two LVDT's and four string pots to measure the transverse deflection at the midpoint of the beam and the lateral deflection of the columns at the beam column connection. A heat gun was used to measure temperatures at designated locations on the outside of the furnace shell to make sure no part of the furnace was losing heat to the ambient environment in the lab.

4.1.2 Fire Scenario Development for Experimentation

A fire curve was chosen to heat the specimen based on the E119 standard fire test and various parametric models with and without active fire protection. Figure 8 shows the fire curve used to heat the specimen, labeled "Furnace Temp", along with five other fire curves that are similar in various ways. This fire curve created for the test was based on the assumption that active fire protection will ignite. The active protection plays a role to keep the maximum temperatures of the fire lower, and allows the fire to rapidly decay. This happens around 20 minutes for all of the curves shown in Figure 8. Figure 9 shows the average temperature data from the thermocouples located at the beam center on the web, top flange, and bottom flange, and the bolts in the connection zones.

www.manaraa.com

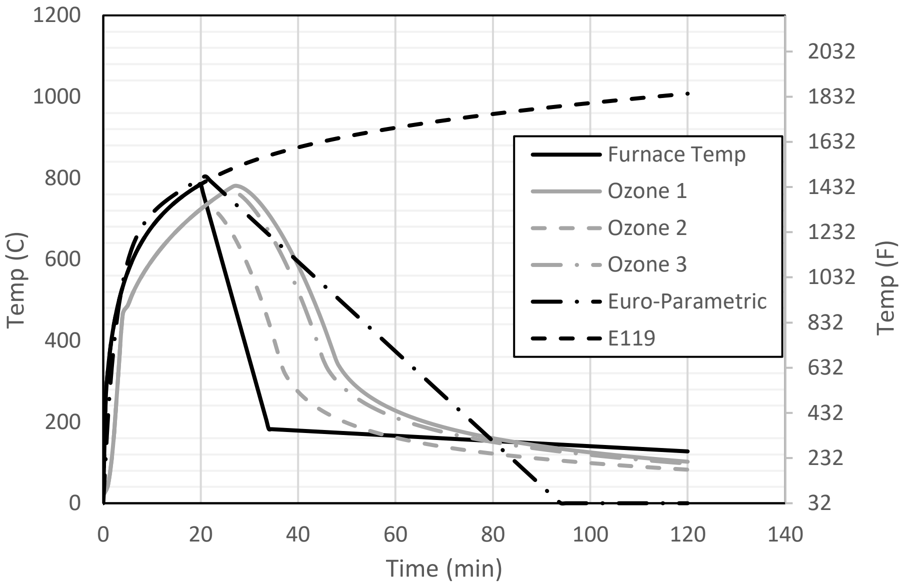

Figure 8 – Fire Curve Comparison

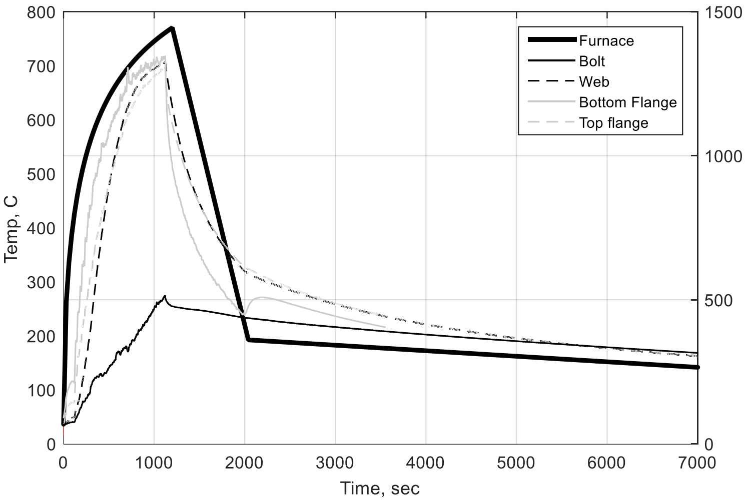

Figure 9 – Specimen Temperature from Test

Figure 8 shows that the E119 curve matches the furnace temperature for the first 20 minutes, but does not have a decay phase. The Eurocode parametric fire curve matches the ramp up portion of the furnace temperature closely, but decays at a slower rate (CEN, 2001). To construct this curve, Buchanan (2002) was referenced for compartment examples and decay

www.manaraa.com

rates that do not include active fire protection. This curve was based on a lightweight concrete compartment with the parameters given in Table 1.

Three OZone fire curves (Cadorin et al., 2001) were developed with varying fuel loads and active fire protection as listed in Table 2. These curves don't ramp up as quickly as the furnace curve, but the decay rates follow closer than the Eurocode parametric fire curve. The fuel loads chosen are consistent with the study performed in Khorasani et al. (2014) to indicate a typical range for office buildings. In most fires, active fire protection is triggered and can help shorten the fire duration, and this is demonstrated in the Ozone fire curves through the fire decay phase. The chosen fire curve took into account active fire protection, allowing a decay phase, but ramped up at the same rate as the standardized temperature curves.

Table 1 – Euro-Parametric Fire Properties

Compartment Materials		
Density	1600	kg/m^3
Specific Heat	840	J/kg K
Thermal Conductivity	0.8	W/mK
Fuel Load	500	MJ/m^2
Compartment Dimensions		
Room Length	5	m
Room Width	5	m
Room Height	3	m
Window Width	2.4	m
Window Height	1.5	m

www.manaraa.com

Table 2 – Ozone Fire Properties

	1	**2**	**3**	
Compartment Materials				
Density	1600	1600	1600	kg/m^3
Specific Heat	840	840	840	J/kg K
Thermal Conductivity	0.8	0.8	0.8	W/mK
Fuel Load	800	800	1200	MJ/m^2
Compartment Dimensions				
Room Length	5	5	5	m
Room Width	5	5	5	m
Room Height	3	3	3	m
Window Width	4	4	4	m
Window Height	0.6	0.6	0.6	m
Active Protection				
Automatic Water Extinguishing	x	x	x	
Independent Water Supplies	x	x	x	
Fire Detection by Smoke		x	x	
Work Fire Brigade	x	x	x	
Off Site Fire Brigade				
Safe Access Routes	x	x	x	
Alarm Transmission to Brigade		x	x	
Fire Fighting Devices	x	x	x	
Smoke Exhaust System	x	x	x	

4.1.3 Observations from Test

The beam was able to last through the full 20 minute fire ramp and decay. The slab had a spreading crack that formed in the concrete above the beam centerline. Hot gases were able to escape through the crack towards the end of the test, and stability of the specimen became a concern. However, no instabilities in the specimen were deemed unsafe, and the beam was able to push through the full 20 minute fire ramping, and stabilize during the decay. Figure 10 through Figure 13 show various photos of the specimen after the test. The longitudinal splitting crack down the middle of the slab can be seen in Figure 10 and Figure 11. Figure 12 shows the

www.manaraa.com

deflection of the beam after the test and removal of the ceramic fiber blankets. Figure 13 shows the shear tab connection after the test. Very little warping occurred in the bolted connection.

Figure 10 – Photo of top of slab after Test 1

Figure 11 – Close up of longitudinal crack

www.manaraa.com

Figure 12 – W8x10 after the test

Figure 13 – Shear tab connection after the test

المنارة للاستشارات

www.manaraa.com

4.2 Computational Modeling

4.2.1 2D and 3D Beam Models

SAIFR 2016 was used to create 2D and 3D models of the specimen using beam elements for the steel frame. The 2D models consisted of a thermal model that included the beam and slab as a consolidated cross-section, shown in Figure 14. 816 elements were used in the analysis, where 144 elements were used in the beam and 662 were used in the slab. In the thermal model, the top surface of the top flange is assumed to have full contact with the slab, which is represented with its minimum thickness dimension. In the 2D composite section, the steel mesh reinforcement is neglected. The 2D structural model used 2D beam elements to create a stick frame, as shown in Figure 15. The beam elements were discretized at one-foot lengths per recommendations from a previous study by Quiel and Garlock (2010b).

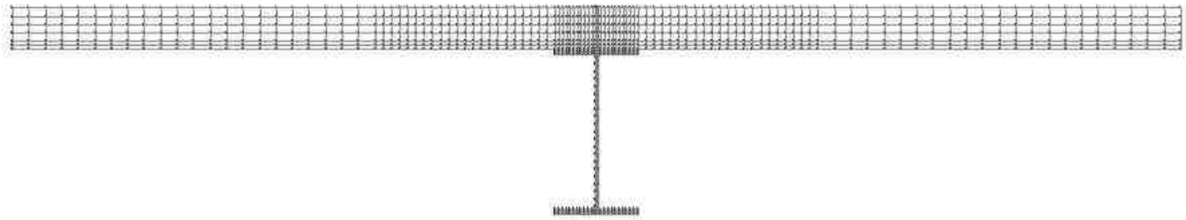

Figure 14 – Thermal mesh for 2D beam and slab

The 3D models consisted of separate thermal models for the beam and slab, and a structural model that used beam elements for the beam and column, and shell elements for the slab, as shown in Figure 16. The beam elements kept the same discretization as the 2D models for the flanges and web, and the shell elements were discretized to one-foot squares and modeled with 5 integration points through their thickness. The shell elements were modeled with 9 temperature locations through their depth, obtained from the slab thickness

www.manaraa.com

simulation in the 2D composite beam cross-section. The slab edges were modeled with no restraints to simulate the test conditions. In both models, the columns were simulated as “cold”. The steel members and concrete slab (which in the shell elements included the steel mesh reinforcement) were modeled with thermal and structural material properties according to Eurocode 3 and Eurocode 2, respectively.

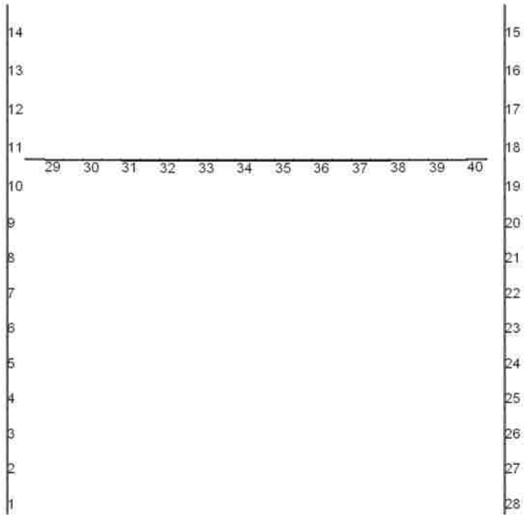

Figure 15 – 2D frame from SAFIR

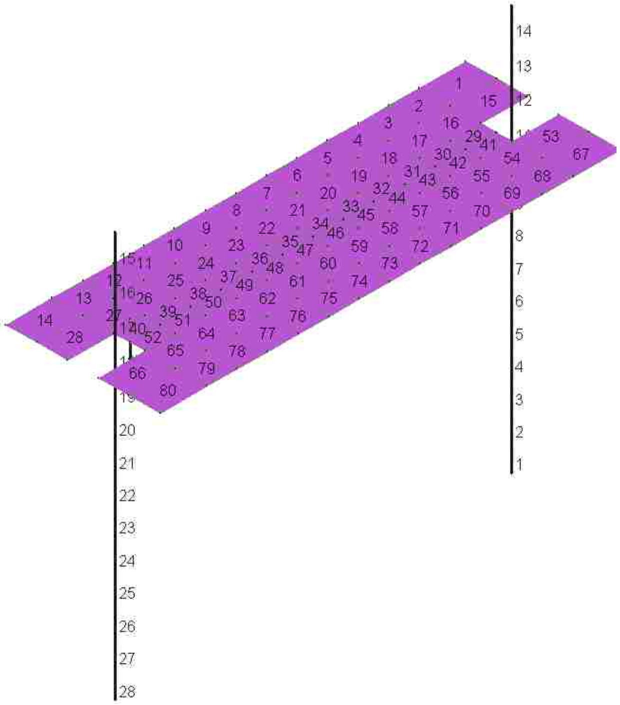

Figure 16 – 3D frame from SAFIR

In both models, the columns are pinned at the top and bottom in the plane of the frame to simulate the clevis boundaries. The beam to column connection was modeled as both pinned and fixed to envelope the behavior of the shear tab. In the 2D models, the slab was raised 38.1 mm (1.5”) to incorporate the corrugation depth of the metal decking, as shown in Figure 17. The thermal mesh and the structural mesh were the same, outside of the position of the slab. In the thermal analysis, the slab is in contact with the top flange of the beam, and in the

المنارة للاستشارات
www.manaraa.com

structural analysis the slab is raised as shown in Figure 17. In the 3D models, the beam was restrained against torsion to simulate the lateral bracing of the composite slab. The rebar mesh in the slab was modeled as a thin, smeared steel layer corresponding to the equivalent area per width within the concrete slab shells. These shells were modeled with a constant thickness corresponding to the minimum 50.8-mm thickness of the corrugated slab. Small, very stiff connector elements were inserted between the beam and slab at 1-foot spacing to simulate shear studs and create composite action. These connectors were kept cold and given a modulus of elasticity of 500E9 N/m^2 to ensure they would behave similar to a rigid shear stud, and not deform with load. Since the beam heats at a quicker rate than the slab, the percent composite increases to 100% fairly quickly (Wang et al, 2016). It is therefore not critical to allow shear deformation between the slab and beam, justifying the use of the "nearly rigid" stud connector.

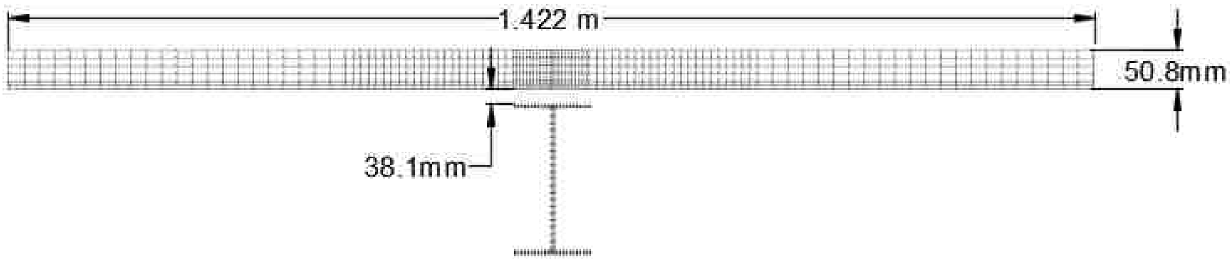

Figure 17 – Structural Mesh from SAFIR

The realistic test fire curve (shown in Figure 8) was used as the input for all thermal models. The beam was heated on three sides (i.e, it is assumed that the top flange was fully shielded from fire exposure), and the slab (modeled at minimum thickness) was fully exposed on its bottom surface. The top of the slab was modeled at ambient and was able to realistically release heat to the compartment above.

المنارة للاستشارات
www.manaraa.com

4.2.2 Thermal Comparison

Quiel and Garlock (2010) created simple equations to predict the lumped mass temperature of a steel beam heated on three sides (similar to a perimeter column or floor beam) based on the theory of convection, conduction, and radiation. Matlab was used to apply these equations and calculate the temperature of the beam in three lumped mass sections: the two flanges and the web. The bottom flange and web are assumed to be fully exposed to fire. The top flange was modeled with all surfaces exposed except the top surface, which was modeled as 70% exposed to convective heat transfer from the fire to account for realistic contact and partial shielding from the bottom of the corrugated deck. Figure 18 shows the predicted temperatures of the flanges and web based on the lumped mass calculation. Figure 19 shows how the top flange temperature from the lumped mass calculation compares with the test data and the SAFIR predicted top flange temperatures. The lumped mass predictions match the “ramp up” phase of the fire closely but show less agreement with the decay phase. Conversely, the predicted SAFIR top flange temperatures more closely match the decay phase, but under-predict the fire growth. Figure 20 shows the temperature comparison between the Matlab lumped mass approach, the SAFIR thermal analysis, and the measured test data for the web, bottom flange, and top flange. Both the SAFIR temperatures and test data are represented as average values.

www.manaraa.com

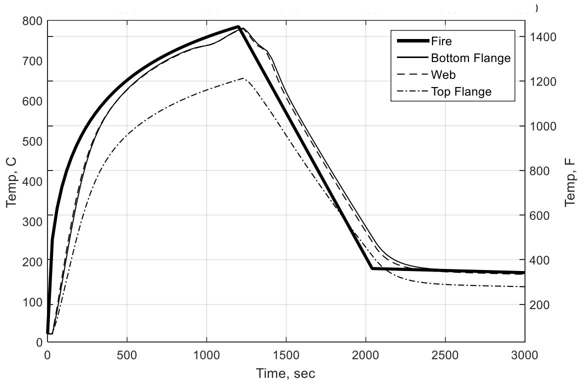

Figure 18 – Lumped Mass Temperatures

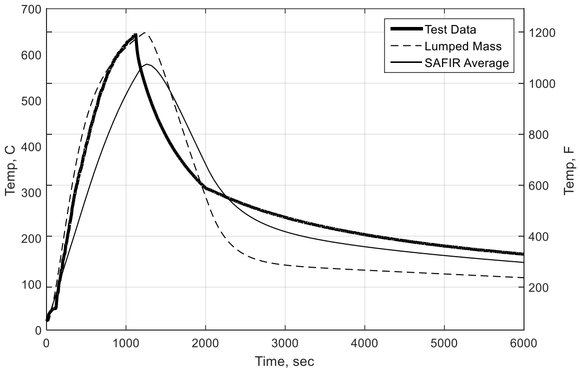

Figure 19 – Top Flange Temperature Comparison

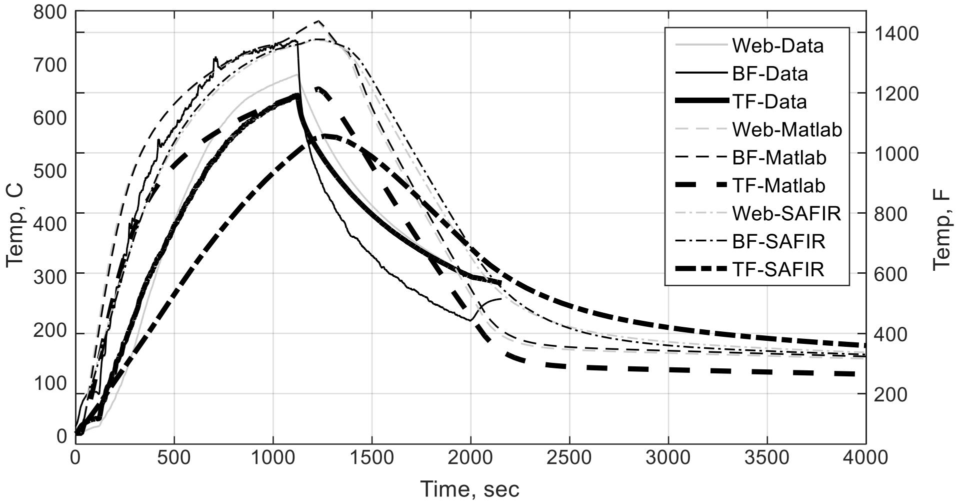

Figure 20 – Beam Temperature Comparison

According to the E119 temperature criteria, a beam fails when the average temperature exceeds 593.3 °C (1100 °F) or the maximum temperature exceeds 704.4 °C (1300 °F). The temperatures from the thermocouples located on the beam were used to experimentally determine when these limits were exceeded. The beam exceeded the maximum limit at 11:40 and the average limit at 11:38. The thermal criteria do not take into account whether the beam is restrained or unrestrained nor any of the structural behaviors in the system, and are generally considered to be conservative. Research has shown that almost all beams in a

www.manaraa.com

building should be considered restrained (Ioannides & Mehta, 1997). The test structurally demonstrated that the unprotected beam was able to withstand a ~20-minute fire without large amounts of permanent damage. If this beam had been protected, it would have cost more time and money during the construction, and may not have provided a different outcome at the end of the fire.

4.2.3 Structural Comparison

The models were verified with the data collected in the test. The lateral deflection of the column at the beam-to-column connection and the transverse deflection at the midpoint of the beam were compared with the SAFIR structural models, as shown in Figure 21 and Figure 22. These models use the temperature predictions from the SAFIR thermal analysis.

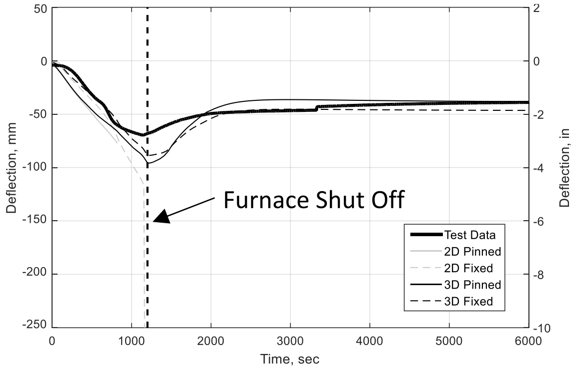

Figure 21 – Beam Deflection Comparison

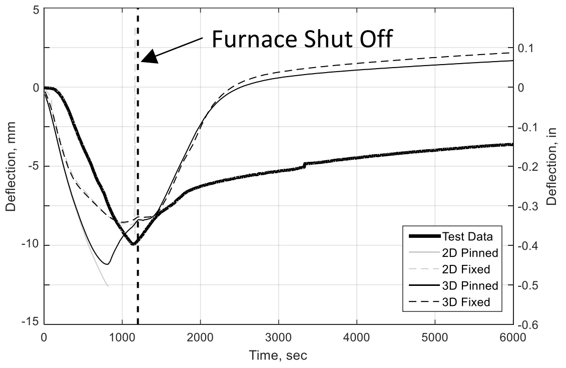

Figure 22 – Column Deflection Comparison

It can be seen that the 3D fixed and pinned models bound the behavior of the test beam in most sections. Typically, engineers will model a shear tab connection as a pin; however, the models show that the tab behaves closer to that of a fixed connection in this case. Reasons for this could include that the connection provides more rotational restraint than expected or that since the connection was kept relatively cool (see the bolt temperatures in Figure 9), it did not

www.manaraa.com

significantly decrease in stiffness throughout the test. It should also be noted that the 2D models didn't match the behavior well, and both the fixed and pinned cases predict failure before the furnace was shut off. This is an important conclusion because it shows that the 2D models are not effectively capturing the structural performance of the composite system. These results indicate that structurally modeling the slab as separate from the floor beam can significantly impact the predicted fire-exposed performance.

Figure 23 shows four snapshots of the axial-moment (P-M) diagram for the 3D fixed beam output at the beam-column connection. The positive P value corresponds to compression and the positive M value represents hogging moment. The first snapshot occurs before the fire has begun, and shows that the beam is loaded to ~25% of composite moment capacity and no axial force at ambient temperature per the initial design. As the beam heats up, the P-M envelope begins to skew due to the shift of the neutral-axis (Garlock and Quiel, 2008). At ~8 minutes from the furnace ignition, the yield strength and plastic moment have decreased such that the normalized P and M in the beam reach the plastic P-M envelope. The beam remains plastic until ~21 minutes as its normalized P-M state remains on the plastic envelope as it changes shape through a moment sign reversal. At this time, the beam quickly loses applied axial force as the fire decays and the beam cools down. As the beam cools, it retracts back in, explaining the transition seen in the fourth snapshot from a large compressive force to a neutral axial force and negative moment.

www.manaraa.com

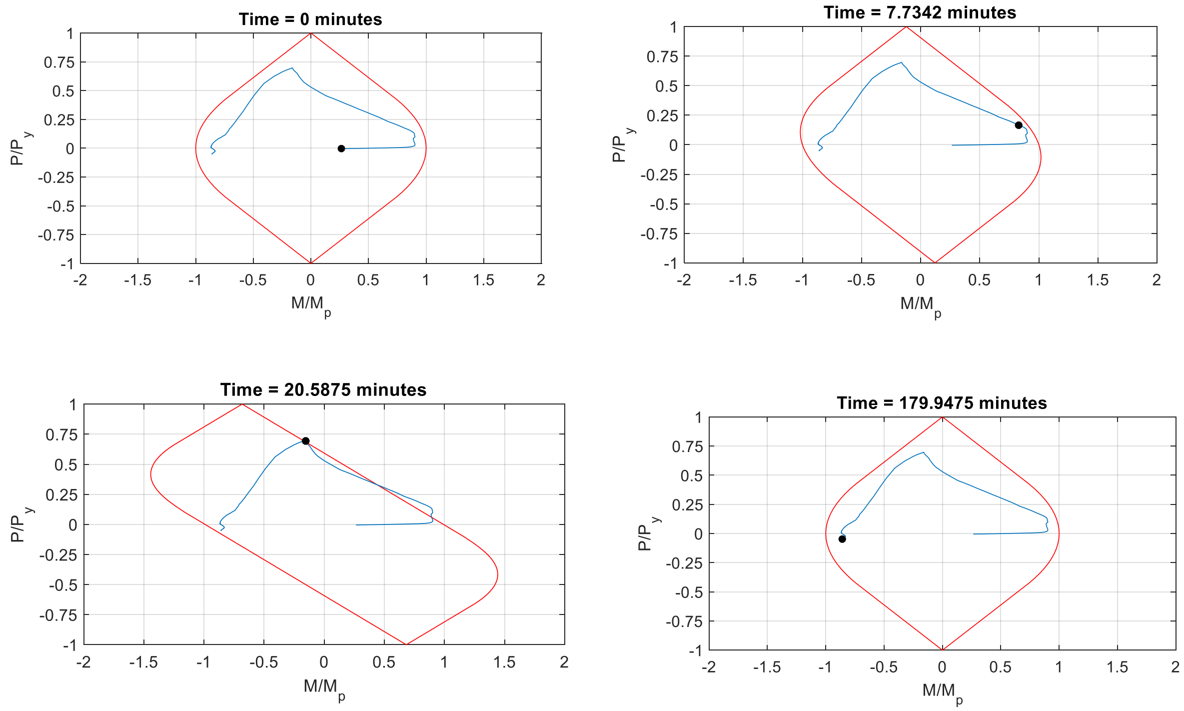

Figure 23 – P-M Diagrams for 3D Fixed Beam at Beam-Column Connection

This same pattern can be seen in Figure 24 with the P-M diagrams of the 3D pinned beam at the beam-column connection. The pinned beam starts at zero moment and axial force, since this connection cannot transfer any moment. The pinned beam takes longer to hit the plastic P-M envelope than the fixed beam, around 13.5 minutes after the start of heating, as shown in the second snapshot. Note that a small amount of moment is registered in the normalized moment values – the moment readings are obtained at Gaussian integration points along the beam length, meaning that the moment is not exactly zero but is instead a small amount measured at 0.11 feet from the connection. The normalized P-M state of the beam then rides along the plastic envelope as it shifts, as shown in the third snapshot. The fourth snapshot shows that the pinned beam stabilizes with a similar amount of axial force and moment as the beginning, and loaded and unloaded on the same path. It is important to note

www.manaraa.com

that the shift in the P-M diagrams is important since the beams would have reached the plastic envelope at a later time if this shift was not accounted for.

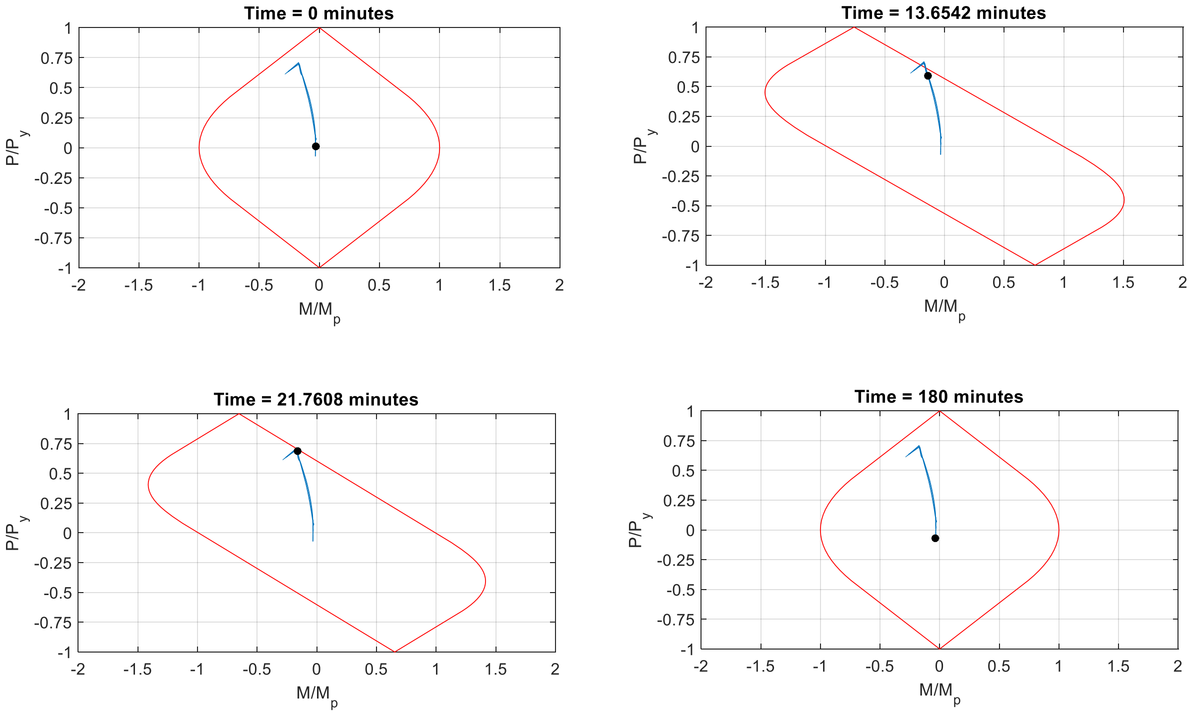

Figure 24 – P-M Diagrams for 3D Pinned Beam at Beam-Column Connection

The comparison of the axial force and moment in the fixed and pinned beams (measured near the connection) is shown in Figure 25 and Figure 26 respectively. As expected, the pinned is not able to hold significant moment at its ends. Both beams go quickly into compression, then swing back into tension around 50 minutes after the start of heating.

www.manaraa.com

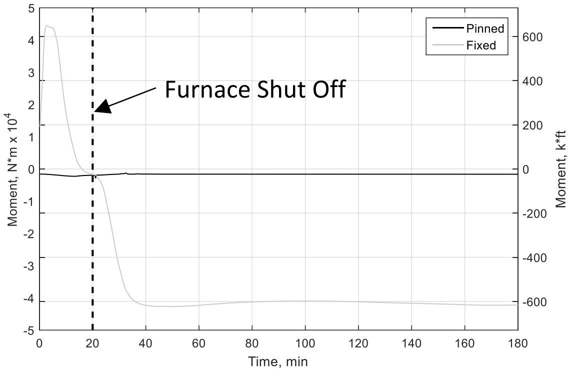

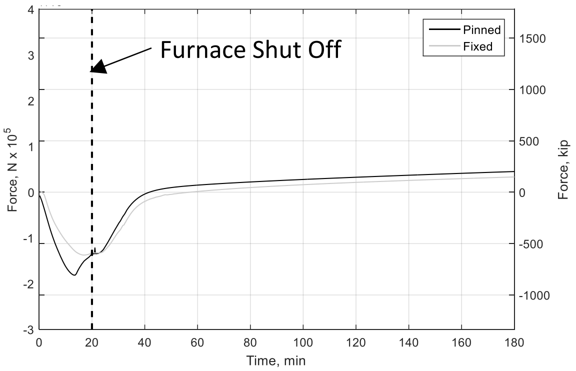

Figure 25 – Beam End Moment

Figure 26 – Beam End Axial Force

Next, the lumped mass temperatures, as previously discussed, were used as input into the SAFIR structural model to see if better correlation between the data and models could be obtained. This was done by removing the steel temperatures that SAFIR calculated, and inserting the three lumped mass temperatures at each time step. This was only done for the 3D models, since the 2D models were shown to provide less accurate predictions. Figure 27 shows the vertical deflection at the beam midspan for the pinned and fixed cases using the original SAFIR temperatures and the lumped mass temperatures along with the tested beam deflection. Similarly, Figure 28 shows the transverse deflection of the column. Both figures draw a coherent conclusion; the lumped mass temperatures increase initial deflection, but allow for greater post-heating deflection rebound. This conclusion matches the previously discussed data that showed the lumped mass predicting an accurate ramp up in temperature, but maintaining more heat during the decay phase. For the fixed case, the lumped mass model better predicts the beam deflection, but the SAFIR temperature model better predicts the column deflection. For the pinned case, the lumped mass temperature model shows less agreement with the experimental deflections than the SAFIR model. Since the lumped mass over predicts the

المنارة للاستشارات
www.manaraa.com

deflections, the pinned beam nearly experiences runaway failure before the furnace shuts off and cools. This causes the beam deflection prediction to be much higher, with a similar level of recovery. This phenomena is also seen in the pinned lumped mass deflections of the column. After the furnace is shut off, the beam starts to cool and causes the column to lurch outwards. It is important to note that the lumped mass predictions are more conservative than the SAFIR predictions. The lumped mass temperatures can be obtained easily through solving a simple set of equations, and the finite element modeling of the discretized cross-sections is more computationally expensive and requires more user knowledge.

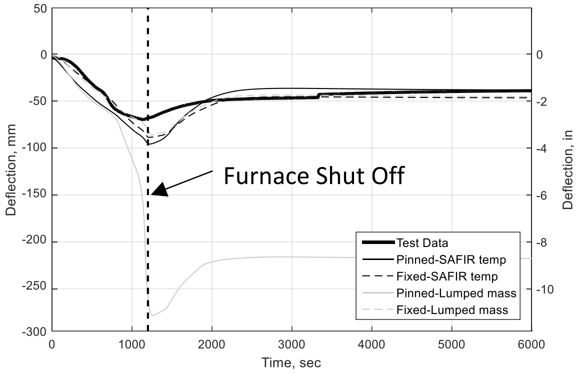

Figure 27 – Beam Deflection Comparison 2

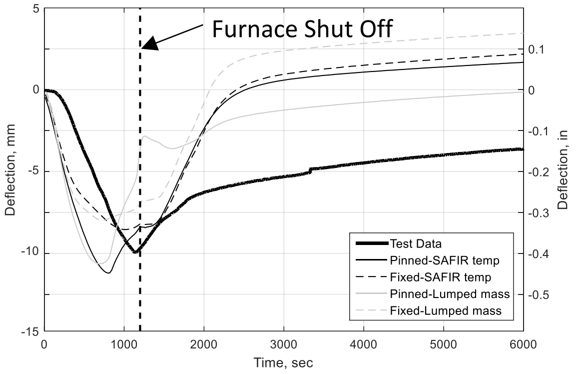

Figure 28 – Column Deflection Comparison 2

4.2.4 Partially Rigid Boundaries

Since the completely pinned and fixed boundary conditions on the beam have not been matching the true behavior from the test, but bounding it, a partially rigid boundary condition was made in SAFIR. A small connector beam element was used to connect the end of the beam to the column. The rotation that a simple pinned connection would provide was isolated in the model to allow only that degree of freedom to be manipulated in the connector element. Translational degrees of freedom were constrained from the end of the beam to the

www.manaraa.com

corresponding node of the column. The rotational connector element was kept cold and the young's modulus was varied to change the stiffness until the boundary connection provided a better correlation with the test data. The model was run with a young's modulus of 210E9 N/m^2 in order to verify that this acted similarly to the completely fixed model. When the young's modulus was changed to 1E9 N/m^2, the model provides slightly better predictions of the test data, as shown in Figure 29 and Figure 30. It should also be noted that although the partially rigid connection better predicted the maximum deflections for the column, it did not closely predict the final deflections after the furnace was shut off and the beam cooled. The maximum deflection for the beam is similar to the fully fixed and pinned models due to the small variation between these models. For both the beam and the column, the partially rigid connection model predicted worse values for the deflection recovery compared to the fully fixed and pinned models.

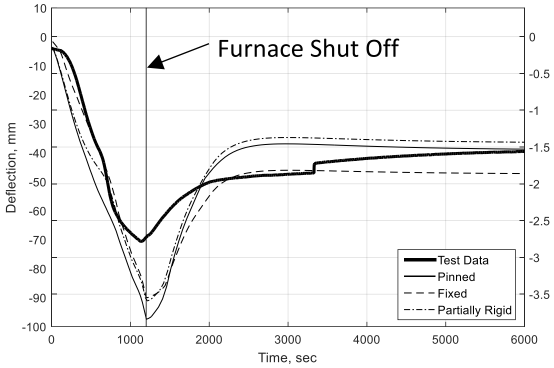

Figure 29 – Beam Deflection Comparison 3

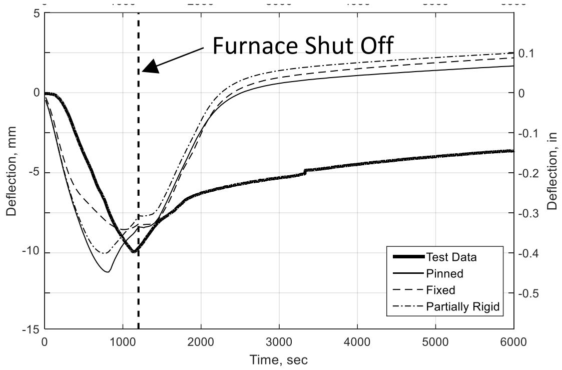

Figure 30 – Column Deflection Comparison 3

4.2.5 Shell Models

A shell model of the W8x10 beam was constructed in SAFIR to see if a higher level of sophistication in the models could provide closer predictions to the test data results. The beam

المنارة للاستشارات
www.manaraa.com

was created with a discretization of 1.5” x 1.5” shells. The slab was modeled using the same shell element approach as in the 3D beam models. The same nearly rigid connector was also used at 1-foot increments along the beam length to develop composite action between the beam and slab. The test beam was examined after the test and showed a very slight wave in the bottom flange near the end connections. The buckling was not able to be simulated in the beam models but can be captured in the shell model.

The beam temperatures were discretized so that temperature could vary along the beam length and cross section. The ends of the beam were kept cooler to simulate the test conditions of the connection zone wrapped in ceramic blanket. During the test, thermocouples were placed on each bolt of the shear tab connection. The average temperatures from these six bolt locations (three on each shear tab) were input into SAFIR as the temperatures for the beam ends. These temperatures were used in the first and last 50.8 mm (2”) of the beam for the full cross section, and the bolt time temperature curve can be seen in Figure 9. The next 355 mm (14”) on both ends of the beam were broken up into fourteen equal transition zones, where the temperature of the cross section was linearly increased from the colder ends to the hotter middle section. Each of these transition sections had different temperatures for the flanges and the web based on the range between the hottest and coldest sections. The peak temperatures for each of the zones in the beam web can be found in Figure 31. The same method was used to step the temperature for the upper and lower flanges. The middle “hot” section pulled from temperatures provided by the Matlab lumped mass calculation, providing different temperatures for the top flange, web, and bottom flange, shown previously in Figure 18. The full shell model can be seen in Figure 32, with the different colors showing where the

www.manaraa.com

transition zones are located on the beam, as well as the thickened shear tab where the elements were made to include the sum of the web and tab.

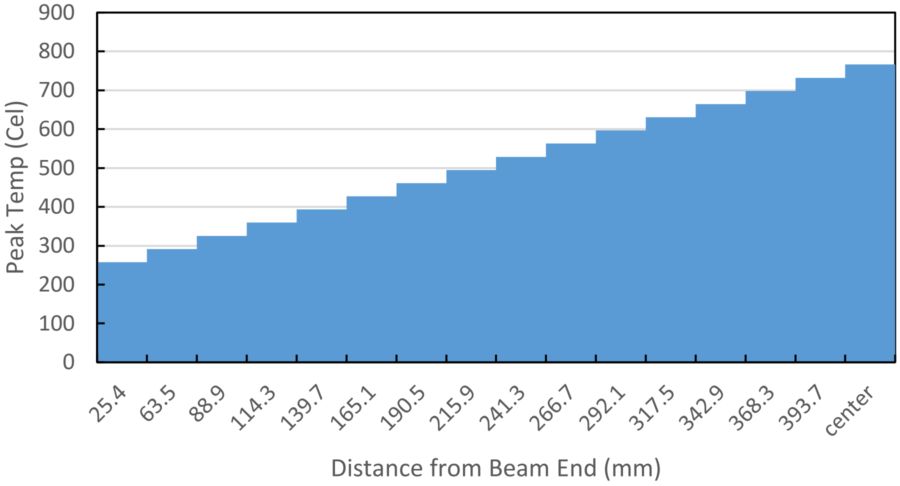

Figure 31 – Peak Temperatures for Each Beam Web Zone

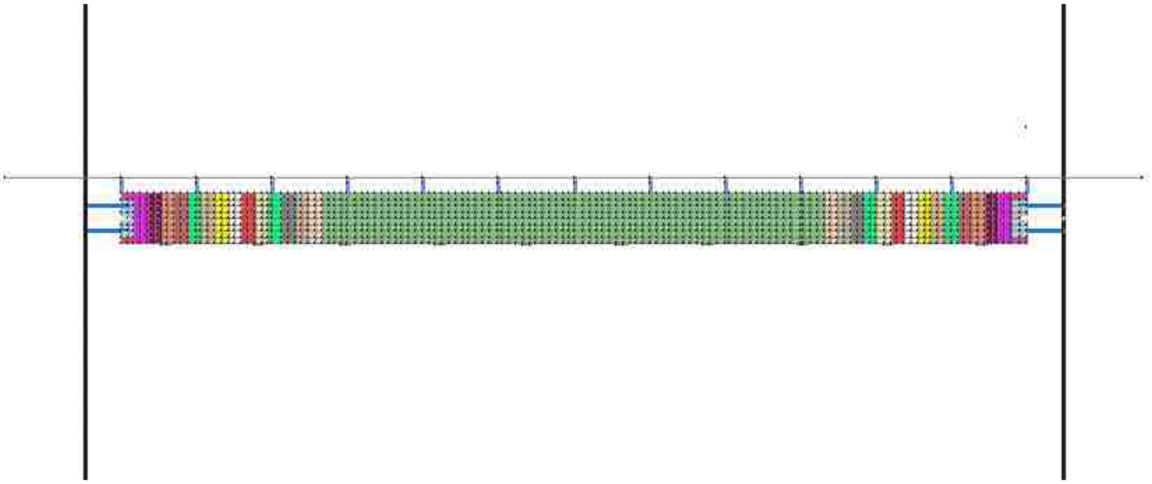

Figure 32 – Shell Model with Temperature Transitions

Truss elements (capably of axial force only) were used in the model to connect the beam and column and provide axial connection stiffness. Three truss elements were used at each connection to symbolize the bolts in the shear tab connection. These elements were given a lower stiffness than the beam so that the connection could behave similarly to a shear tab,

المنارة للاستشارات
www.manaraa.com

and not provide too much fixity. The shell elements that were located in the section that overlapped with the shear tab connection were thickened to account for the beam web (4.4mm thick) and the tab thickness (12.6mm thick). This added necessary stability to the connection to achieve numerical convergence at these locations of concentrated reaction force.

Imperfections were added into the beams web and bottom flange. The top flange was left perfectly straight because it is braced against the metal deck, and is therefore realistically unable to experience local buckling. The amplitude of the imperfections in the web were based on a value of T/500, where T is the height of the web plate, and was calculated to be 0.003 meters. The number of waves in the web were based on the web aspect ratio of a/b divided by 2, based on research previously presented by Quiel and Garlock (2010). For this beam, the aspect ratio is 20.5, therefore an even value of 10 wavelengths were added into the web. The imperfections in the bottom flange were based on the values from the web. Ten wavelengths were added into the bottom flange to create consistency in the model and an amplitude was calculated as 0.0018 meters to force the web and bottom flange to remain at a right angle.

The outcomes of the shell model are shown in Figure 33 and Figure 34 for the beam and column deflections. The shell models are compared to the test data and the 3D beam models. The shell model closely predicts the maximum deflection for the beam and the column. For the beam, the shell model accurately predicts the recovery. However, for the column, the test data shows that the column did not recover as quickly as the models predict. The slower recovery can be explained as follows. One cause could be that the column was not kept completely cold, as it is in the models. Because of this, the column could have lost stiffness throughout the test and was unable to fully recover as predicted by the models. As the column expanded from the

المنارة للاستشارات
www.manaraa.com

heat, second order effects could cause the axial force in the column to increase. It is possible that the column got “jammed up” because it had been sitting in the pinned condition for multiple years, and then lurched free at one point, as seen in the test data around 3300 seconds. The clevis pins at the boundary of the columns were old, which may have caused the lurching action. Another cause may be that the ridges in the concrete hold heat, and the ridges were not present in the thermal models. The ridges are present in the models as weight, but do not have the ability to store heat and change the thermal capacity of the slab. This extra heat sink causes the whole system to cool slower, and the columns to recover at a slower rate. Figure 34 shows that the test data is trending towards the convergence of the models, but the data acquisition was shut off before the system fully recovered. In future studies, a factor should be implemented into the concrete thermal model when the ribs are not present to adjust for the decreased ability to store heat. This would allow the models to better predict the cooling and recovery phase of the floor system.

It should also be noted that there was no complete gap closure between the beam edge and the column for the models or seen in the test. The gap between the members was not completely breached, and from inspection of the members after the test, the beam and the column were not scuffed or smashed.

المنارة للاستشارات
www.manaraa.com

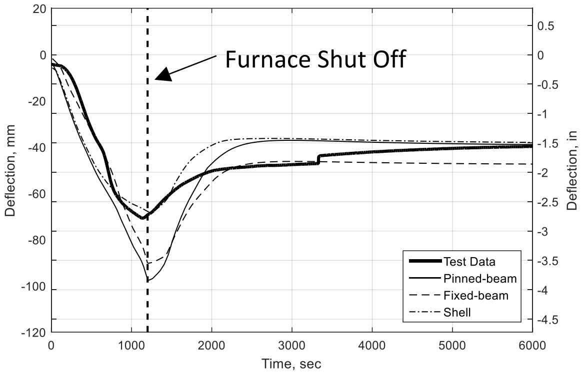

Figure 33 – Beam Deflection of Shell Model

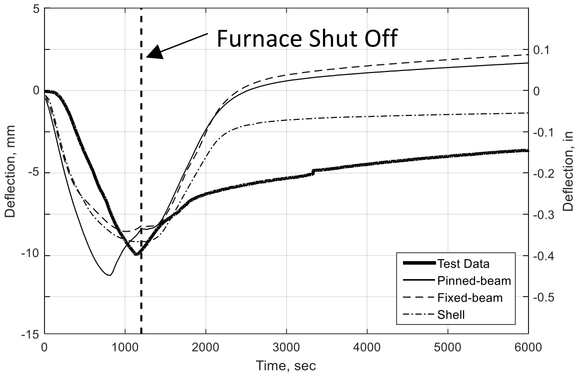

Figure 34 – Column Deflection of Shell Model

The shell model is much more detailed and advanced compared to the 2D or 3D beam models, and better predicts the composite floor system behavior from the test. However, the 3D beam pinned and fixed models are able to provide relatively close and conservative estimates to the test data, and can be simply made with much less time.

All of these models show that this assembly is able to survive the realistic fire curve, which accounts for compartmentation and ignition of active fire protection. The E119 thermal criteria predict failure at less than 12 minutes, but the experimental test and models show that the beam was able to resist a rapidly increasing fire curve for 20 minutes and a sharp decay phase, completely unprotected.

4.3 Simulation with Realistic End Constraint

The 3D beam-shell models were updated to create conditions similar to a building. This was done by removing the columns and inserting perfect boundary conditions at the beam ends. This is more realistic because the columns alone have much less stiffness than if surrounded by a building system. When the beam pushes into and pulls against the column, it provides much less restraint and stiffness than if the beam is reacting against a building

المنارة للاستشارات

www.manaraa.com

diaphragm. The slab wings that wrapped around the column were removed, and the slab edges were made continuous through the following changes:

- Short edges were fully clamped against translation.
- Long edges were restrained against rotation about the longitudinal (x) direction (see Figure 35 as reference).

One more row of slab shells were added onto the short ends of the slab to increase stability in the edge shear studs and represent the slab extension toward the centerline of the adjoining girder (to which the beam is perpendicularly connected). Figure 35 shows the layout of the model in SAFIR. The models were analyzed with the test fire curve as well as the full E119 curve to show the difference if active fire protection systems were damaged and did not ignite properly. Shown in Figure 36 are the beam deflections for the pinned and fixed models under various conditions. The “realistic” cases use the updated boundary conditions to create models that relate to a beam in a building instead of the test frame.

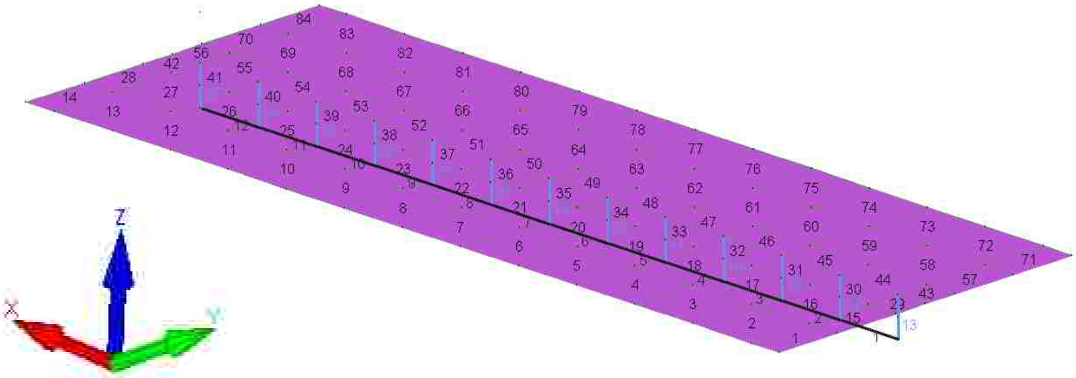

Figure 35 – 3D Beam SAFIR Model Made Realistic

المنارة للاستشارات
www.manaraa.com

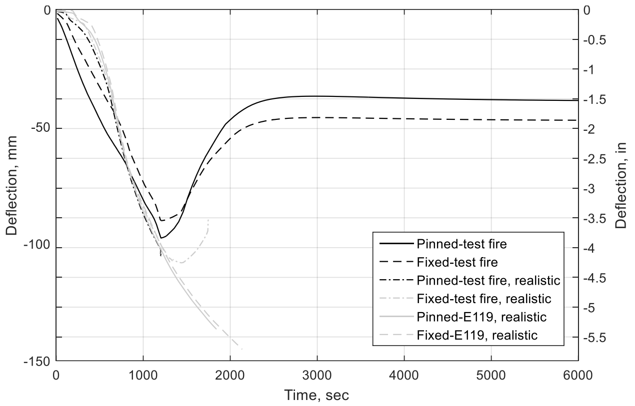

Figure 36 – Beam Deflection Comparison of Realistic Beam Models

The first thing to note from Figure 36 is that the pinned and fixed boundary conditions do not have very much distinction when the models were updated to represent a realistic building setup. For models using the realistic boundary conditions with either fire, the fixed beam model is able to slightly outlast the pinned case. The diaphragm used in this building is assumed to be very stiff, therefore the rotational rigidity in the slab edges at the end of the beam span prohibits significant rotation in the pinned connection. The presence of the slab creates a coupling action between the steel beam and rebar, emphasizing the importance of accounting for the slab in the analysis of the system. In addition, the model only depicts one floor bay being heated, when in some fire scenarios two neighboring floor bays can be simultaneously heated. In a two floor bay fire, the tension that develops in the rebar would double due do the pull from the slab membrane action occurring simultaneously in neighboring bays.

Another note from Figure 36 is that the pinned and fixed beams under the full E119 curve crash around 31 minutes and 36 minutes after the start of the fire, respectively. Many people assume that a fixed beam will outlast a pinned beam in this scenario, but in reality the

www.manaraa.com

failure time and behavior is very similar for each connection type. Both beams are able to last past a half hour, allowing significant time for the fire to be reduced or removed before the beam would completely collapse. Although it is likely that the beam would have to be replaced if left completely unprotected, the absence of collapse would improve the likelihood of the surrounding structural stability to be maintained and allow occupants a better chance of safely exiting the building.

The same method is applied to the shell model to create a realistic model of how the beam would perform in a building. Figure 37 shows the layout of the model in SAFIR. A similar technique of transitioning the beam from hot to cold using 15 zones is shown with different colors. Figure 38 shows how this model compares with the realistic beam models and the test fire shell model.

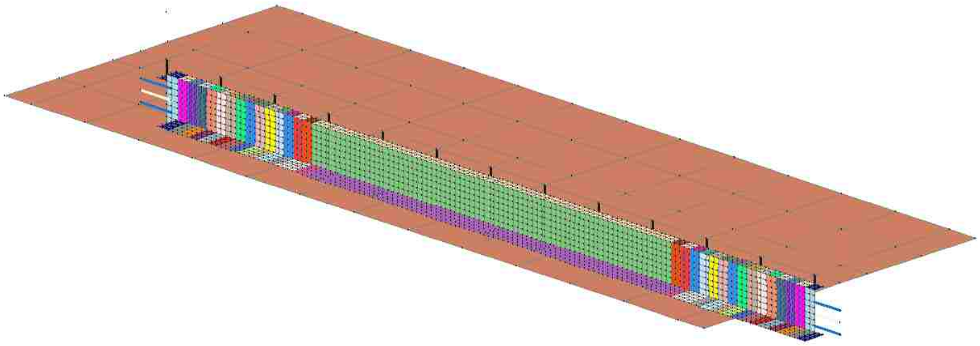

Figure 37 – 3D Shell SAFIR Model Made Realistic

www.manaraa.com

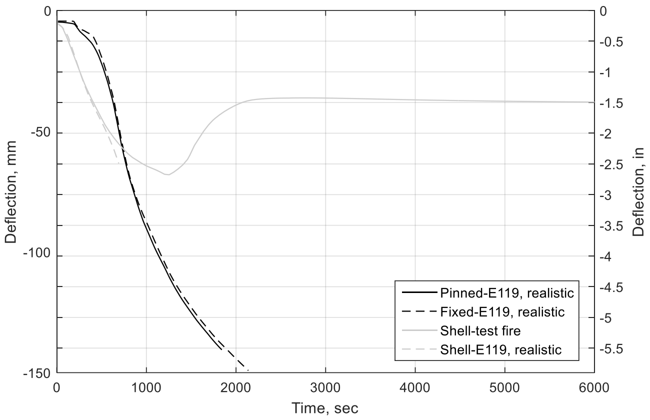

Figure 38 – Beam Deflection Comparison of Realistic Shell Models

Figure 38 shows that the realistic full shell model fails much sooner than the 3D beam models predict. This is mainly due to the numerical instability in the shell model once local buckling occurs. The model cannot stabilize long enough to enter the phase where the beam starts to “hang” and enter into a catenary response. This is a limitation of the current SAFIR model and the model complexity, making the outcome inconclusive. The real behavior of the beam would be bounded between the shell and 3D beam model predictions, and the beam failure time would potentially be similar to the predicted failure from the beam element models.

The two shell models shown in Figure 38 behave quite similar until the point of local buckling that occurs in the realistic model due to the extra stiffness provided in the boundary condition. At this point, the shell starts to follow a similar trajectory as the 3D beam models. If the shell model was able to overcome the numerical instability, it could potentially continue on the path similar to the beam models.

Figure 39 shows the end reactions for the beam and slab for the two realistic 3D beam models and the realistic shell model. In all of the models, both the beam and slab move quickly

www.manaraa.com

into a compressive state. In the 3D beam models, the slab transitions back into tension minutes before failure, while the beam is unable to make the full swing into tension. This shows that the beam does not fully reach catenary where it has lost all of the flexural strength and “hangs”. Both the pinned and fixed models show very similar behavior, proving once again that the end restraint has little effect on the cause of failure. The shell model has much less deviation between the end forces in the slab and beam in comparison to the 3D beam models. The shell model is able to distribute the stresses more evenly across all the shells (i.e. it is not governed by the assumption that plane sections remain plane) and creates a less drastic force couple between the steel and concrete. Since this model fails early and does not progress through the reversal from compression to tension, it is impossible to conclude whether the beam would reach catenary.

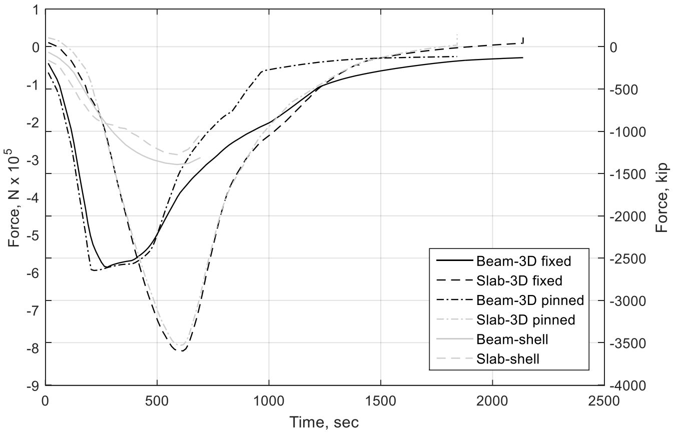

Figure 39 – End Force Reactions of Beams and Slabs

Figure 40 through Figure 43 show the final P-M diagrams for the fixed and pinned beams respectively. The first set of figures represents the beam end element and the second set of figure represents the beam center element.

www.manaraa.com

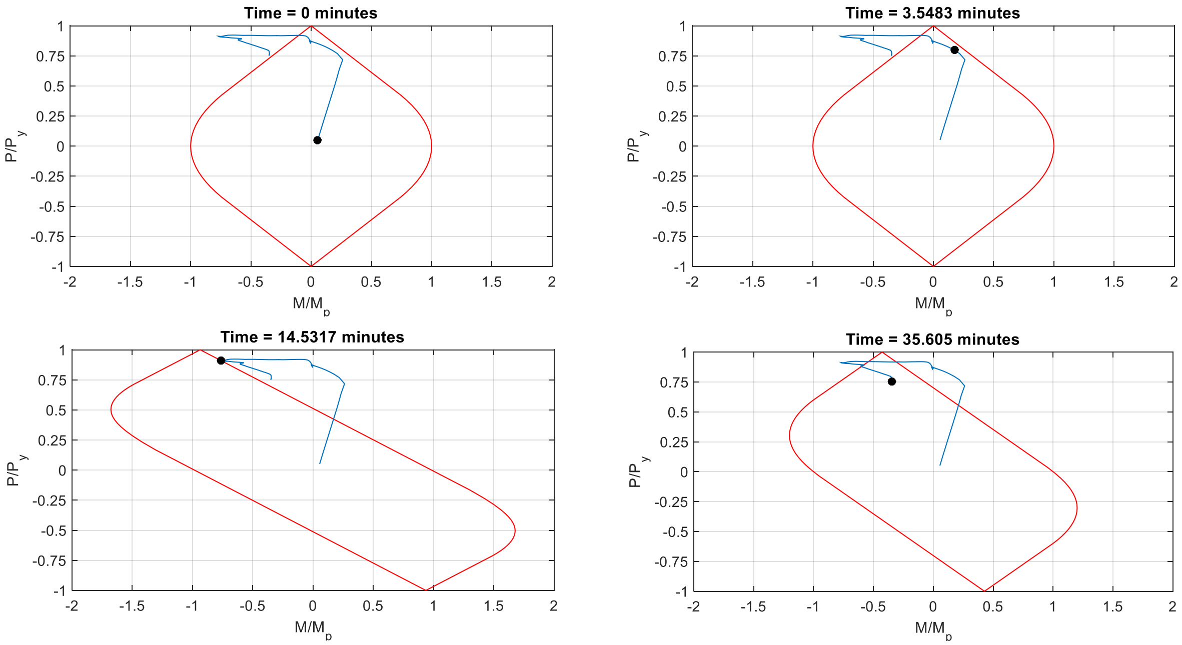

Figure 40 – P-M Diagrams for 3D Fixed Beam at Beam End

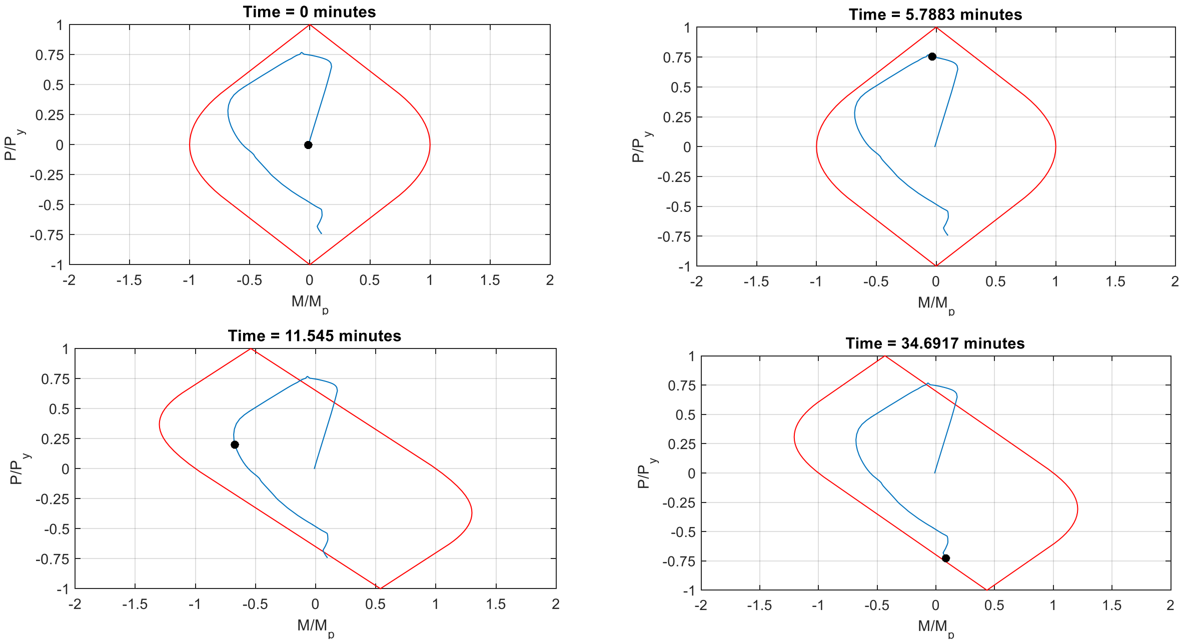

Figure 41– P-M Diagrams for 3D Fixed Beam at Beam Center

www.manaraa.com

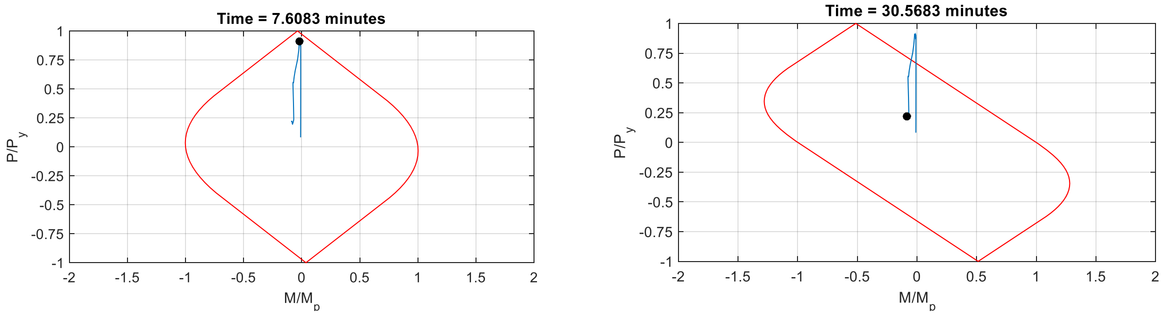

Figure 42 - P-M Diagrams for 3D Pinned Beam at Beam End

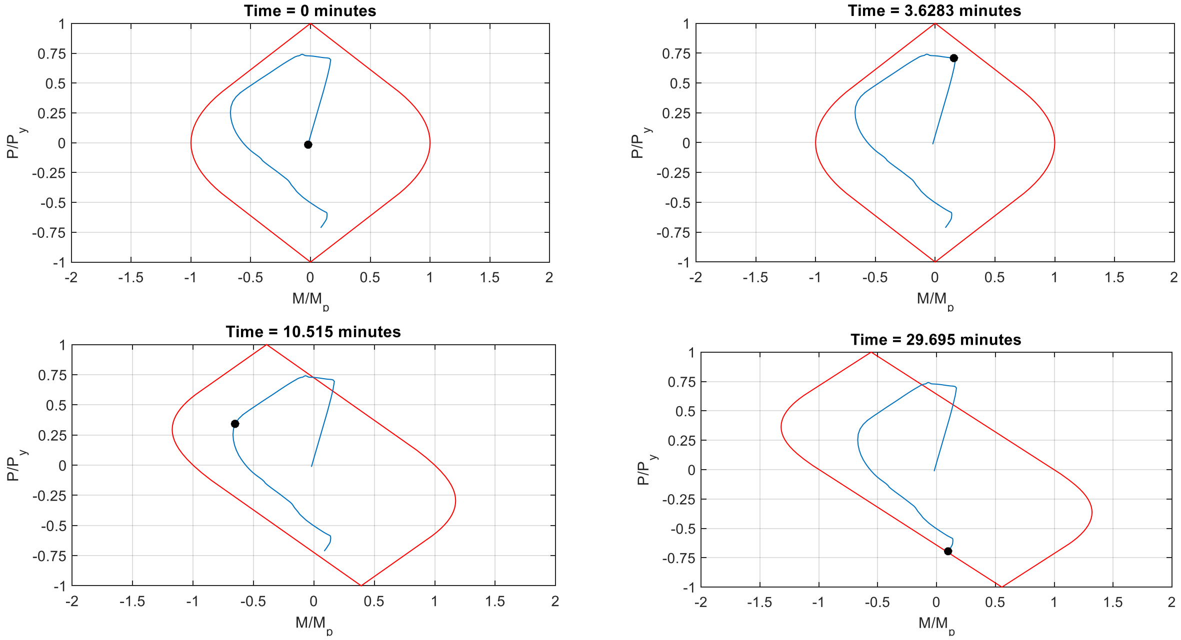

Figure 43 – P-M Diagrams for 3D Pinned Beam at Beam Center

The fixed and pinned beam P-M diagrams look very similar at the beam center, and different at the connection zone, as to be expected. All of the diagrams show that the beam quickly gains compression while staying at a relatively constant moment until it hits the P-M envelope. For the beam center diagrams, the beam gains moment as the compression decreases, and eventually transitions back into tension. The beam hits the envelope again at the point of numerical failure for both models. The beam center is acting similar to a truss

المنارة للاستشارات
www.manaraa.com

chord where axial effects dominate behavior. For the fixed beam, the beam boundary rides along the envelope for the majority of the test, staying at a high axial compression. Near the end of the analysis, the beam loses applied moment until numerical failure. For the pinned beam, the connection is unable to hold moment, which is shown in Figure 42. Both beams fail in a state of compression at the connection, proving that catenary has not been reached.

The SAFIR thermal analysis is used to verify the predictions of failure based on the E119 thermal criteria. The beam cross-section thermal model predicts the maximum thermal limit to be exceeded at 13:20 and the average thermal limit to be exceeded at 12:40. These numbers are similar to what was previously presented for the temperatures from the test. Once again, it is important to note that the beam was able to outlast a 20 minute parametric fire curve with a decay phase, even though failure is predicted at earlier times from the prescriptive methods. A performance based analysis provides information that cannot be obtained from the current prescriptive methods.

4.4 Summary and Conclusions

A case study of a composite beam under a realistic fire curve has been tested, analyzed, and modeled in SAFIR using various levels of complexity. A W8x10 composite beam was tested in the structural furnace at ATLSS with a fire curve that considered the triggering of active protection after 20 minutes. The test revealed a low level of damage during the fire and residual damage after the fire ended. Although E119 thermal criteria predicted failure of the test beam between 11.5-13.5 minutes, the beam was stable after the full fire duration.

The finite element models were able to reasonably predict the maximum beam and column deflections, and agreed with the experimental results by showing that the system could

المنارة للاستشارات
www.manaraa.com

survive the fire. The 2D beam models were attempted and proved to be unable to match the full behavior of a composite system, and therefore may not be suitable in the design or analysis of composite floor systems. 3D beam models were created using fixed and pinned connections and bounded the deflections of the frame. The models show that the shear tab behaves between the two connection states. A partially rigid connection was added to the 3D beam models that allowed better predictions of maximum deflections, but worse predictions of post-fire behavior when compared to the pinned and fixed connections.

A simplified steel temperature calculation was implemented to predict the lumped mass temperatures of the top flange, web, and bottom flange of the beam. These temperatures were compared to the temperatures provided from finite elements and from thermocouple data from the beam specimens during the test. It was shown that the simplified calculation correlates very well with the test and can be used to get a similar and conservative result as the finite element temperatures.

A full shell model was made in SAFIR to capture more complexities of the composite floor system. This model was much more advanced than the beam models, and was able to closely match the deflection data from the test beam and column supports. However, in practice when time and money is a constraint, the 3D beam models with fixed and pinned boundary conditions are able to provide an accurate and conservative estimate of the solution, and therefore can be used. The shell models had trouble converging once instabilities occurred in the system.

The 3D beam models were re-analyzed with boundary conditions that were updated to simulate a real building scenario subject to the E119 standard fire curve. The unprotected

المنارة للاستشارات
www.manaraa.com

W8x10 composite beam was structurally stable for 36 minutes with fixed boundaries and 31 minutes with pinned boundaries. This outcome shows that the two boundary conditions predict relatively similar failure times. When a continuous slab diaphragm is considered, the pinned and fixed beams can behave very similarly up until structural failure. The additional stiffness at a fixed connection can either cause premature system failure or provide necessary stiffness to outlast a pinned connection, depending on the temperature increase and loading.

Moving forward, more research can be done with different parametric fire curves, beam sizes and lengths, and levels of protection to enhance this study. Simplifications can be made to better correlate with industry practices and reinforce performance based design standards. The temperatures of the concrete slab need to be further analyzed to correlate the heat absorption of a modeled flat slab with a realistic corrugated slab.

www.manaraa.com

5.0 Tests 2 and 3

Two further tests on composite floor sections were performed in the ATLSS Furnace. The setup of these steel beams were identical, except one was protected with a SFRM and the other was left as bare steel. From here on out, the unprotected specimen test will be known as test 2, and the protected specimen test will be known as test 3. This study was done as one of the first direct comparisons between protected and unprotected beams.

5.1 Test Setup and Specimen Design

5.1.1 The specimens

Two 10’-11 1/2” long W12x26 beams with a 3.25” lightweight concrete slab (121 pcf) on top of a 2” 18 gage metal deck were designed to be tested in the ATLSS Furnace. The beam size was chosen based on a typical size floor beam for an office building, and the length is what could be accommodated in the ATLSS Furnace. The system was designed with 3/4" diameter, 4” long shear studs at one foot intervals to create composite action. The beam is considered ~30% composite (Vinnakota et al., 1988). The slab was reinforced with 6x6, 10 gage square welded wire fabric located 3/4" below the top of the slab. The beam was perpendicularly framed to a C15x40 channel at each end with a shear tab connection, similar to how the secondary framing beams would be connected to the primary framing beams in an office building. The back of the channel web was bolted onto the flange face of W10x26 columns that spanned through the furnace between the heavy self-reacting steel frame. The columns were pinned on both ends using the same clevis connections as for Test 1. The connection zone, the channels, and the part of the columns inside the furnace were all wrapped with ceramic fiber blanket during the test

المنارة للاستشارات

www.manaraa.com

to prevent them from heating excessively. Figure 44 shows the specimen placement inside the furnace, Figure 45 shows the shear tab connection between the test beam and channel, and Figure 46 shows the connection between the channel and column.

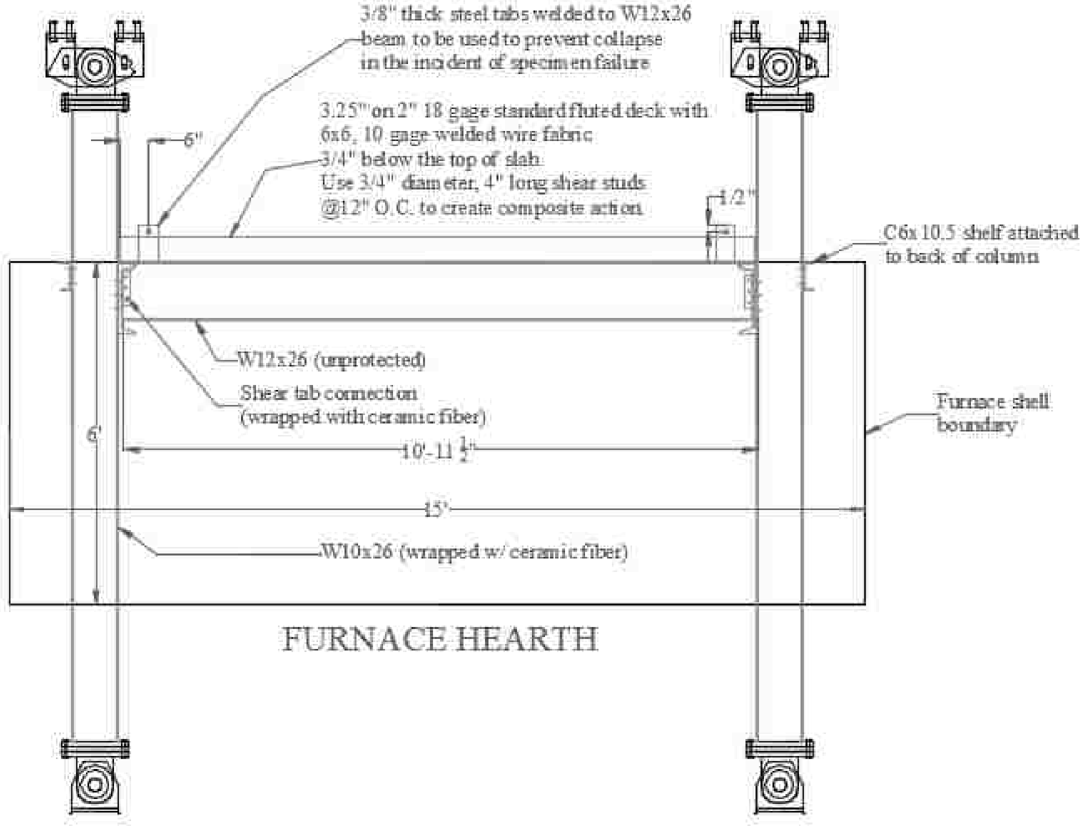

Figure 44 - Test Specimen and Furnace

www.manaraa.com

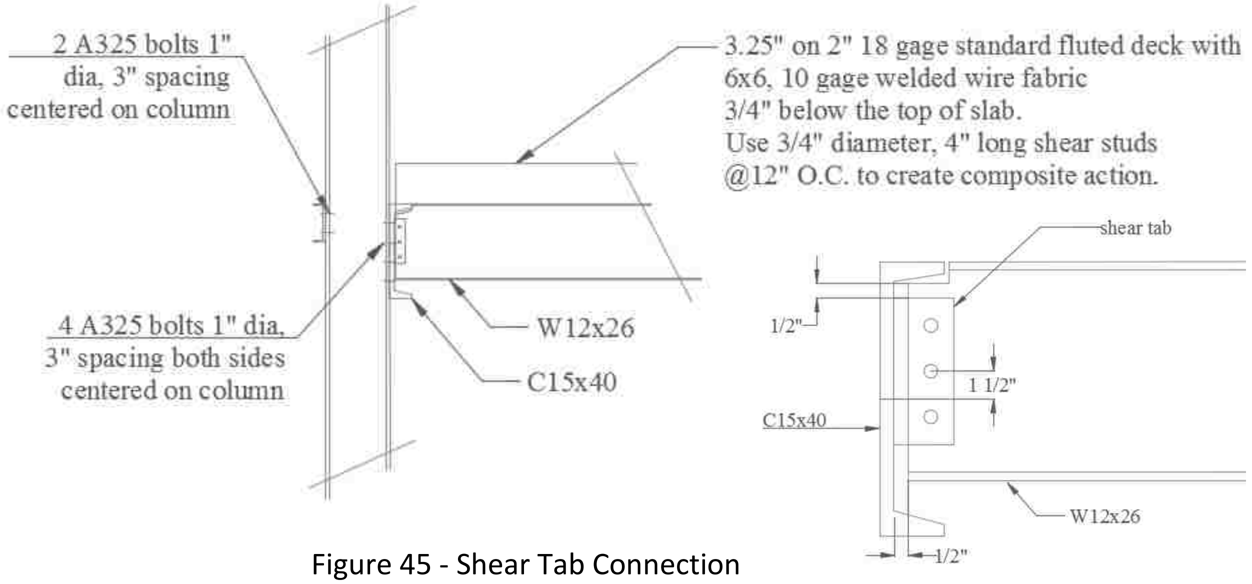

Figure 45 - Shear Tab Connection

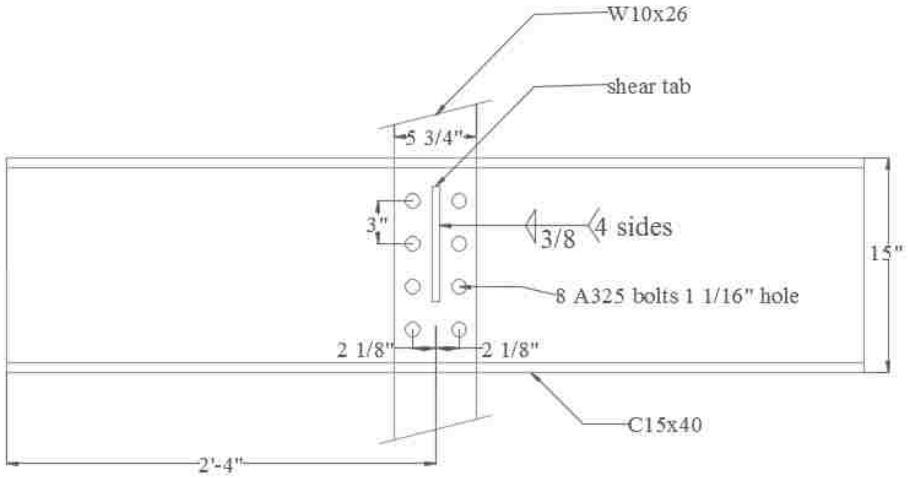

Figure 46 – Channel to Column Bolted Connection

The specimens were designed in accordance with the UL Directory design number D902. The protected beam was designed in accordance with the two hour restrained and unrestrained assembly. Isolatek International sprayed the specimen with CAFCO 300 (Isolatek, 2016), at an average thickness of 7/8” in accordance with section 6C in D902 (Underwriters

www.manaraa.com

Laboraties Inc., 2016) and the SFRM thickness conversion equations in ASCE 29-05 (ASCE, 2005). The calculation of SFRM thickness can be seen in Appendix B.

The slab was poured six months prior to the first test in order to allow time for a full cure and adequate moisture reduction before the test was conducted. Six months was recommended to allow the concrete moisture content to stabilize, thus preventing premature spalling with in the slab during heating. The concrete strength was tested after 28 days and on both test days, and can be seen in Appendix C.

The E119 Standard fire curve was chosen to heat the specimens until failure. The system was instrumented with 58 thermocouples, 4 string pots, and 2 LVDT's to measure the temperature throughout the furnace and structure, and to obtain deflections of the beam and columns. A description of the outcomes of the two tests are to follow. The locations of the instrumentation are as follows:

- 3 thermocouples on web (north, mid, south)
- 6 thermocouples on bottom flange (2 north, 2 mid, 2 south)
- 6 thermocouples on top flange (2 north, 2 mid, 2 south)
- 6 thermocouples on concrete deck (north, mid, south in pairs)
- 6 thermocouples ambient hanging throughout furnace
- 10 thermocouples on connection (1 on each bolt 2 on each shear tab)
- 8 thermocouples on columns (4 on each)
- 4 thermocouples on channels (2 on each)
- 1 thermocouple on overhead frame
- 1 thermocouple on sidewall of furnace

www.manaraa.com

- 4 thermocouples on clevis connections (1 on each)
- 2 thermocouples on LVDT's (1 on each)
- 2 LVDT's on columns (1 on each)
- 2 string pots on beam at midspan
- 2 string pots on columns at top (1 on each)

5.1.2 Load Selection

The specimen was loaded with an enerpak jack at the third points, to most closely represent the moment distribution of a distributed load. The setup of the loading can be seen in Figure 47.

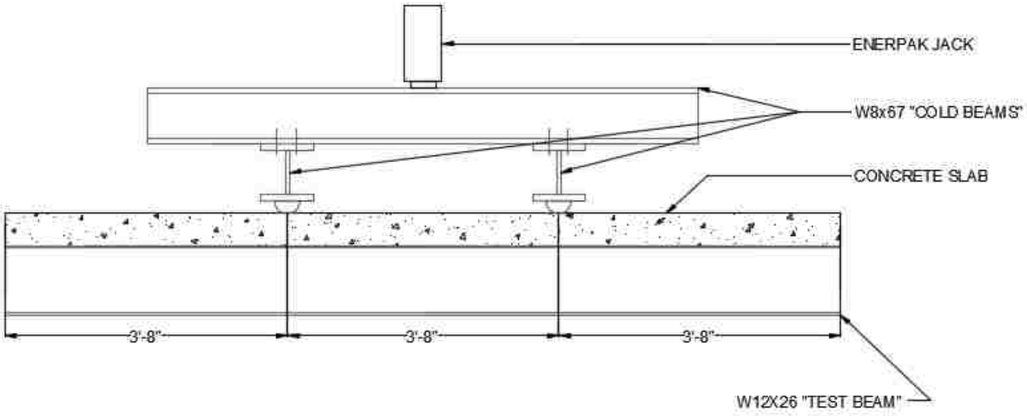

Figure 47 - Specimen Loading Setup

In order to determine the amount of load to apply, two small studies were conducted. First, the W12x26 floor beam was analyzed with the provided dead loads and a standard office live load of 50 psf (ASCE, 2010). When using the standard load combination of 1.2*DL+1.6*LL, the applied moment was about 40% of the composite beam's moment capacity. This analysis was repeated using the standard extreme events load case of 1.2*DL+0.5*LL, and the applied

www.manaraa.com

moment was about 25% of capacity. This study provided the factor of 25/40 that was used to scale between design loads and extreme event loads. A second study was conducted with the W12x26 at four different lengths – 15’, 20’, 25’, and 30’. For each length, the maximum allowable deflection of the beam was taken as L/240 (where L is the total applied load), and the maximum distributed live load was back-calculated based on the deflection limit and the standard load combination of 1.2*DL+1.6*LL. The applied bending moment for each beam was calculated, as well as the percent capacity represented by that moment. The 25/40 factor was used to scale down the capacity for the scenario of extreme loading. Table 3 shows the outcomes of this calculation process for each beam length. The last column shows the percent of moment capacity that would be applied to a typical framing beam during an extreme event. Based on this study, an applied moment of 25% capacity was chosen to prevent excessive overload on the beam lengths selected for the parametric study. On the test beam, the moment was created with two point loads of 17.75 kips loaded at the third points (see Appedix A for beam design calculations).

Table 3 – Moment Capacity Calculation for W12x26 at Various Lengths

Length (ft)	**L/240 (in)**	**w_{max} (k/ft)**	**w_{LL} (k/ft)**	**M_{app} (k*ft)**	**% Capacity @ 1.6LL**	**% we want @ 0.5LL**
15	0.75	5.03	4.76	223.45	81.55	50.97
20	1	2.12	1.85	164.46	60.02	37.51
25	1.25	1.09	0.82	127.43	46.51	29.07
30	1.5	0.63	0.36	101.06	36.88	23.05
E=	29000	ksi				
I_{eff}=	263.6	in^4				
w_{DL}=	0.271	k/ft				
M_{cap}=	274	k*ft				

www.manaraa.com

The beams were designed based on standard practice (AISC, 2010) and resulted in ~30% composite action (see appendix A). However, it has been shown in previous research that partially composite beams behave increasingly composite (eventually reaching fully composite) under fire exposure (Wang et al., 2016). For example, Figure 48 shows the percent composite of the unprotected beamused in this study, as calculated usign the AISC design equations, plotted over time. This figure is based on a SAFIR temperature model of the middle of the beam during an E119 fire. As the temperature increases faster in the beam than in the slab, the yield strength of the steel decreases, which increases the percent composite. After about 15 minutes of heating, the beam is acting as fully composite, which supports the research shown in Wang et al. (2016). Figure 49 shows the same graph for the protected case. This case doesn't get us to a fully 100% composite beam, but still increases with time as the steel heats up.

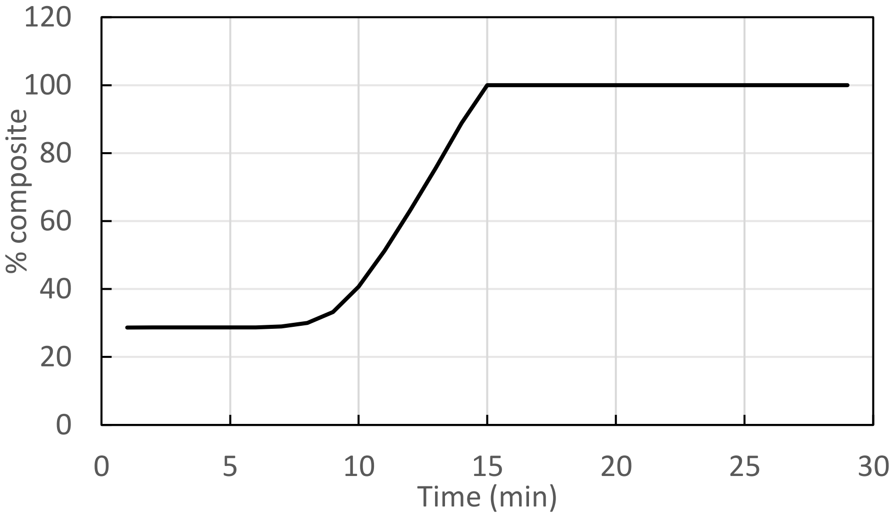

Figure 48 - Percent Composite of Unprotected Beam

www.manaraa.com

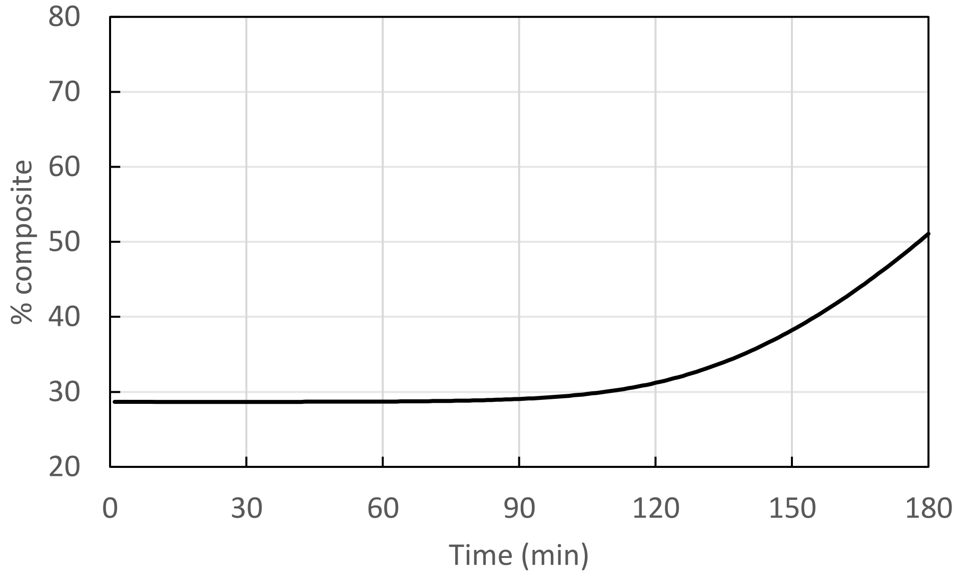

Figure 49 - Percent Composite of Protected Beam

5.2 Test 3 – Protected Beam

5.2.1 Description of the Protected Beam Test

The protected specimen was tested for 2:18:45 before failure was reached and the furnace was shut off. This is the longest test ever performed on this furnace, and the equipment performed well. Channels were not clamped across the furnace walls for the test, and small amounts of vibration were noticed in the walls as the furnace heated rapidly (about the first 30 minutes of the test). This vibration was not enough to impede on the test, but in the future channels should be clamped across the top edges to prevent the vibration. A photo of the specimen after the test and the removal of the furnace wall can be seen in Figure 50. It can be seen that chunks of the SFRM fell off the top and bottom flanges during the test, as well as the bottom of the metal decking.

www.manaraa.com

Figure 50 – Protected Beam after Failure

This specimen was tested 182 days after the concrete slab was poured. The concrete did not spall during the test, but popping sounds were heard after about 15 minutes from the furnace start. Wet spots could be seen on the top of the slab for the next 25 minutes, where water was released through the pours of the concrete. The first chunk of SFRM was seen to fall off the metal decking at about 33 minutes, and off the steel about 2 minutes before the specimen failed. A high temperature camera was used to capture this detail. Failure was determined when the rate and magnitude of beam deflection dramatically increased and the furnace no longer had a seal at the top. The concrete slab had cracked along the middle and underneath both loading beams as seen in Figure 51. The slab began to crack and deflect at the location with SFRM damage, though the more rapid accumulation of deflection at this location didn’t occur until near the end of the test when the beam was rapidly deflecting and losing strength overall.

www.manaraa.com

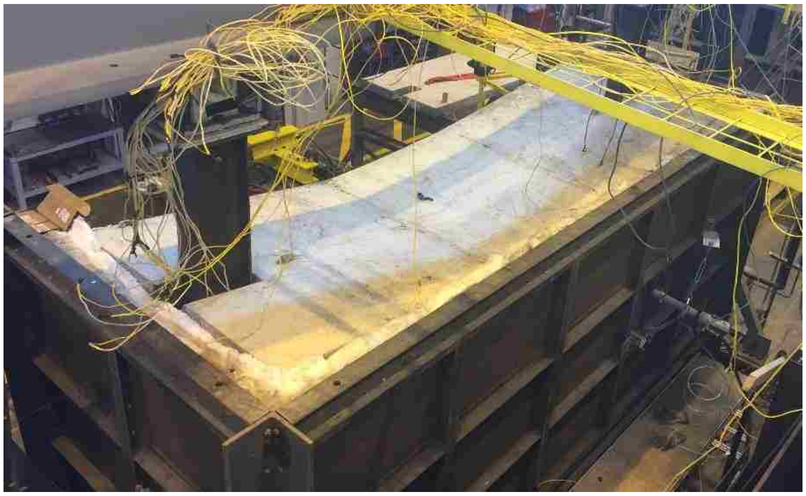

Figure 51 – Test 3 Slab Post Test

Once the specimen had cooled, the fiber blankets were removed from the columns, channels, and connections, and all elements were inspected. A 4” chunk of the SFRM was missing from the bottom flange, and many chunks of the SFRM had fallen off the top flange, as shown in Figure 52. The columns experienced significant permanent deflection and would need to be replaced for future testing. The channels didn’t have permanent deformation, and are able to be used in future tests. The top bolt head on both ends at the beam to channel connections had been sheared off during the test, the middle and lower bolts stayed intact but experienced permanent shear-induced deformations. Figure 53 shows the warping in the beam’s connection holes after the test, with close ups on the top two holes. The warping is hardly visible in both end tab connections.

www.manaraa.com

Figure 52 – SFRM chunks missing on flanges

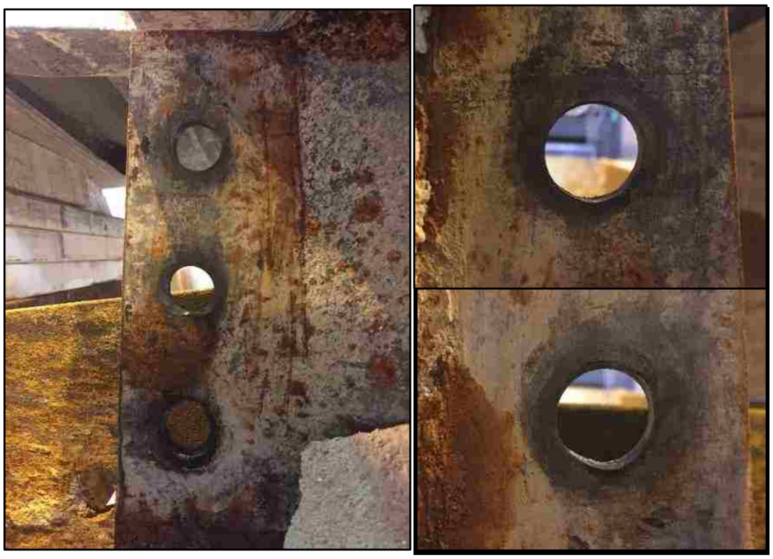

Figure 53 – Test 3 Beam End Connection Holes

At failure, the bottom flange of the beam twisted slightly out to one side, as shown in Figure 54 looking down the length of the beam from each direction. This state indicated lateral torsional buckling in the beam’s bottom flange. The top flange did not disconnect from the metal deck anywhere along the length.

المنارة للاستشارات

www.manaraa.com

Figure 54 – Test 3 Beam Twist at Failure

Six thermocouples were used to measure the ambient temperature in the furnace. One of these thermocouples malfunctioned during the test and produced erroneous results - the other five are shown in Figure 55 along with the standard E119 curve and average furnace temperature.

www.manaraa.com

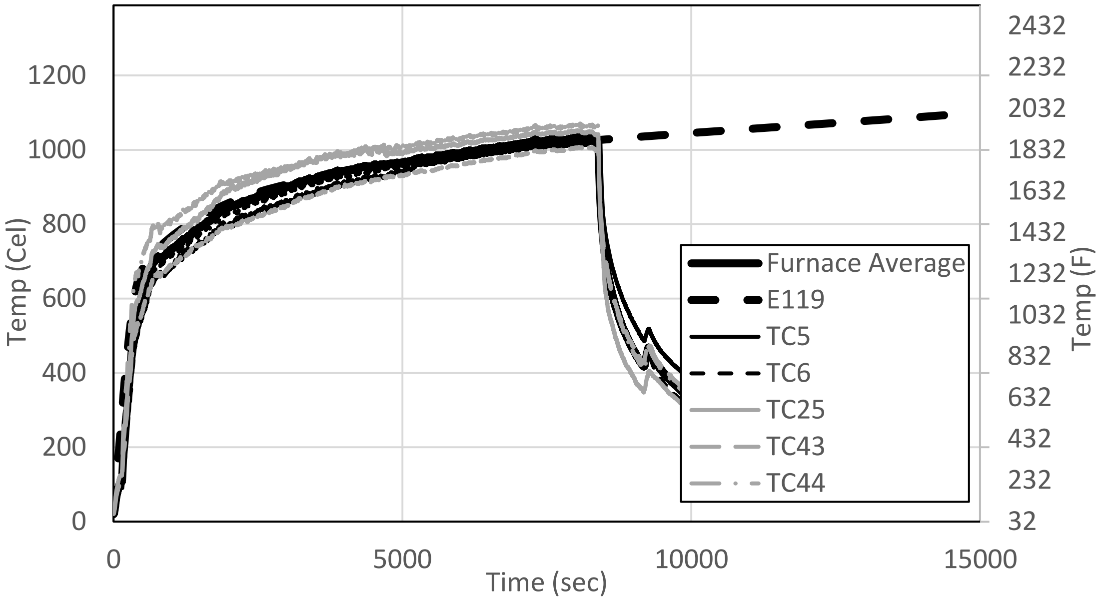

Figure 55 – Test 3 Ambient Furnace Temperature

Figure 55 shows that the furnace temperature average is very similar to the E119 standard curve. According to the E119 standard (ASTM, 2014), the area below the E119 standard curve must be within 5% of the area under the test curve for a test 2 hours or longer. For this test, the two areas are within 1.41%.

The columns were each instrumented with six thermocouples to obtain the temperature at various locations near the connections. Figure 56 shows the average column temperature throughout the test.

www.manaraa.com

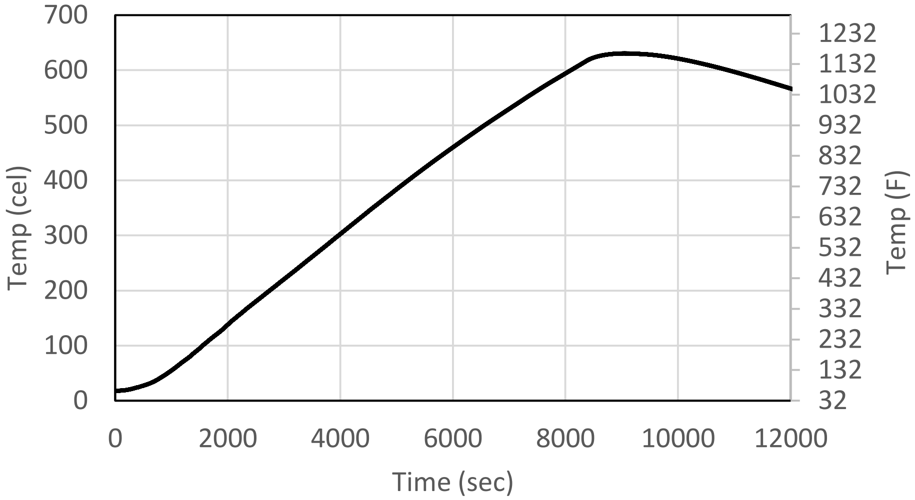

Figure 56 – Test 3 Average Column Temperature

Although the columns were wrapped with ceramic blanket, they still reached average temperatures greater than 600°C during the test due to the significant duration of fire exposure. Since the properties of steel weaken at these temperatures, the length of the columns that were inside the furnace were modeled as uniformly heated at the temperature time history shown in Figure 56. The lengths outside of the furnace were left approximated as cold. The models were checked to make sure no local buckling or irregularities occurred at the transition zones.

The beam was instrumented with 15 thermocouples, five in the middle of the beam and five at the quarter points. At each location, there were two thermocouples on each flange (one on each side of the beam) and one thermocouple on the web. Figure 57, Figure 58, and Figure 59 show the temperatures throughout the test at the south end, midspan, and north end, respectively.

المنارة للاستشارات
www.manaraa.com

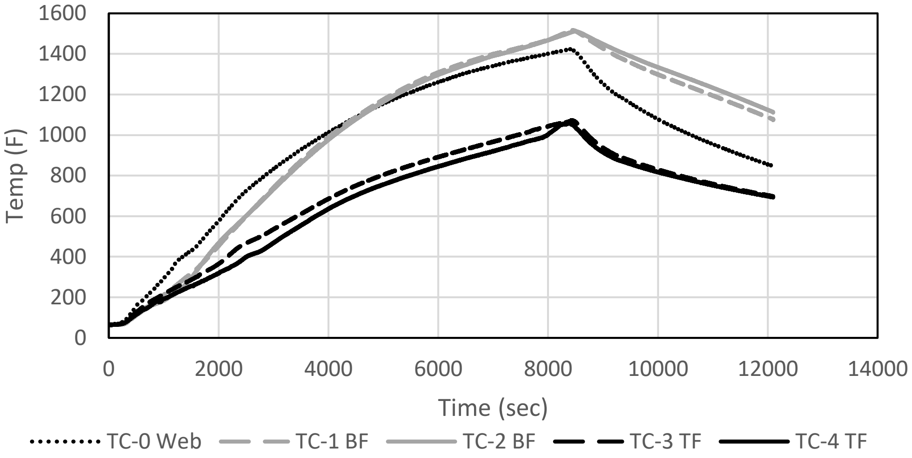

Figure 57 – South End Beam Temperatures

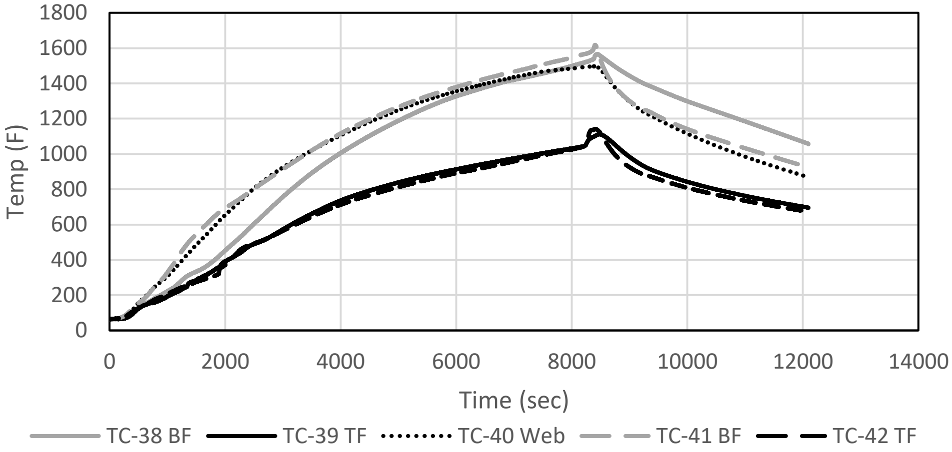

Figure 58 – Midspan Beam Temperatures

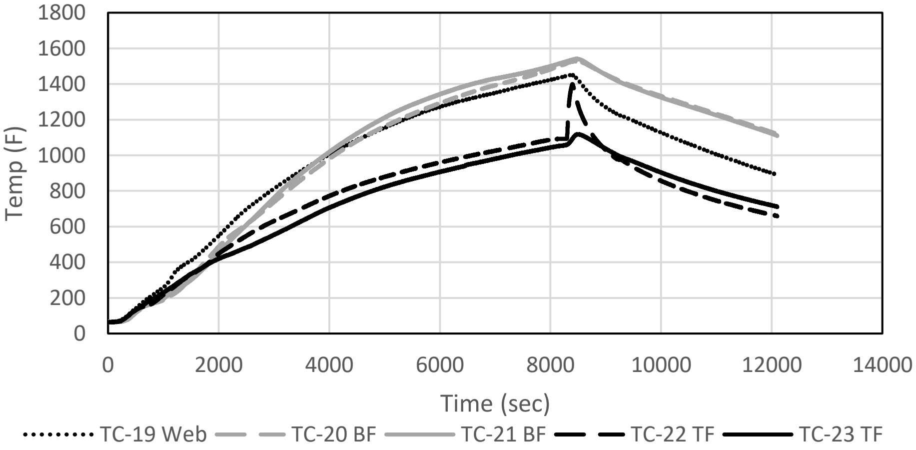

Figure 59 – North End Beam Temperatures

www.manaraa.com

Figure 59 shows a large spike in TC-22 corresponding to a location on the top flange. This spike is most likely caused when a chunk of the SFRM fell off the beam's top flange near this location, moments before failure. All three figures show that the top flange temperature spiked before at least somewhat failure.

The E119 standard failure criteria states that failure of an unrestrained beam is reached when the maximum temperature of the beam hits 1300°F or the average temperature of the beam hits 1100°F. In the test, the first condition was met at 1:40:45, and the second condition was met at 1:28:01. According to this criteria, the beam would not be qualified for a two-hour unrestrained fire rating. However, the test beam falls into a category of semi-restrained, which is not specified in the E119 criteria. Due to the short span, the beam never fails the deflection criteria given for fully restrained beams. The test shows that the beam was able to survive for 2:18:45 seconds, proving that it is able to achieve more than 2 hours of structural fire resistance.

5.2.2 Thermal Analysis for Protected Beam

The temperatures of the beam were modeled through a 2D SAFIR analysis and a lumped mass calculation performed in MATLAB (see Appendix E). In both analyses, the properties of the SFRM were modeled as temperature dependent (Kodur & Shakya, 2013). Figure 60 shows the comparison of the two analyses with the thermocouple data from the test averaged for each plate.

المنارة للاستشارات
www.manaraa.com

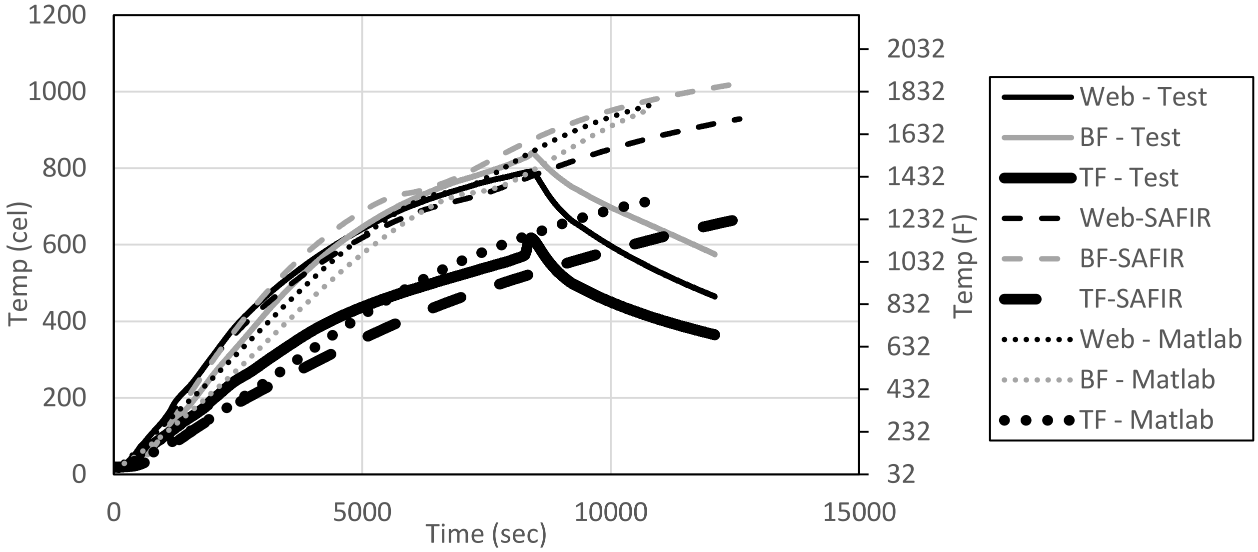

Figure 60 – Test 3 Beam Temperature Analysis Comparison

Figure 60 shows that the MATLAB program tends to slightly under predict the temperatures from the test, and the SAFIR analysis is very close for the bottom flange and web, and slightly low for the top flange.

Two thermocouples were placed on the top of the slab to measure the heat flow. These thermocouples were also compared with the SAFIR 2D thermal analysis to see if the temperatures of the slab were predicted accurately. A section of the slab with the ridges was created using GiD software (CINME, 2016), and thermally analyzed in SAFIR. Figure 61 shows the slab section with ridges. Two frontiers were used, as shown in Figure 61. The bottom of the slab was heated with the E119 curve (frontier 1), and the top surface was exposed to ambient conditions of 20 degrees Celsius (frontier 2). The heat flow between the layers of the slab is shown by the colored gradients.

المنارة للاستشارات
www.manaraa.com

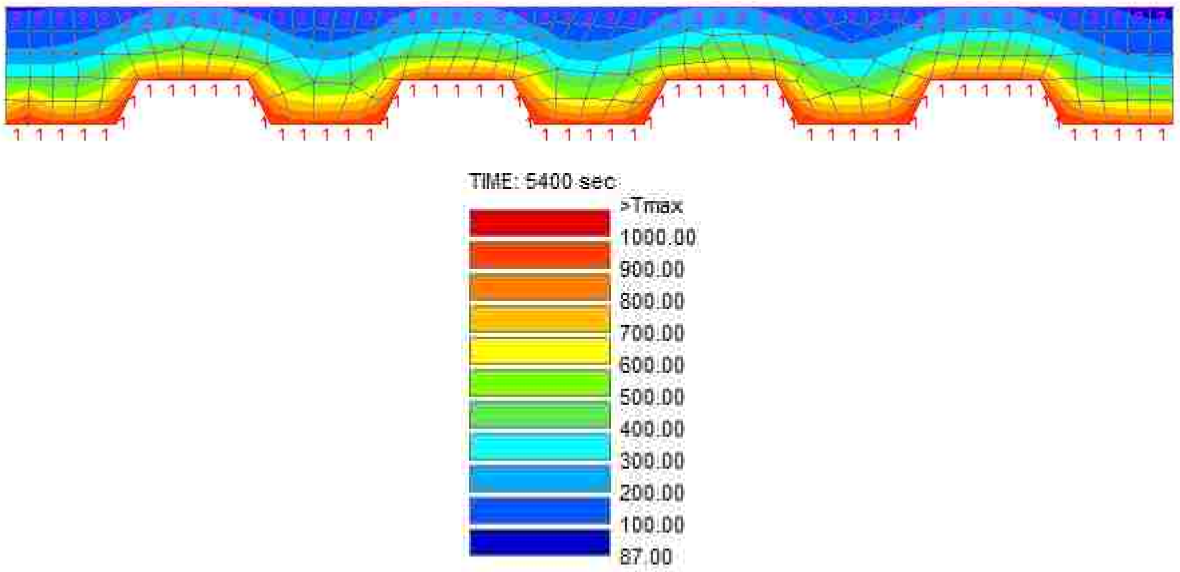

Figure 61 – Profile of Slab with Ridges Modeled

Figure 62 shows the temperature data from the profile of the slab with ridges. Four points were taken throughout the thickness of the slab, with one being the closest to the fire and four being the top of the slab. The four points were taken at the same elevation in both the thick and thin sections of the slab, and plotted against each other to see the variation of temperature between the ridge and trough. The average of the thick and thin sections were also plotted. As expected, the thin sections of the slab get hotter than the thick sections, because there is less concrete for the same amount of heat to travel through. Location 1 at the bottom of the slab and location 4 is at the top of the slab.

www.manaraa.com

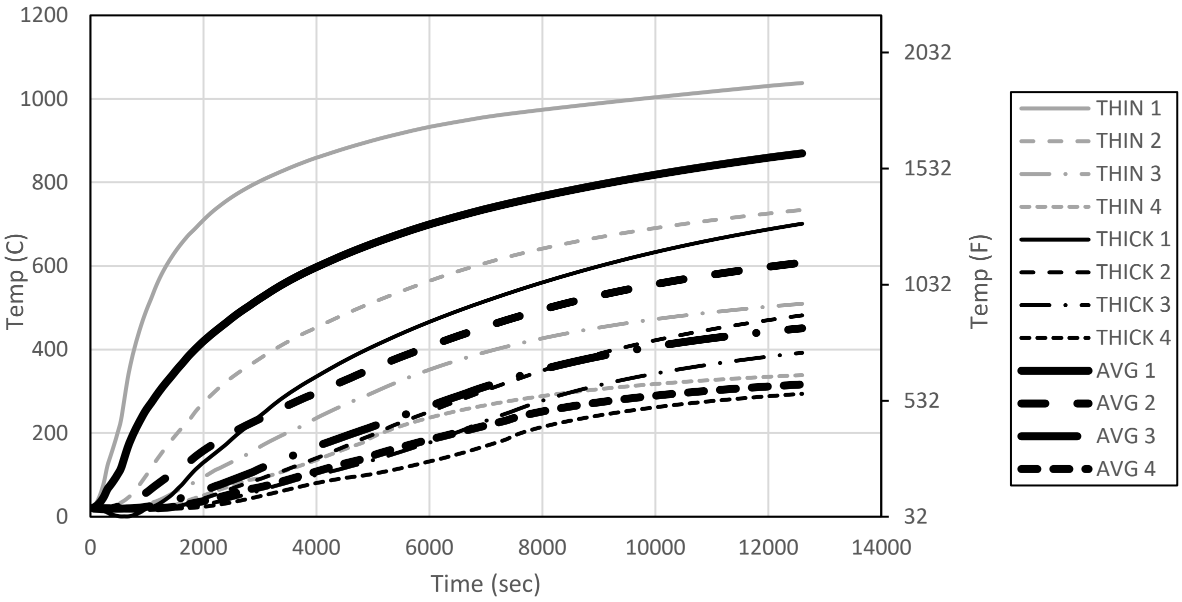

Figure 62 – Slab Temperature Thick and Thin Comparison

The average temperatures through the 3.25” minimum thickness, shown in Figure 62, are compared to the temperatures at the same four location of a flat slab that is uniformly 3.25” thick. Figure 63 shows the comparison of these slab temperatures. The average temperatures from the slab with ridges are significantly lower than the temperatures from the slab without ridges, and this decrease is not uniform for each of the four locations through the thickness. Future research will develop adjustment factors to scale thermal calculations for a uniformly thick slab to approximate the realistic temperature distribution due to the corrugation. This paper will move forward using the average temperatures in the minimum thickness across the entire width of the corrugated slab (i.e. averaging both the thick and thin portions) to characterize the slab in these analyses.

www.manaraa.com

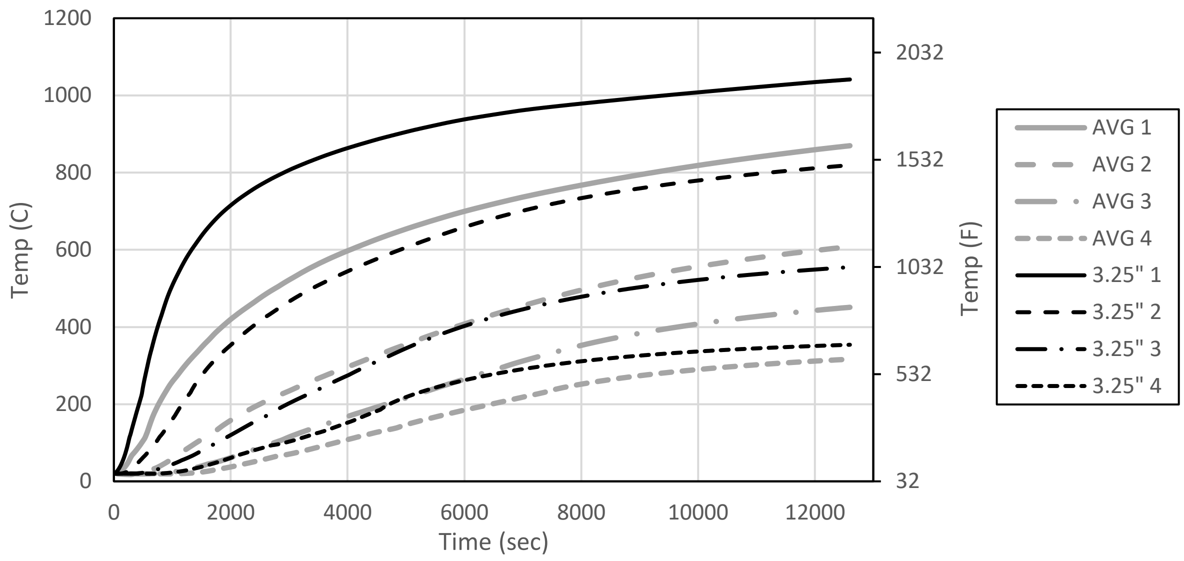

Figure 63 – Ridge and Flat Slab Temperature Comparison

5.2.3 Structural Analysis for Protected Beam

The tests were modeled in SAFIR using five different methods. First, 2D models were created using a perfectly fixed and perfectly pinned boundary condition between the beam and column. These models were simplistic. The steel section and the slab were modeled as one entity in the thermal model, and as two separate entities in the structural model. The thermal models were analyzed with the E119 fire curve for three hours. This created an output of temperature verses time for every discretized fiber in the cross section of the composite beam. The section was discretized into 1270 elements, of which 204 were steel, 536 were the SFRM, and 530 were concrete. This data was then used as input for a structural model of the experimental assembly using fiber-beam elements for the composite beam and the columns. The channels were neglected in the 2D structural models since out-of-plane behavior is not included. The columns were kept cold, and the beam referenced the thermal model to acquire

www.manaraa.com

temperature data. These 2D models were made in a similar way to the 2D models in the previous study (see section 4.2.1).

Next, 3D beam models were created with the slab modeled with shell elements. The slab had temperature readings four times along its depth. The channels between the beam ends and columns were added into this model as spanning in the third dimension. The beam ends were connected to the channel, which was then connected with full translational and rotational constraint to the column. Once again, two models were made, one with perfectly fixed and one with perfectly pinned boundary conditions between the beam and channels. The lateral span of the slab over the channel was supported by the channel via a vertical translational constraint – not other constraints were input between the slab shells and the channel. The channels and the portion of the columns outside of the furnace were assumed to be cooler throughout the analysis. The time temperature curve found from the thermocouples located on the column was used to heat these elements, as described in Figure 56 for the protected beam and Figure 78 for the unprotected beam. For these models, the beam and slab were modeled as separate entities in both the thermal and structural models. These 3D beam models were made in a similar way to the 3D models in the previous study, with the slab reinforcement and shear studs input into the model to best match the test setup (see section 4.2.1).

Lastly, a shell model was created that used shell elements for both the beam and the slab. This shell model was constructed in the same manner as the shell model from the previous study (see section 4.2.5). The imperfections in the beam were calculated using a d/500 parameter, similar to before. For the W12x26 beam, the web imperfection was 0.0197” and the

المنارة للاستشارات
www.manaraa.com

flange imperfection, based on geometry, was 0.0123”. Seven wavelengths were input into the web and flange for the 11’ beam, based on an aspect ratio of 1:3.1.

First, the models were analyzed with the test temperatures from the thermocouples on the beam as input to the structural model. This allowed the models to show how well they could predict the structural behavior when the beam temperatures fully match. Figure 64 and Figure 65 show the beam and column deflection, respectively, for these models. The 2D models were not analyzed using this method, since it was previously shown that they have difficulty predicting behavior the composite beam behavior.

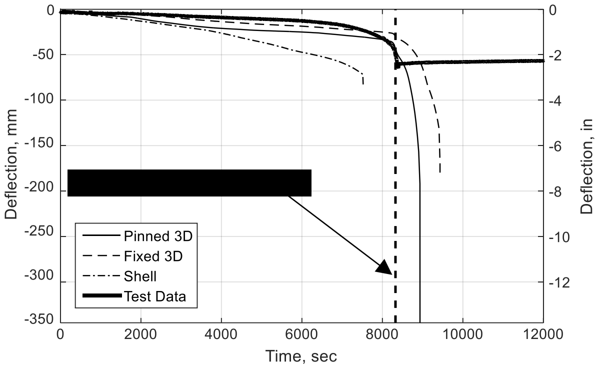

Figure 64 – Test 3 Beam Deflection (Test Temps)

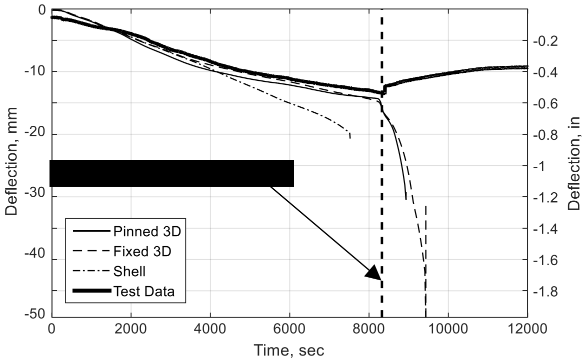

Figure 65 – Test 3 Column Deflection (Test Temps)

The 3D pinned and fixed cases predict the beam and column deflections very well, as well as the failure time of the system. The shell is slightly more flexible than the test specimen, and slightly over predicts deflections and conservatively predicts the failure time. These figures verify that the models are structurally accurate and can be used to reasonable estimate behavior when beam temperatures are known.

The following Figure 66 through Figure 68 show the plastic Axial-Moment (P-M) diagrams for the fixed beam ends, fixed beam center, and pinned beam center. The fixed beam

www.manaraa.com

shows that the beam ends do not hold experience large normalized axial force until minutes before failure, where the beam center enters into a state of high tension towards the end of the test. The pinned beam center behaves very similar to the fixed beam center. The greatest difference occurs when the pinned beam hits the envelope boundary and fails quicker than the fixed beam. This is similar to what has been shown for previous models, where the pinned connection has more flexibility than the fixed.

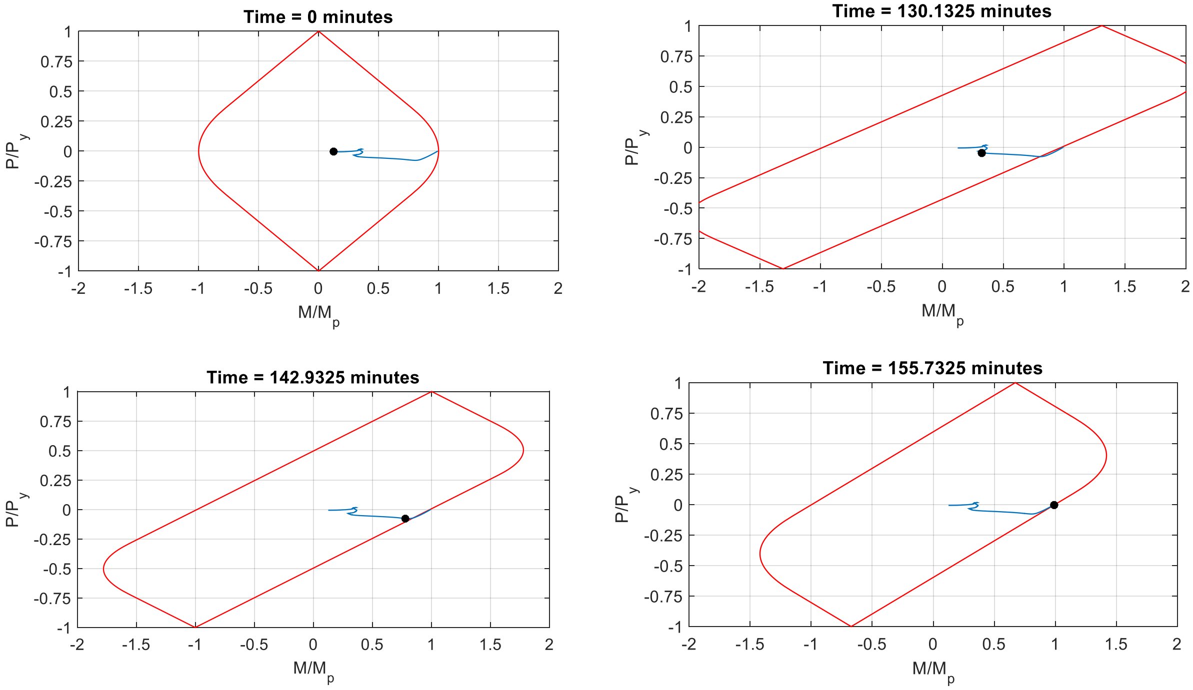

Figure 66 – Test 3 P-M Diagram for Fixed Beam Ends

www.manaraa.com

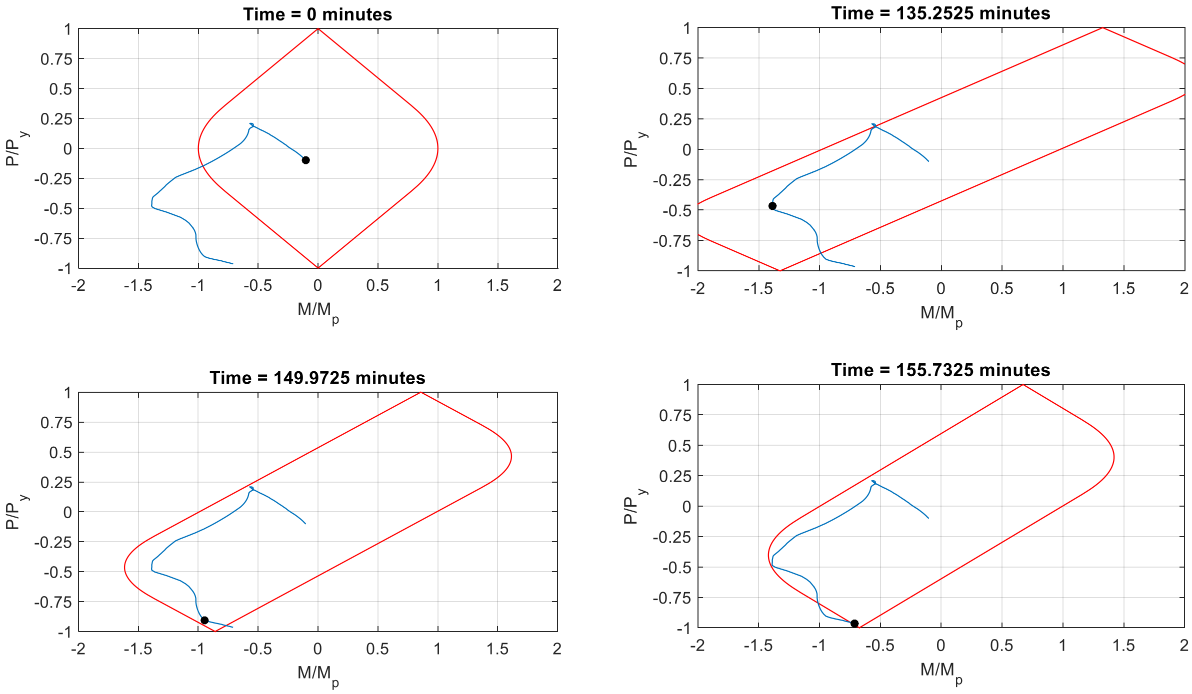

Figure 67 – Test 3 P-M Diagram for Fixed Beam Center

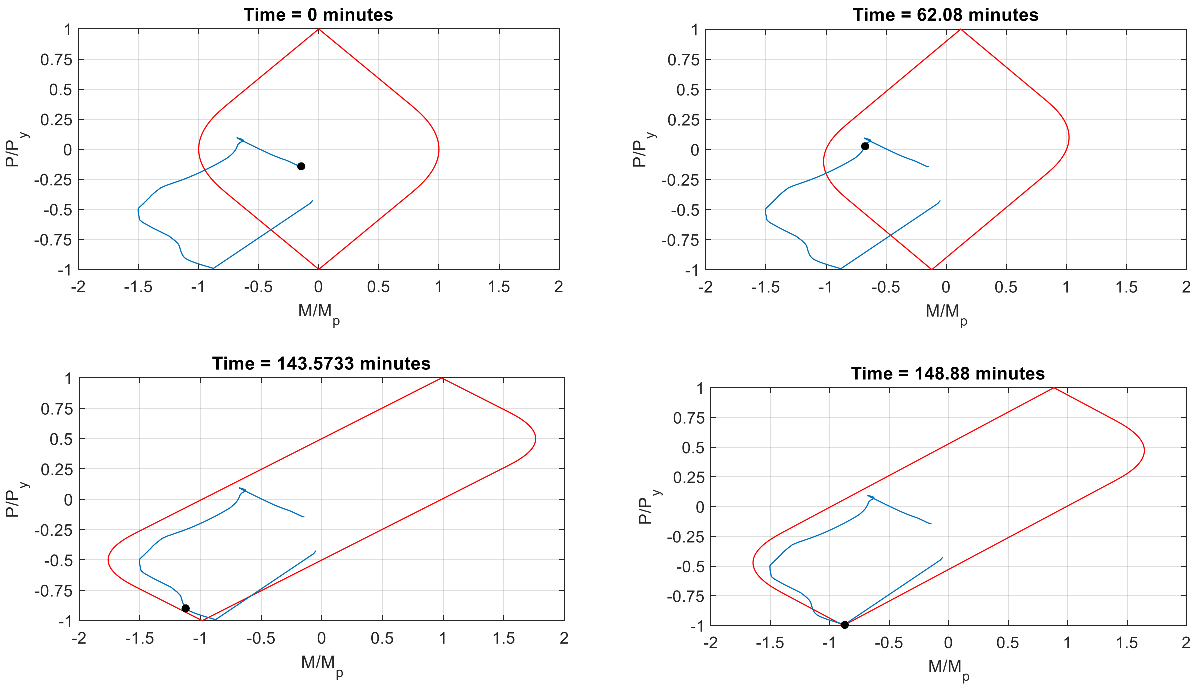

Figure 68 – Test 3 P-M Diagram for Pinned Beam Center

المنارة للاستشارات
www.manaraa.com

The next set of models were ran with the temperatures provided from the thermal SAFIR analysis instead of the test temperatures. The deflections from these models can be seen in Figure 69 and Figure 70 for the beam and column respectively. It is shown that the predictions are increasingly conservative when the SAFIR temperatures are used versus the test temperatures. However, the prediction of failure time still shows good agreement with that observed during the test, and all 3D models provide conservative predictions of deflection.

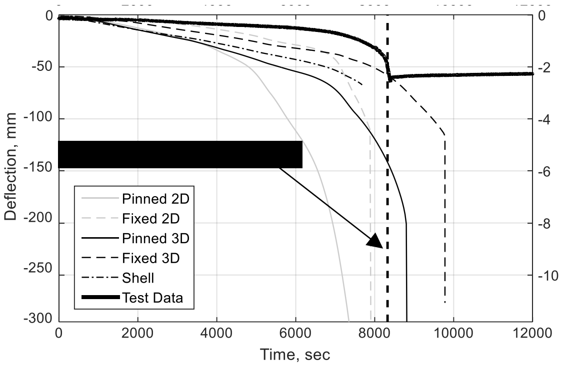

Figure 69 – Test 3 Beam Deflection (SAFIR Temps)

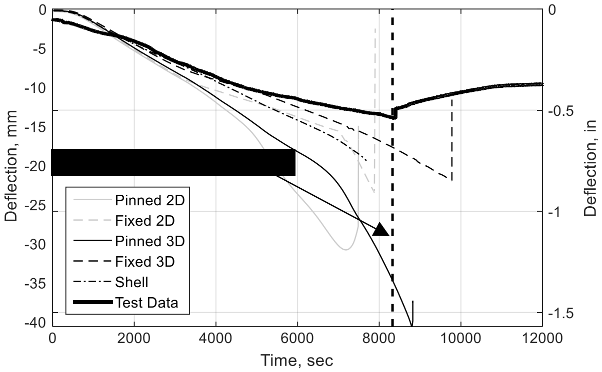

Figure 70 – Test 3 Column Deflection (SAFIR Temps)

Similar to Figure 64 and Figure 65, Figure 69 and Figure 70 show that the shell model predicts a slightly earlier failure time than the 3D beam models. In examining the shell models, the bottom flange begins to slightly twist at failure similar to what was described in the test (shown in Figure 54). This damage mode makes it difficult for the shell model to continue to numerically converge, even though the beam realistically has some remaining capacity after the torsional buckling begins.

The fixed models for the 2D and 3D beams match the test data closer than the pinned models since the increased fixity in the connection allows less beam deflection throughout the test. This shows that the shear tab connection may behave closer to a fixed connection rather

المنارة للاستشارات
www.manaraa.com

than a pinned connection in extreme heat, contrary to common design assumptions. As described for the first test, this phenomenon could be partly due to the connections being kept relatively cool during the test by the ceramic fiber blanket. This change in temperature between the connections and beam provides more stiffness to the connection, resulting in behavior that trends toward a fixed boundary.

5.3 Test 2 – Unprotected Beam

5.3.1 Description of the Unprotected Beam Test

The unprotected specimen was tested for 28:15 before failure occurred, as indicated by rapidly increasing beam deflection. At this time the furnace was shut off, and the applied load was removed. The beam was allowed to cool for several hours before the data acquisition was turned off to capture the stabilized residual state. A photo of the specimen after the test and the removal of the ceramic insulation blankets on the connections and channels can be seen in Figure 71.

Figure 71 – Unprotected Beam after Failure

www.manaraa.com

The beam experienced moderate local buckling in the bottom flange and the web near the connections, just past where the ceramic blankets ended. The beam experienced lateral torsional buckling on the bottom flange along the heated length. This type of failure only occurs in the portion of the beam that experiences compression. Under typical gravity loads, the top flange holds compression, but is braced in a composite system. In a fire, the bottom flange of a secondary framing beam would get hotter quicker than the top flange due to the beam orientation. The bottom flange tries to expand at a quicker rate than the top, and pushes against the connections, causing the flange to go into compression. If the compression is high enough, lateral torsional buckling is a concern, as seen in the test beam. Figure 72 shows the permanent deformation that formed near the connection, which happened at both ends. Figure 73 shows the buckling of the beam looking down its length.

Figure 72 – Plastic Hinge in Unprotected Beam

www.manaraa.com

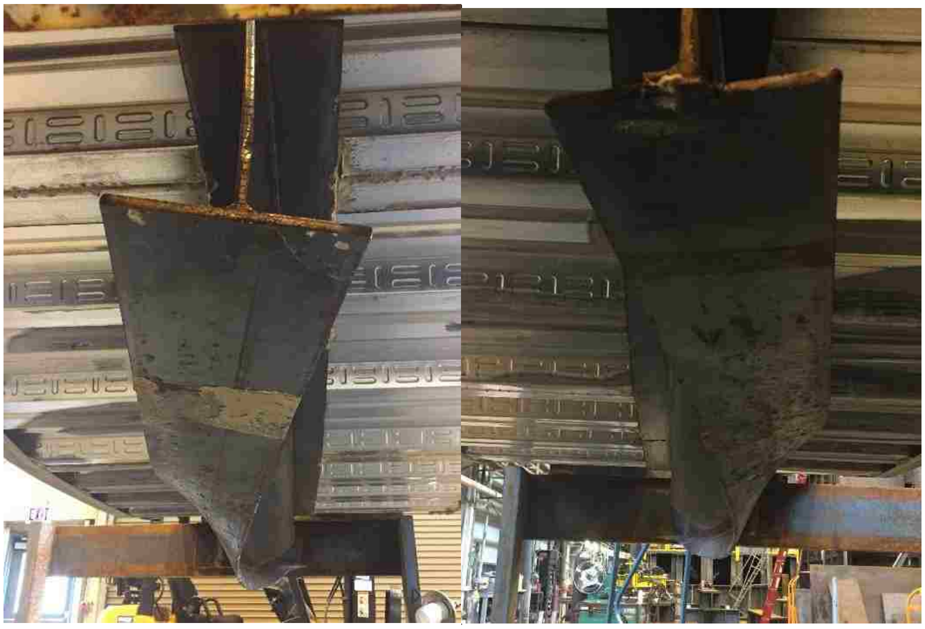

Figure 73 – Lateral Torsional Buckling in Bottom Flange

The end of the beam on the north side experienced some rupture in the web to bottom flange connection. This is most likely due to the beam forcefully compressing into the column face such that the steel could not longer withhold its internal forces. A photo of this rupture can be seen in Figure 74.

Figure 74 – Rupture in Web to Flange Connection

المنارة للاستشارات
www.manaraa.com

This specimen was tested 274 days after the concrete was poured. Wet spots were visible on the concrete after about 20 minutes of heating, but spalling due to high moisture content was never encountered. Popping could be heard throughout the test, with the frequency of popping increasing in the last 5 minutes of the test. Failure was determined when the specimen began to deflect so quickly that it would have been considered “runaway failure”. Once the applied load and the furnace temperatures were removed, the specimen only rebounded about 1/4", signifying that very little strength remained. The slab had relatively few cracks visible in the top except for large lateral cracks below the loading beams. Crushing of the concrete could be seen at the edges of the slab below the loading beams where the slab experienced high compressive forces. The top of the slab after the test is shown in Figure 75.

Figure 75 – Unprotected Beam Top of Slab

None of the bolts sheared apart during this test, but the bolts were slightly deformed and were jammed such that large wrench forces had to be applied to remove them from the connection after the test. The bolts holes were warped due to the connection experiencing large axial reactions and rotation. Photos of the warped holes can be seen in Figure 76.

المنارة للاستشارات
www.manaraa.com

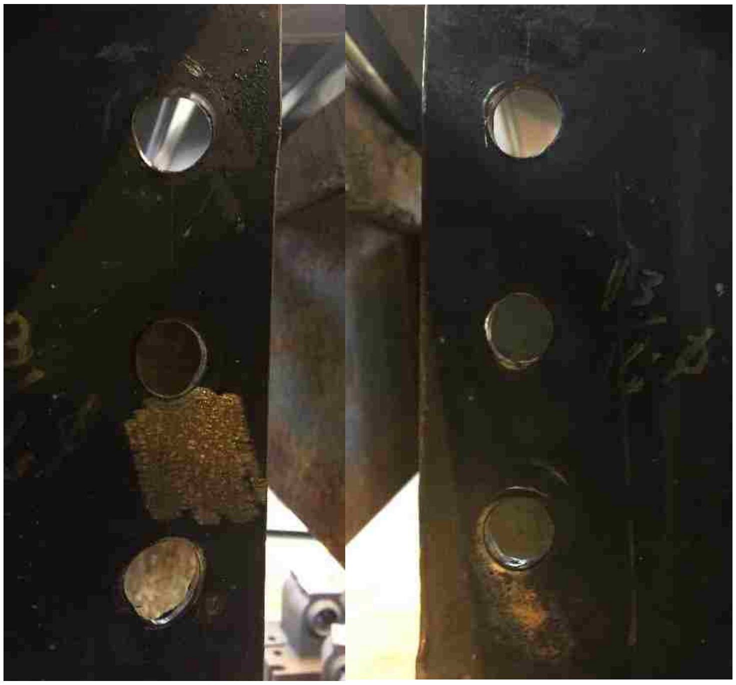

Figure 76 – Test 2 Beam End Connection Holes

Six thermocouples were used to measure the ambient temperature in the furnace. One of these thermocouples failed during the test, and the other five are shown in Figure 77 along with the standard E119 curve and average furnace temperature.

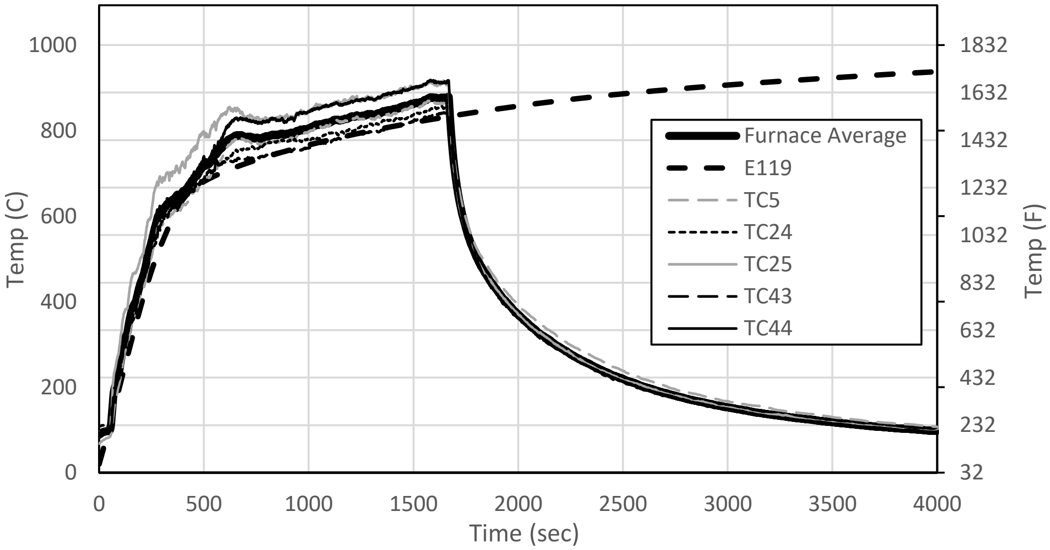

Figure 77 – Test 2 Ambient Furnace Temperature

المنارة للاستشارات
www.manaraa.com

Figure 77 shows that the furnace temperature average is very similar to the E119 standard curve, but slightly higher. According to the E119 standard (ASTM, 2014), the area below the E119 standard curve must be within 10% of the area under the test curve for a test of one hour or less. For this test, the two areas are within 8.78%.

The columns were instrumented with six thermocouples to obtain the temperature at various locations near the connections. Figure 78 shows the average column temperature throughout the test. Note that compared to the previous test, the column heated up faster but peaked at a lower temperature due to the length of the test.

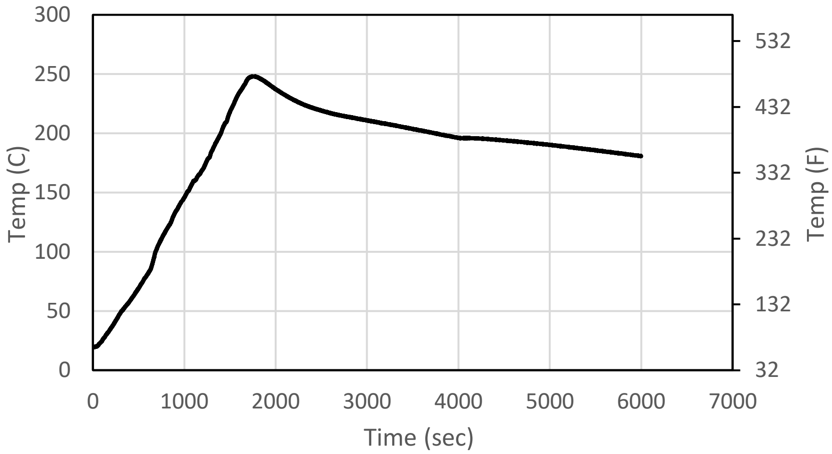

Figure 78 - Test 2 Average Column Temperature

Figure 78 shows that, due to the conductivity of steel, the columns heated up even though they were wrapped with a ceramic fiber blanket. Since the properties of steel change at these temperatures, the length of the columns that were inside the furnace were once again modeled as heated at the same rate shown in Figure 78. The column temperatures were extrapolated in order to analyze the models for a full hour. The column lengths above and

www.manaraa.com

below the furnace were left cold. The models were checked to make sure no local buckling or irregularities occurred at the transition zones.

Once again, the lifespan of the beam is compared with the E119 maximum temperature limit for a beam (1300˚F) or the average temperature limit (1100˚F). In the test, the first condition was met at 16:30, and the second condition was met at 12:00. According to this criteria, the beam would only be qualified for a ten minute rating. However, the test beam was able to structurally survive for 28:15, proving that it is able to provide almost triple the fire resistance compared to the E119 temperature criteria.

5.3.2 Thermal Analysis for Unprotected Beam

The beam temperatures of the top flange, bottom flange, and web were captured with 6 thermocouples on each flange and 3 on the web (15 total on the beam) located at the midspan and quarter points along the length of the beam. The average temperature of each location was taken as the average of the 6 thermocouples. Once again a 2D SAFIR thermal analysis was performed to calculate temperatures of the top flange, bottom flange, and web, as well as a lumped mass calculation in MATLAB. The lumped mass calculation did not include the slab, and assumed the top surface of the top flange was adiabatic. Figure 79 shows the comparison of temperatures from the test, the SAFIR finite element model, and the MATLAB lumped mass calculation.

المنارة للاستشارات
www.manaraa.com

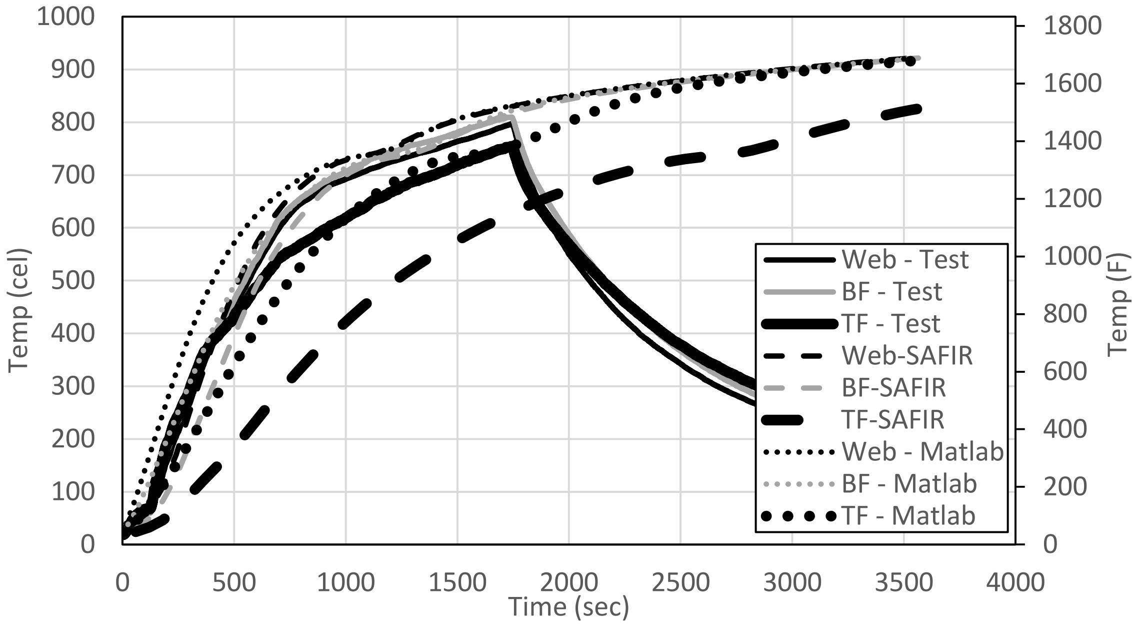

Figure 79 - Test 2 Beam Temperature Analysis Comparison

Figure 79 shows that the temperatures recorded for the top flange in the test does not agree well with the top flange temperatures predicted by SAFIR, and the lumped mass calculation provides a much better estimate. It is important to note that the lumped mass calculation is relatively simple, and takes minimal computing power when compared to the finite element software. The calculation provides a good temperature prediction when working with an unprotected system. Since this study is comparative, and the SAFIR temperatures were used for the protected beam, the SAFIR temperatures will be implemented in the following models. However, in the industry, it is recommended that the lumped mass calculation be considered for temperature predictions on bare steel. The most likely cause for the SAFIR temperatures to be low is that the slab is thermally modeled as perfectly bonded to the top of the flange in the model, and it is able to sink a significant amount of heat from the top flange. In reality, the metal deck is only touching a portion of the top flange, and the other portion is

www.manaraa.com

exposed to the hot air of the furnace. This configuration allows the flange to heat more than the model predicts. Another advantage of the lumped mass calculation is the flexibility that comes with being able to more easily tailor the model to account for the exact amount of heated and unheated steel areas.

The temperatures in the slab were measured with two thermocouples on the bottom of the slab and two thermocouples on the top of the slab. One set was put on the thick section of the slab and one set was put on the thin section of the slab in order to see the change in temperature between these two areas. Figure 80 and Figure 81 show the output from these thermocouples compared with the SAFIR output at similar areas from the “slab with ridges model” observed in Figure 61, for the slab bottom and top, respectively.

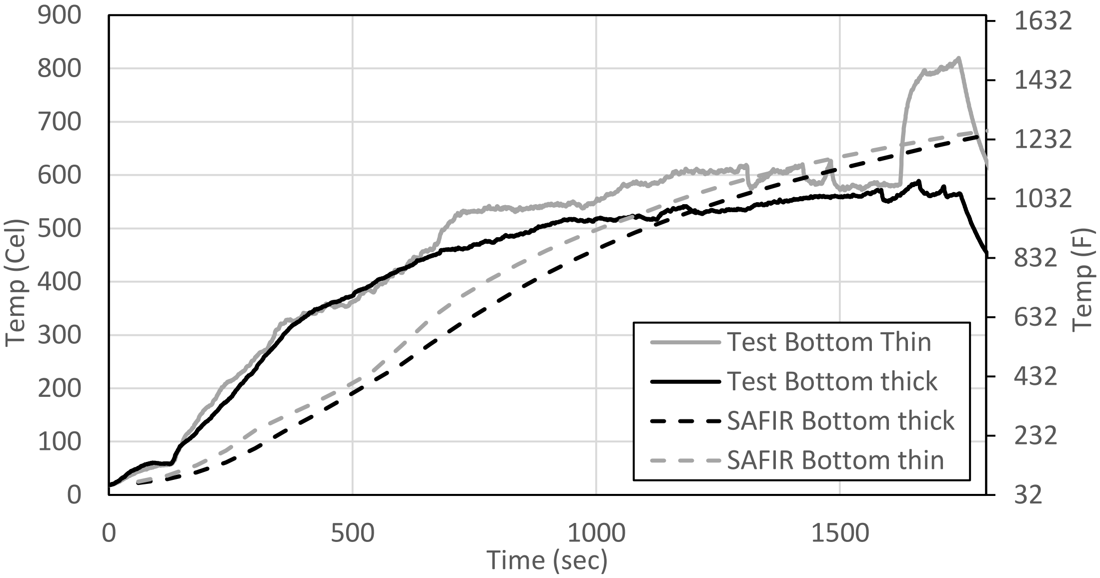

Figure 80 – Test 2 Slab Temperature Comparison: Slab Bottom

www.manaraa.com

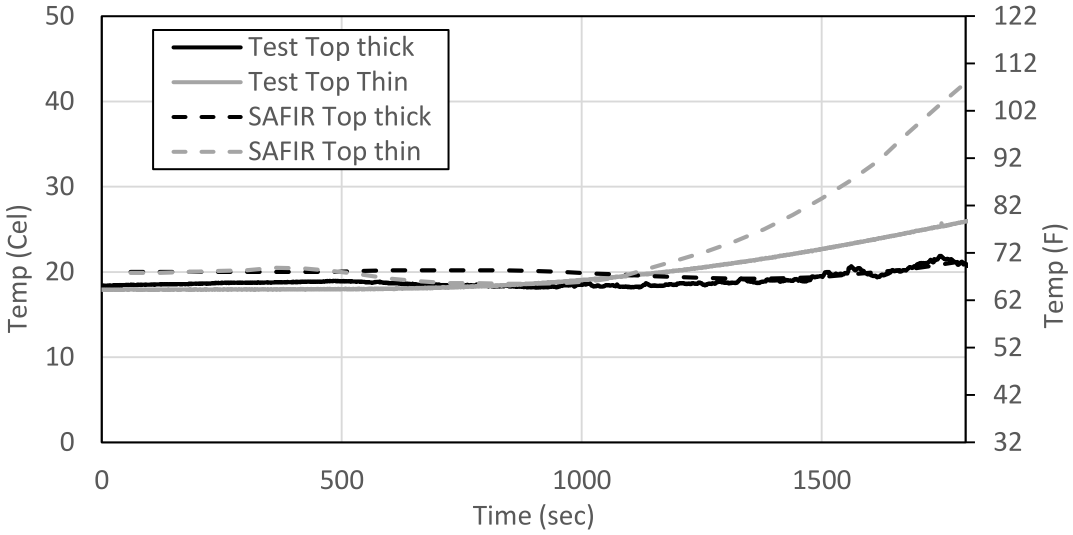

Figure 81 – Test 2 Slab Temperature Comparison: Slab Top

Figure 80 and Figure 81 show that the slab temperatures are fairly accurate between the test and model, with the slab bottom heating up a bit faster in the test and the slab top heating up a bit slower when compared to the SAFIR models. The thermocouples on the slab bottom were placed on the metal decking, which could cause the temperature to be greater than if they were directly on the concrete due to the thermal conductivity differential of the two materials. Note that the test ran for 1,695 seconds, and then the furnace was shut off and the ambient air was allowed to cool. As predicted, in both the slab top and bottom the thin section heats up quicker than the thick section.

5.3.3 Structural Analysis for Unprotected Beam

The same 2D beam, 3D beam, and 3D shell models used for the protected beam test were used for this test. The temperature data was reran for an unprotected W12x26 subject to the E119 standard fire curve. The temperatures of the slab were kept the same as the previous models. The column temperatures from the test thermocouples were used as the new column

المنارة للاستشارات
www.manaraa.com

temperatures for the portion of the column inside of the furnace, and the outside portion was modeled as cold. All other aspects of the model were kept the same.

First, a set of models was analyzed using the beam thermocouple temperatures from the test. The average temperature of each flange was used as a lumped mass temperature, so that there was no gradient over each plate. Figure 82 and Figure 83 show the beam and column deflection, respectively, from these models. This approach was used for the 3D models to evaluate the structural response for this scenario.

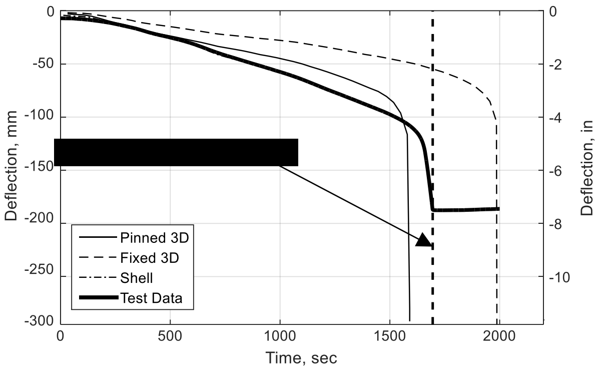

Figure 82 – Test 2 Beam Deflection (Test Temps)

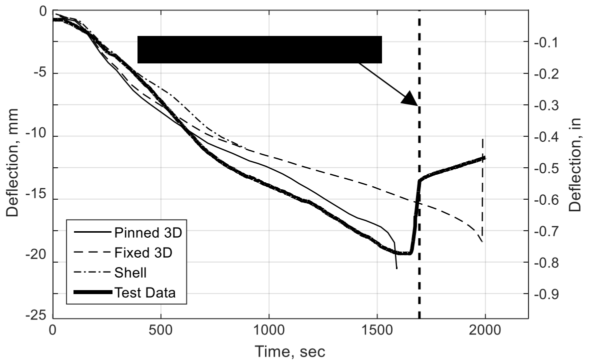

Figure 83 – Test 2 Column Deflection (Test Temps)

The test is shown to behave with more flexibility than the 3D beam models with the test temperatures. The shell model is hard to see, because it is directly overlapping the test data, but the model “fails” near 900 seconds. As seen previously, the shell models are unable to numerically push through local or global buckling in the beam. It was observed in the test beam that a large amount of buckling occurred – it was therefore not surprising that the shell model has numerical difficulty predicting a realistic time of global failure. The deflections of the shell element model compare well with the test results until the numerical instability begins. The pinned and fixed models are able to envelope the failure time of the system within a 6 minute

المنارة للاستشارات
www.manaraa.com

window. Both models predict a very similar end deflection, before the runaway failure begins to occur, and this deflection is very close to what the test beam experienced. It is also important to note that the 3D beam models hit runaway failure similar to the test beam, and are therefore predicting a similar failure mechanism at the end of the test.

The following plastic P-M diagrams show how the fixed and pinned beams behave at the locations that potential plastic hinges could form. Figure 84 shows the fixed beam at the end connection. These diagrams show that the normalized moment increases (due mostly to a rapid decrease in plastic moment) until it hits the P-M envelope. The beam then enters into a slight state of compression once the beam is beginning to fail. This time correlates with when the shell model “fails”, further suggesting that this is when the plastic hinge began to form in this location.

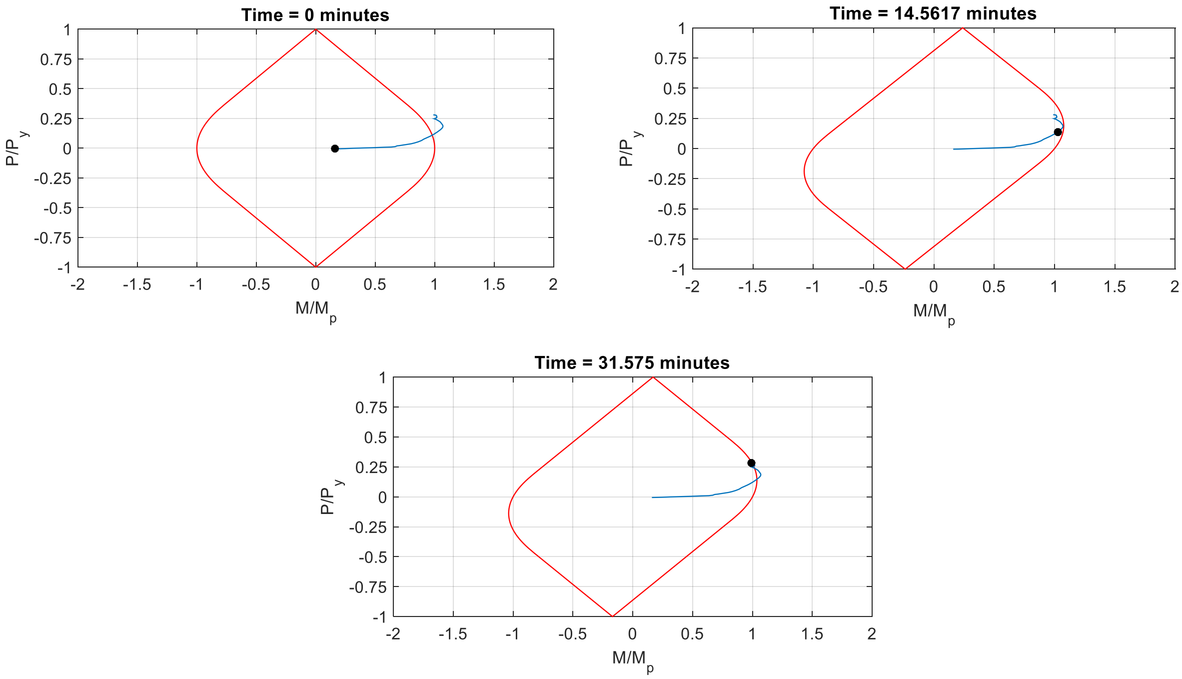

Figure 84 - Test 2 P-M Diagram for Fixed Beam Ends

www.manaraa.com

Figure 85 and Figure 86 show the center of the fixed and pinned beams respectively. The pattern of the behavior is similar for both beams at the center, showing that the end condition has less significance on behavior in the middle of the beam. Both beams enter into a state of compression and decreased moment capacity in the first few minutes of the test, which corresponds to the beam heating up and compressing into the boundaries. The beams then begin to transition to a tensile state as the center of the beam deflects and the moment begins to decrease. The beams fail at a similar location, corresponding to a slight normalized moment and high level of tension, near or on the P-M envelope.

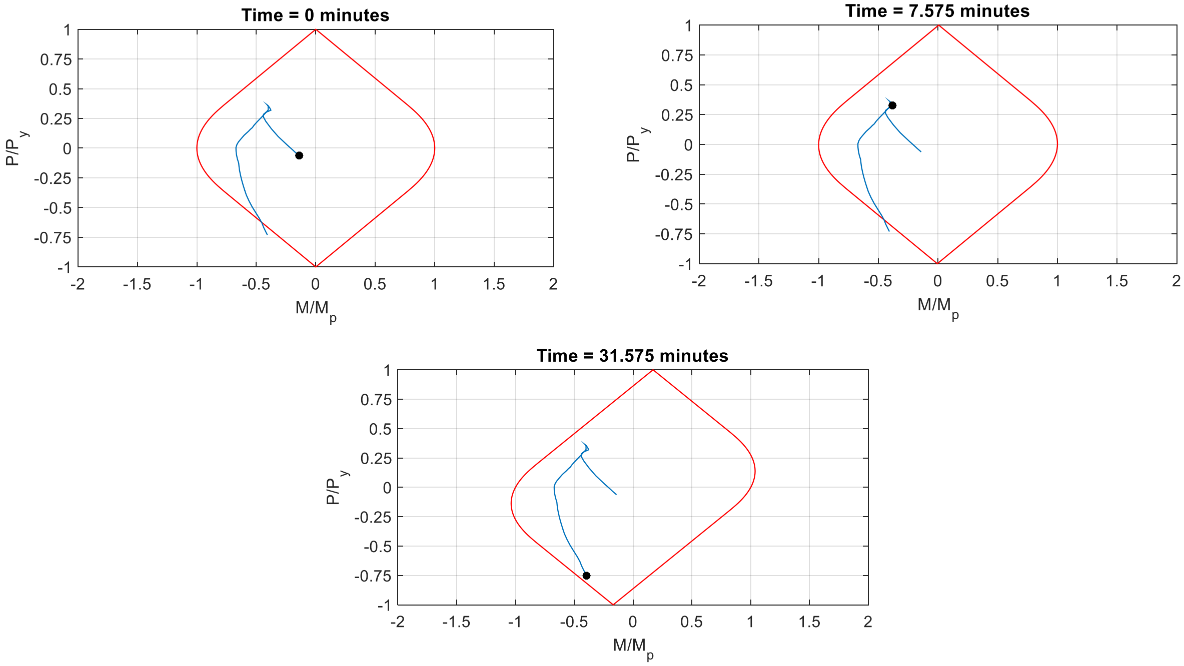

Figure 85 - Test 2 P-M Diagram for Fixed Beam Center

www.manaraa.com

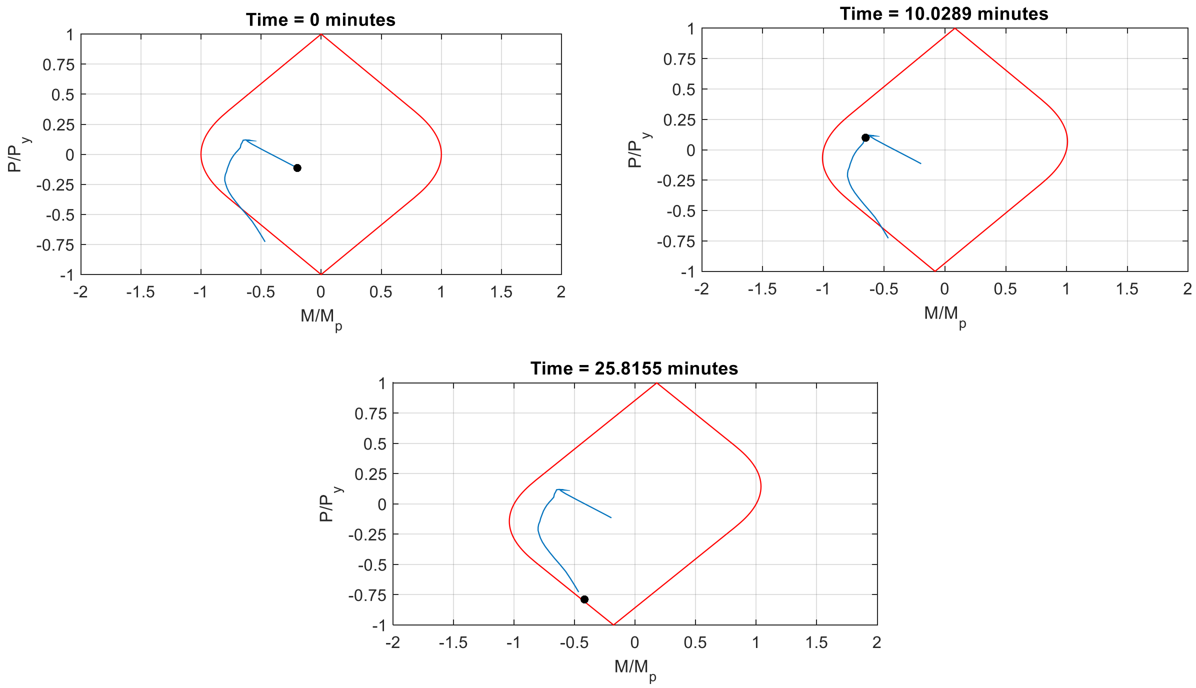

Figure 86 - Test 2 P-M Diagram for Pinned Beam Center

The next set of models were made similarly to the last, but used the SAFIR predicted temperatures for the beam temperature instead of the test temperatures as lumped masses. The advantages of this method are that each plate can have a temperature gradient and the data is no longer based on the test (i.e. representing a "blind calculation" when the beam is analyzed without information from experimental data). Figure 87 and Figure 88 show the deflection of the beam and column respectively for the aforementioned models. For this scenario, the 2D beam models were included.

www.manaraa.com

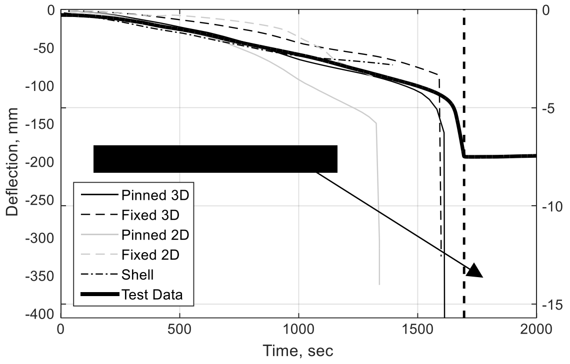

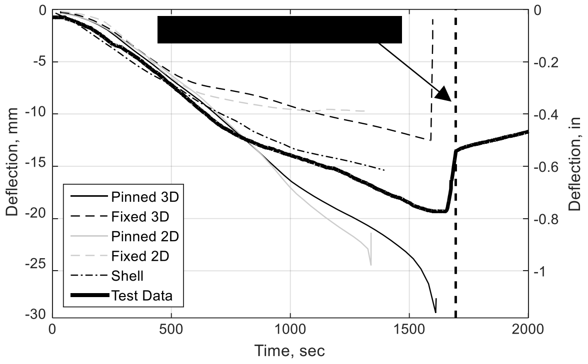

Figure 87 – Test 2 Beam Deflection (SAFIR Temps) Figure 88 – Test 2 Column Deflection (SAFIR Temps)

The inclusion of the SAFIR temperature allows the models to be more flexible than before, which provides a better prediction of the test data. The 3D beam models envelope the test data closely and predict failure just minutes before the test beam failed. These models once again predict runaway failure, and bound the maximum deflection that the beam experiences. The 3D shell model behaves similarly to the previous test, but is able to last substantially longer, to about 1400 seconds. The shell model once again matches the deflection of the beam and column very closely, but is unable to predict the correct failure time due to the numerical instability from internal stresses and local buckling. Figure 89 shows the area where the shell model experiences numerical failure.

www.manaraa.com

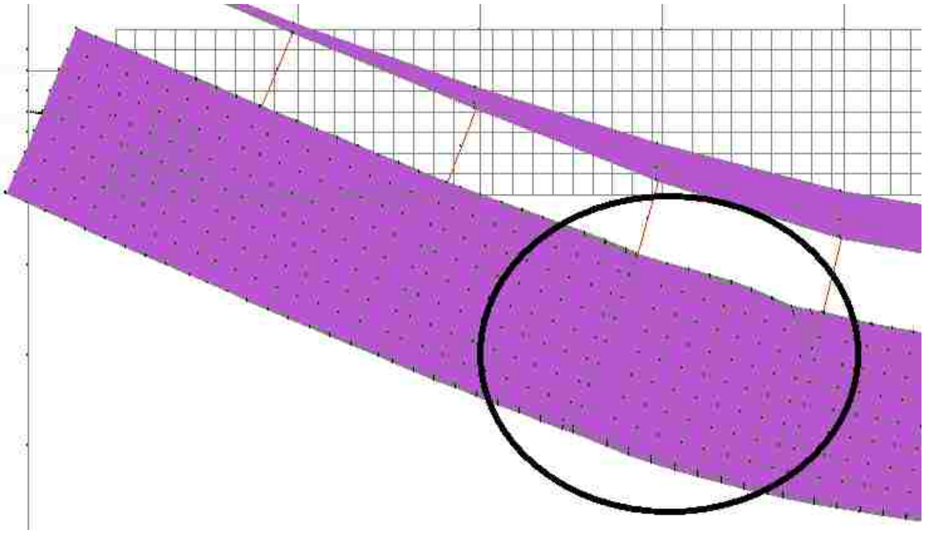

Figure 89 – Location of Failure in Test 2 Shell Model (displacement x10)

The shell model is failing due to internal von-mises stresses becoming too large. This occurs in the beam near the final transition from the cooler connection zone to the hotter main span, similar to where a plastic hinge formed during the test.

The 2D models provide a better prediction than they have for previous scenarios but are still far less accurate than the 3D models. The failure time predictions for these models fall short of the real failure time and predict a similar outcome as the shell model. The 2D models also create a larger deflection variation between boundary conditions, further suggesting that they are less suitable for this application. As seen in the parametric study when realistic boundary conditions are encountered, the 3D models may be preferable for analysis of a composite floor system.

www.manaraa.com

5.4 Conclusions

Two beams were tested in the Lehigh University ATLSS furnace, one of which was protected with SFRM and the other was left as bare steel. Descriptions of the test setup and experimental outcomes have been discussed. The protected beam was given a 2 hour fire rating in accordance with a UL D902 assembly and was able to resist the ASTM E119 fire curve for 2:18:45 before runaway failure was reached. The beam reached the temperature limits from the E119 standard at 1:28:00, when the average temperature of the beam exceeded 1100˚F. The unprotected beam was able to resist the E119 fire for 28:15 before failure was reached. This failure was justified by an extreme increase in the rate of the beam deflection, considered to be runaway failure. The beam failed temperature criteria from the E119 standard at 12:00, where once again the average beam temperature exceeded 1100˚F. A summary of the beam failures based on the E119 rating, the test, and the SAFIR models is provided in Table 4. Note that the structural category in the SAFIR models is left blank. This category has been explored in detail with many different models throughout the chapter, and cannot easily be summarized in a single failure time. If a failure time had to be chosen for this category, a good approximation would be to use the average of the failure time between the 3D pinned and 3D fixed models. These models have been proven to most accurately predict failure times, and often envelope the failure time found from the experiments.

Table 4 – Failure Time Comparison

		Test			**SAFIR**		
	E119 Rating	Avg (1100 °F)	Max (1300 °F)	Structure	Avg (1100 °F)	Max (1300 °F)	Structure
Protected	120	88	100.75	138.75	93.7	86	N/A
Unprotected	N/A	12	16.5	28.25	16	14.5	N/A

www.manaraa.com

The temperatures during both tests were recorded using high temperature compatible thermocouples. The temperatures of the beam, slabs, columns, and furnace compartment were recorded and compared with theoretical models. The temperatures of the beam were compared with SAFIR thermal models and MATLAB lumped mass calculations. It was shown that the lumped mass calculations provide more flexibility to create better predictions of top flange temperatures with varying exposure. Calculating the temperature of the bare steel beam is much simpler than the protected beam, and more research needs to be conducted in order to obtain better temperature predictions for SFRM protected beams. Temperature comparisons were performed for the slab and the ambient air in the furnace, and good agreement between test results and calculations were obtained. The temperature of the column was monitored and input into the structural models for improved realism.

Finite element models were created with SAFIR at various levels of complexity to show the capability of different model types at predicting failure times and element behavior. 2D beam models were created and shown to not fully capture the complexity of a composite system. 3D beam models correlated very well with the data, and enveloped the beam and column deflection between the perfectly pinned and fixed model boundaries. 3D shell models were created with a higher level of modeling fidelity, and were able to predict the experimental behavior until numerical instability was reached. Numerical non-convergence in the shell models was mostly caused by the onset of local or global buckling. The models were not able to predict a reliable time to failure, but were able to predict locations timing of local buckling.

www.manaraa.com

6.0 Parametric Study

A parametric study was conducted to see how the length of the beam and boundary conditions would affect the outcome and behavior of the composite floor beam at failure. The ATLSS furnace is able to test a maximum beam length of about 11’, which is a short span for an office building. Therefore, the project team subsequently investigated the behavior of the beam at a more realistic span. The four beam lengths chosen to be analyzed were 15’, 20’, 25’, and 30’. These lengths are most commonly seen in office buildings as the secondary framing beams. The boundary conditions were updated to replicate what would be seen in a realistic building, similarly as described in section 4.3. The structural consequences of these updates is reviewed. The following sections will discuss the outcomes of the parametric study using the 2D beam, 3D beam, and 3D shell models in SAFIR 2016.

The beam chosen for this study was a W12x26 with a 3.25” concrete slab on top of a 2” metal deck. The details of the design of this specimen can be found in section 5.1.1. The live load applied to each specimen can be found in Table 5.

Table 5 - Applied Live Load

Length (ft)	**% Moment Capacity**	**M_{app} (k*ft)**	**w_{max} (k/ft)**	**w_{LL} (k/ft)**
15	25	68.5	2.44	2.16
20	25	68.5	1.37	1.10
25	25	68.5	0.88	0.61
30	25	68.5	0.61	0.34

The percent moment capacity was kept constant at 25% for each beam length, similar to the test beams. This means that the beam was loaded to 25% of the beam moment capacity, as

المنارة للاستشارات
www.manaraa.com

described in section 5.1.2. From this and the known dead load, the live load was back calculated for each beam length, and is shown in the last column. The study was done for both the W12x26 unprotected and a protected beam.

The beams were heated with the full E119 standard fire curve in SAFIR. The beam temperatures from the SAFIR thermal analysis are used in all of the models.

6.1 Description of Structural Models

2D beam, 3D beam, and 3D shell models were created in SAFIR 2016 to be used in the study. These models were made with realistic boundary conditions, similar to what would be found in an office building. Specifically, the beam ends were axially restrained, the lateral edges of the slab were fully clamped (i.e. fully restrained to rotation or translation), and the longitudinal edges were restrained for rotation about an axis parallel to this edge as well as transverse translation (in the plane of the slab). The process of creating these models is described in sections 5.2.3 for the structural characteristics, section 4.3 for the boundary conditions, and 5.2 and 5.3 for the thermal characteristics of the protected and unprotected beams, respectively. The beam models were created with two boundary conidtions: perfectly pinned and perfectly fixed. The shell model used a shear tab connection that was constructed in the same way as the previous study. All of the models were originally created at 11’ lengths, which is the length able to be accommodated in the ATLSS furnace. Figure 90 and Figure 91 show how the 11’ models with realistic boundary conditions behave for each model type. The behavior of these models will be used as reference when the length is extended.

www.manaraa.com

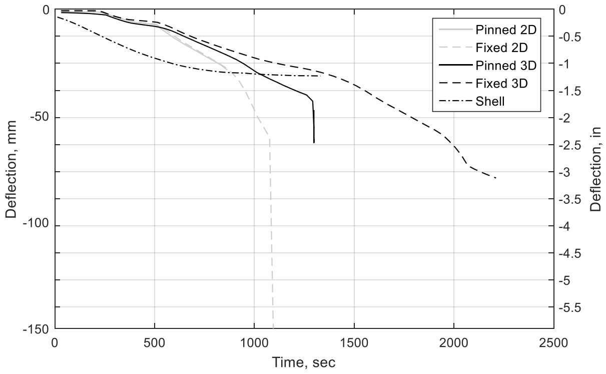

Figure 90 –Realistic Unprotected Beam Deflection

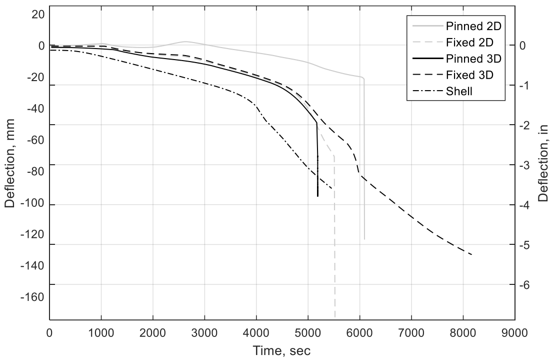

Figure 91 –Realistic Protected Beam Deflection

For both the protected and the unprotected beam, the shell model analysis terminates earlier than the fixed end beam models. In the unprotected case, the beam buckles and cannot resolve the internal forces in the shell model, but the 3D beam model neglects local effects and has more numerical stability, similar to the shell models in the previous study. Since the beams are short, local buckling occurs in the unprotected beam shell models. The 2D beam models are shown to be less effective for both cases. In the unprotected case, the 2D beam fails much earlier than the other models predict. In the protected case, you get upward bowing in the pinned model early in the fire exposure due to the concrete slab heating quicker than the protected steel beam. This is an unrealistic result which was not seen in any of the experimental tests. The fixed and pinned 2D models hit runaway failure, as shown by the steep slope of the deflections at the end of the model.

6.1.1 2D Models at Various Lengths

The 2D pinned and fixed realistic models were updated to each of the four lengths chosen for the study. A comparison of beam deflection from each model can be seen in Figure 92 and Figure 93 for the unprotected and the protected beams, respectively.

www.manaraa.com

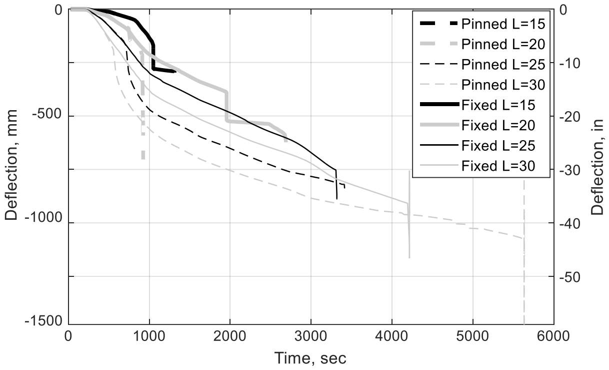

Figure 92 – 2D Beam Deflection -Unprotected

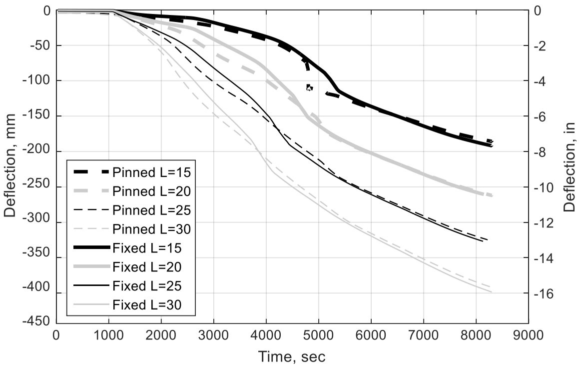

Figure 93 – 2D Beam Deflection -Protected

As stated before, the 2D models are not able to fully characterize the behavior of the composite beam, and therefore should not be relied on for design. In this case, the unprotected 2D models behave realistically, showing a conclusion that could be believed. The unprotected beams show that the longer beams are able to outlast the shorter beams, and the pinned beams deflect quicker than the fixed. The protected beams show that the beam length doesn’t change the time to failure, just the rate of deflection. However, since these models have been shown to be less reliable than 3D models in other analysis cases, any data provided from these models should be weighed carefully for proper application.

6.1.2 3D Models at Various Lengths

The same process was repeated for the 3D models in order to have a pinned and fixed model for each length, for the unprotected and the protected beam. The beam deflection comparisons for the unprotected and protected beams can be seen in Figure 94 and Figure 95 respectively.

المنارة للاستشارات
www.manaraa.com

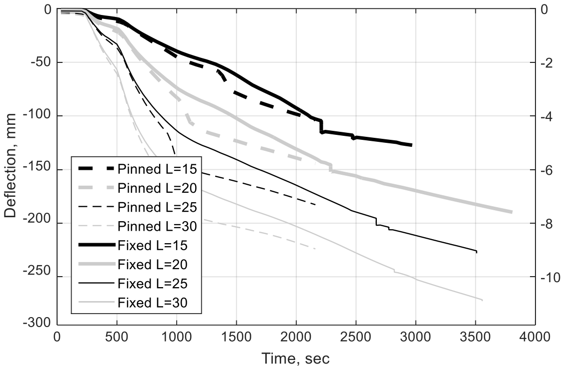

Figure 94 – 3D Beam Deflection -Unprotected

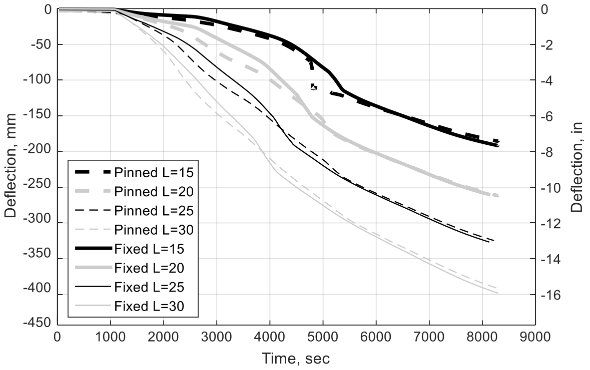

Figure 95 – 3D Beam Deflection -Protected

The 3D beams models are much better at predicting the beam behavior than the 2D models. For both cases, the pinned beam typically deflects at a faster rate than the fixed beam, due to the inherent flexibility in the pinned connection. For the unprotected cases, the pinned beam fails earlier than the fixed beam for all of the lengths. The higher rigidity in the fixed connection allows the fixed beam to outlast the pinned case. For the protected case, the pinned and fixed beams fail at almost the exact same time for all of the lengths. This shows that when the beam is protected the end condition plays a smaller role in the beam behavior. Many of the models have a lurch in the deflection data near an hour and a half after the fire has started. This could be due to the beam “jamming” into the connections, and the force growing until it gets large enough to lurch free, causing a jump in the deflections. Both the unprotected and protected models show that there is little variation in how long the beam will last based on the length of the beam, but the longer beams deflect more than the shorter beams as predicted, at a ratio compatible to the beam length.

المنارة للاستشارات
www.manaraa.com

6.1.3 3D Shell Models at Various Lengths

The 3D shell models have some advantages and disadvantages over the 3D beam models. They are much more complicated models, and this can sometimes lead to stability problems during the analysis. Once the beam starts to buckle, SAFIR can have trouble resolving the internal forces within the member. However, these models are able to provide more insight into the beam's behavior in terms of showing when and where instabilities occur.

Shell models were created at each of the various lengths for the unprotected and protected beams. The number of imperfection wavelengths in the beam flange and web were calculated for each beam length based on its aspect ratio (a/b). The amplitude of the imperfections were kept the same as the 11' model. Table 6 provides the number of waves inserted into the beam shell model for each beam length. Figure 96 and Figure 97 show the beam deflections for unprotected and protected 3D shell models.

Table 6 – Number of Waves in each Beam Flange and Web

Length (ft)	**a/b**	**# of waves**
11	13.04	7
15	17.78	9
20	23.70	12
25	29.63	15
30	35.56	18

المنارة للاستشارات
www.manaraa.com

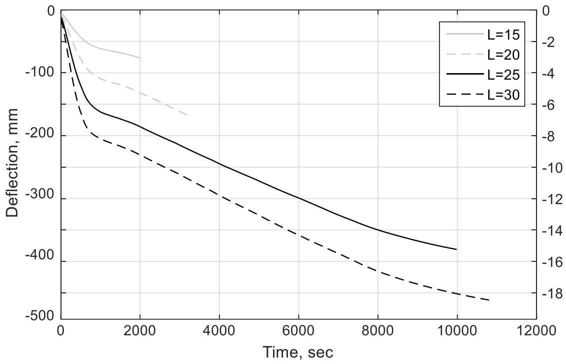

Figure 96 – Shell Beam Deflection -Unprotected

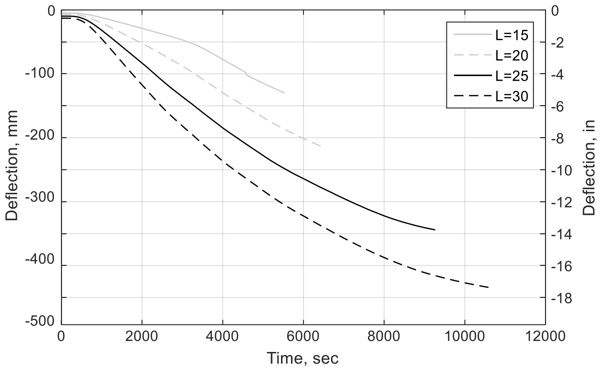

Figure 97 – Shell Beam Deflection -Protected

Unlike the 3D beam models, the shell models show that the longer the beam, the more time it can last before failure. However, the shell models have difficulty with numerical convergence when local buckling emerges, which occurs earlier in the stiffer, shorter beams. Because of this, the outcomes of the failure times are less reliable. The “failure” entails that the model is unable to resolve the internal forces, but the beam may have more strength past the point of local buckling. The longer beams do not locally buckle, and therefore their failure times are more descriptive of global limit states. The protected models, shown in Figure 97, do not experience local buckling, and the shorter beams are able to outlast the unprotected beams. These models show that the longer beams are able to behave similarly with or without fire protection in terms of maximum deflection and time to failure. More research is needed to experimentally examine the impact of realistic continous slab boundary conditions.

6.2 Discussion of 20’-0” Models

The 20’-0” length models will be discussed and compared in further detail. A 20’-0” secondary beam is a realistic length for an office building. Figure 98 and Figure 99 show the

www.manaraa.com

comparison for beam midspan deflection among the 3D pinned, fixed, and shell models for the unprotected and protected cases, respectively.

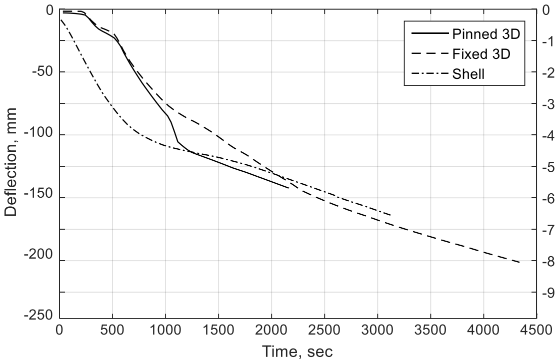

Figure 98 – Beam Deflection: 20’ Unprotected

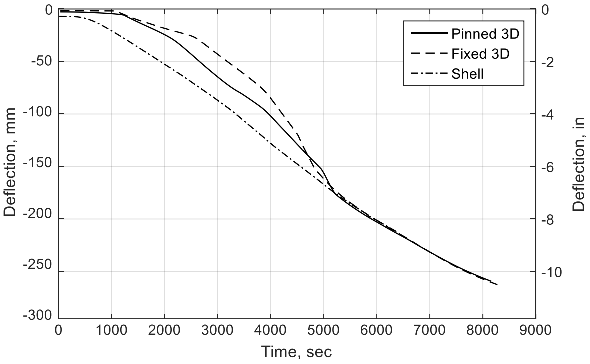

Figure 99 – Beam Deflection: 20’ Protected

Figure 98 shows that the beam deflection trajectory is similarly predicted by all three models, but the models provide a broad range of failure times between about 35 minutes and an hour. The agreement between the three models is even closer for the protected beam shown in Figure 99. The beam deflections start with some variation but converge after ~1.5 hours of heating. The pinned and fixed models predict a very similar failure time of about 2 hours and 15 minutes, and the shell predicts slightly earlier failure at just under 2 hours, when local buckling and numerical instabilities begin to emerge in the model.

According to the E119 standard, the temperature failure criteria of a beam is that once the maximum temperature exceeds 1300°F or that once the average beam temperature exceeds 1100°F. A thermal analysis of the beam cross section was performed using SAFIR for the unprotected and protected beam models. For the unprotected beam case, the maximum temperature limit is exceeded at 17 minutes, and the average limit is exceeded at 15.5 minutes. For the protected beam case, the maximum limit is exceeded at 86 minutes, and the average

www.manaraa.com

limit is exceeded at 95 minutes. Note that these failure times are not dependent on beam length, only the beam cross section.

The structural failure times are determined through the analysis of the SAFIR structural models. Table 7 and Table 8 show the failure times of the 20’-0” 3D beam models, for the unprotected and protected beams respectively. These tables show that the average structural failure time far exceeds the E119 thermal rating. These results also show that the boundary condition plays a larger role in failure time when the beam is unprotected verses protected, and failure times from varying types of models show greater variation when the beam is left unprotected.

Table 7 – Unprotected 20’-0” 3D Beam Structural Failure Times

	Failure Time (min)
Fixed:	63.5
Pinned:	36
Shell:	54
Average:	**51.2**

Table 8 – Protected 20’-0” 3D Beam Structural Failure Times

	Failure Time (min)
Fixed:	135.8
Pinned:	138.3
Shell:	107.3
Average:	**127.1**

The following Figure 100 through Figure 105 present the plastic P-M diagrams for a 20’ fixed and pinned beams at various locations, unprotected and protected respectively.

Figure 100 and Figure 101 show the axial-moment diagrams for the unprotected 20’ fixed beam at the beam ends and the beam center. It can be seen that the beam ends reach the

المنارة للاستشارات
www.manaraa.com

envelope after about 10 minutes, and remain on the envelope for about 7 minutes. As the beam starts to fail, it sheds axial load and then bending moment. The midspan of the beam does not hit the envelope, indicating that this location does not go into a plastic state. The overall trajectory for both locations is similar, but less extreme at the center. Also, the center of the beam finishes the analysis in a state of almost zero axial force, while the beam end retains some of its axial force.

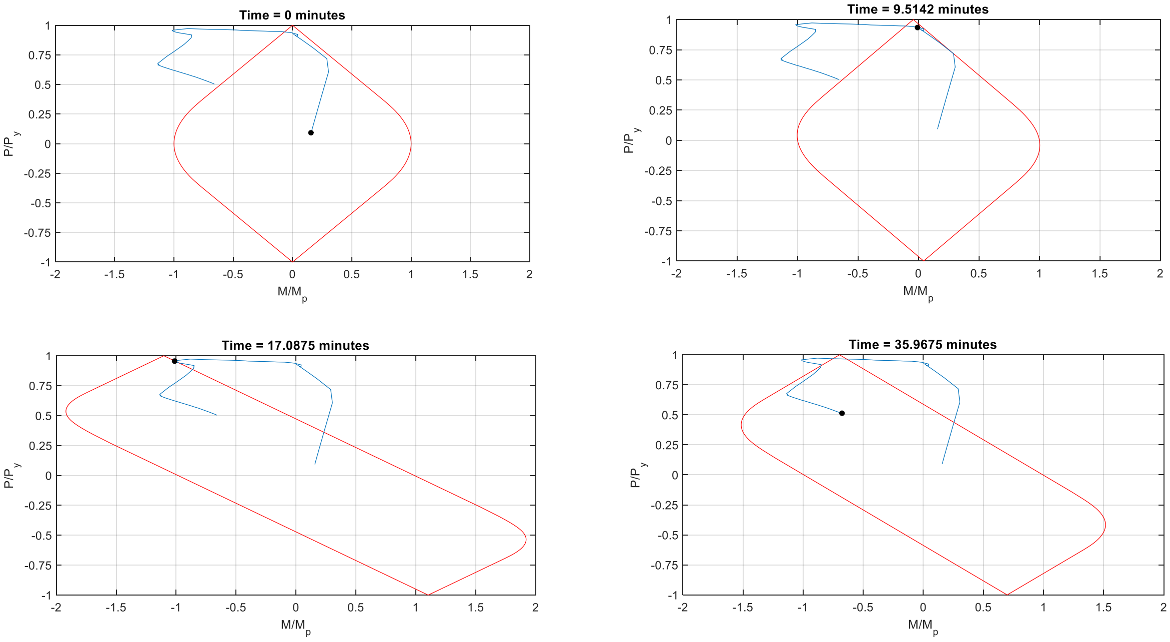

Figure 100 – PM Diagram for Unprotected 20’ Fixed Beam at Ends

www.manaraa.com

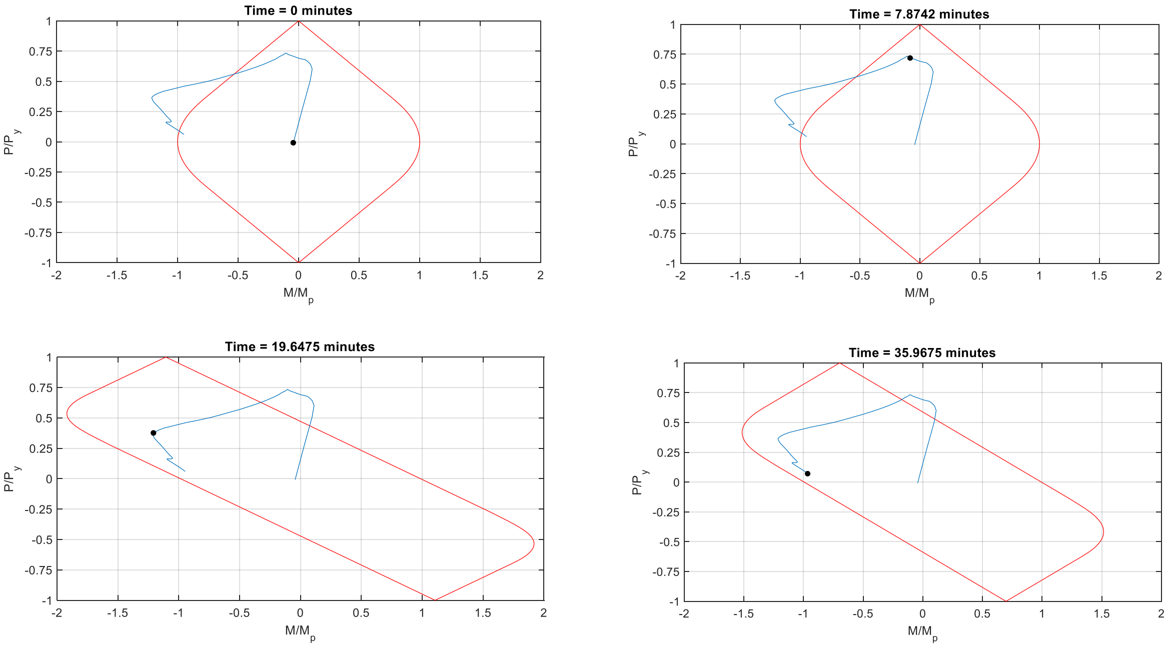

Figure 101 – PM Diagram for Unprotected 20’ Fixed Beam at Midspan

Figure 102 shows the plastic P-M diagrams for the unprotected 20’ pinned beam at the beam center. This beam never fully hits the P-M envelope. It shows a similar pattern as the fixed models, with an immediate increase in axial force followed by an increase in moment. When the model fails, the beam center is holding a small amount of compression as well as a larger negative moment similar to the center of the fixed beam model.

المنارة للاستشارات
www.manaraa.com

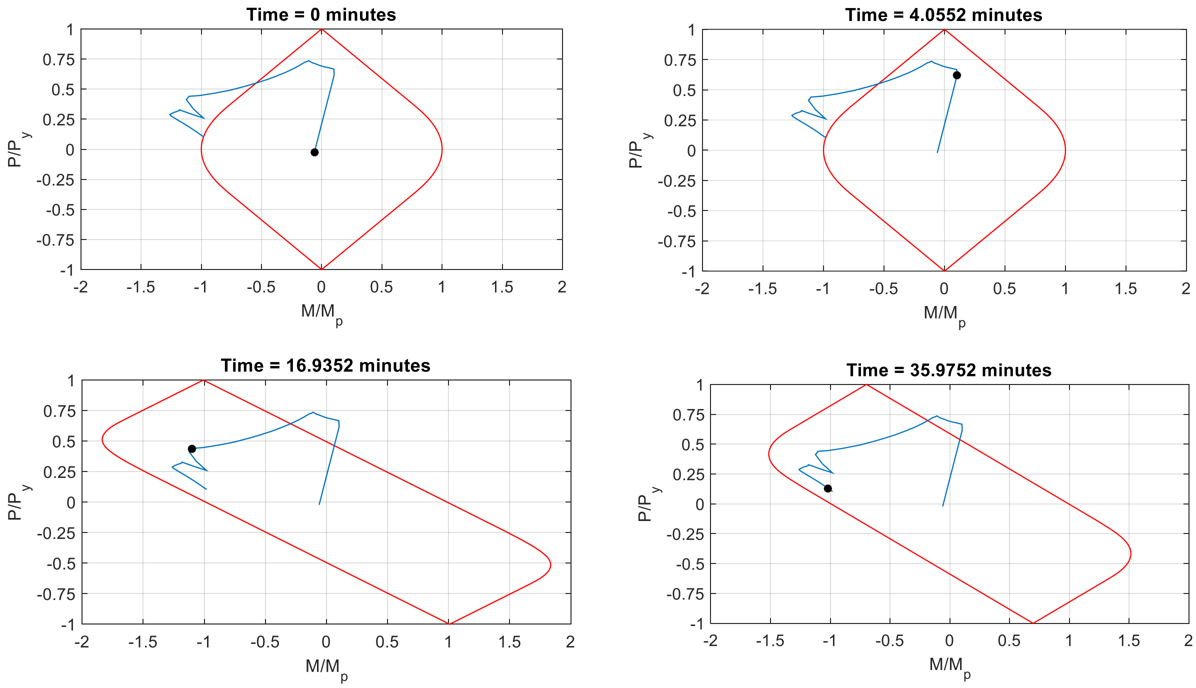

Figure 102 – PM Diagram for Unprotected 20’ Pinned Beam at Midspan

Figure 103 and Figure 104 show the plastic P-M diagrams for the protected 20’ fixed beam at the beam ends and the beam center. Similar to the unprotected beam, the beam end hits the envelope and follows along it, but these occurrences happen later in the test due to the beam heating up slower when protected. The beam center behaves a bit different than the unprotected case, reaching the failure envelope and remaining on it towards the end of the simulation. This location finishes the analysis in an opposite state of moment and axial force than the unprotected case. The beam end is able to reach and ride along the boundary for a longer duration than the unprotected case for a similar reason as mentioned for the beam ends. Since the protected case can withstand the fire for much longer, it allows the beam center to transition to a tensile state and reverse moment. At failure, the center of the beam is still on the envelope, unlike all the other diagrams where the beam leaves the boundary before failure.

www.manaraa.com

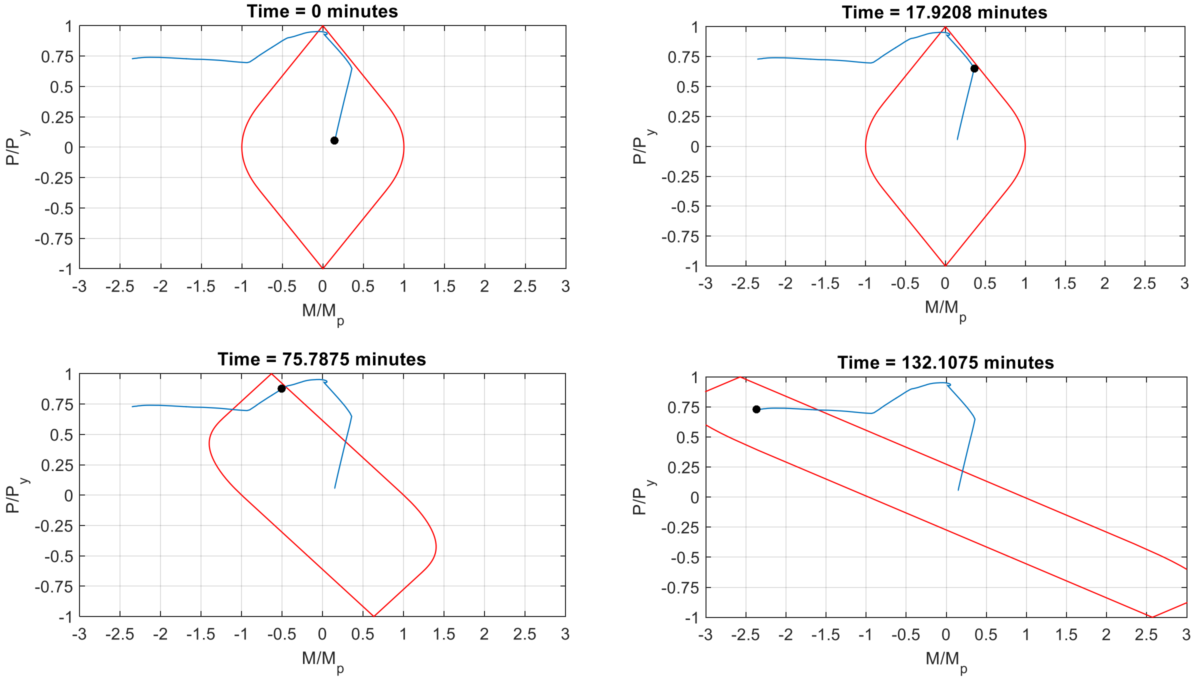

Figure 103 - PM Diagram for Protected 20’ Fixed Beam at End

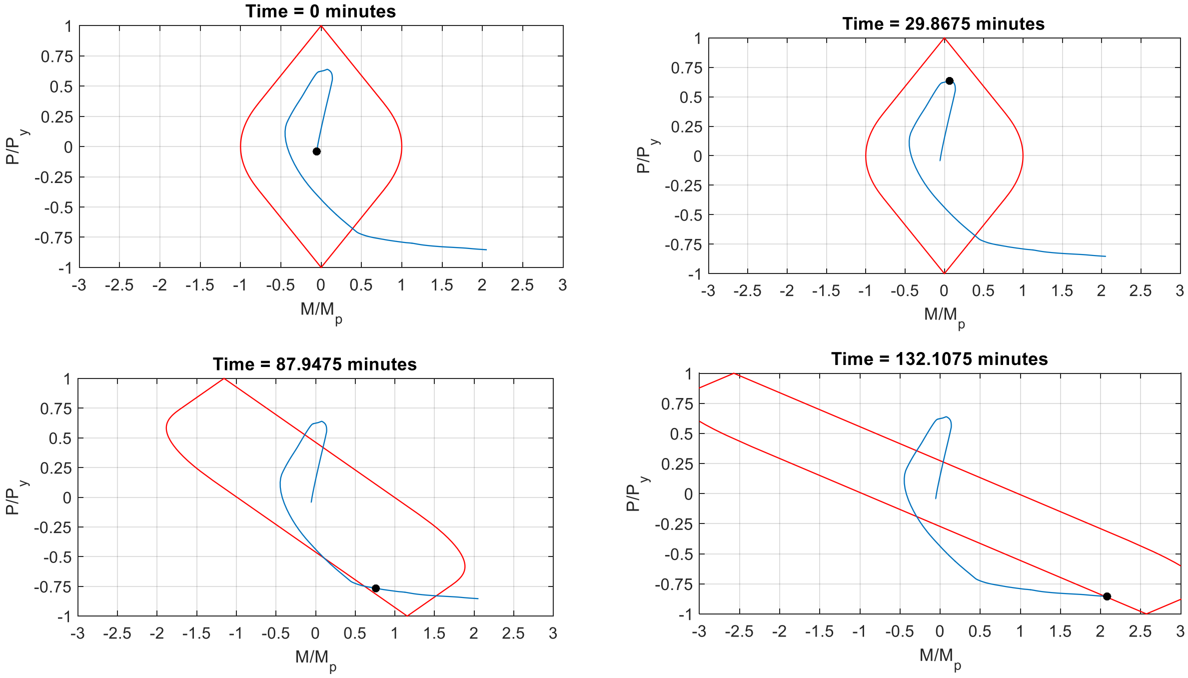

Figure 104 - PM Diagram for Protected 20’ Fixed Beam at Midspan

المنارة للاستشارات
www.manaraa.com

Figure 105 shows the axial-moment diagrams for the protected 20’ pinned beam at the beam center. Similarly to the protected fixed beam at midspan, the beam reaches the failure envelope late in the test (at an hour and a half after the fire started) and just a few minutes before the fixed beam. The beam remains on the failure envelope until the end of the test (at system failure). Once again the beam state is tension and holds a positive moment at midpsan when the test finishes. The overall P-M diagram looks very similar at the beam center for the pinned and fixed beams.

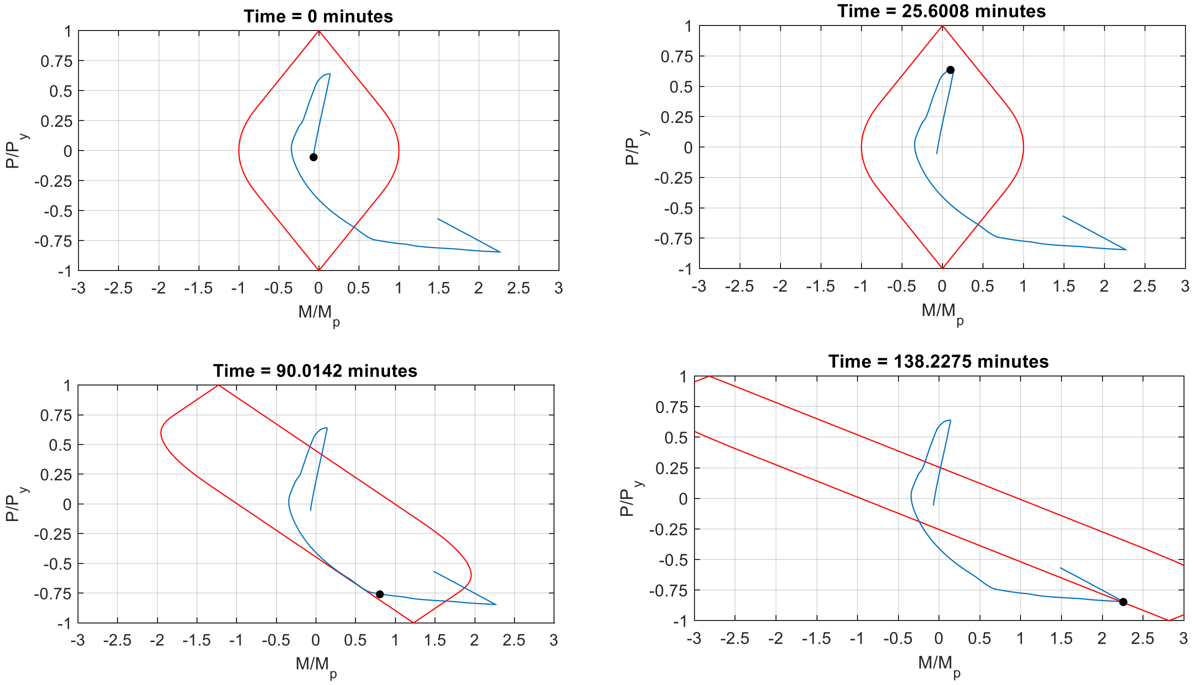

Figure 105 - PM Diagram for Protected 20’ Pinned Beam at Midspan

The following Figure 106 through Figure 111 show the end reactions of the beam and the slab over time for six different models, all at 20’ lengths. Each figure has a caption that shows the protection, model type, and boundary condition for the analyzed beam.

www.manaraa.com

Figure 106 through Figure 108 are all unprotected beams. These figures show that both the beam and the slab immediately go into compression. The slab is always able to swing back into tension before failure, however the beam is only able to get there for the fixed end model. The pinned model shows that the beam gets close to tension, but never fully enters into the catenary state, and the shell model shows that the beam is not able to transition before the beam locally buckles and hits a numerical failure. If the beam enters into a fully tensile state, this result indicates that catenary behavior has been reached, where it no longer has flexural strength, and hangs from the connections. The 3D beam models show that the slab edge experiences its maximum tensile force (indicated by the plateauing of the curve), and the beam is able to transition to tension or get very close.

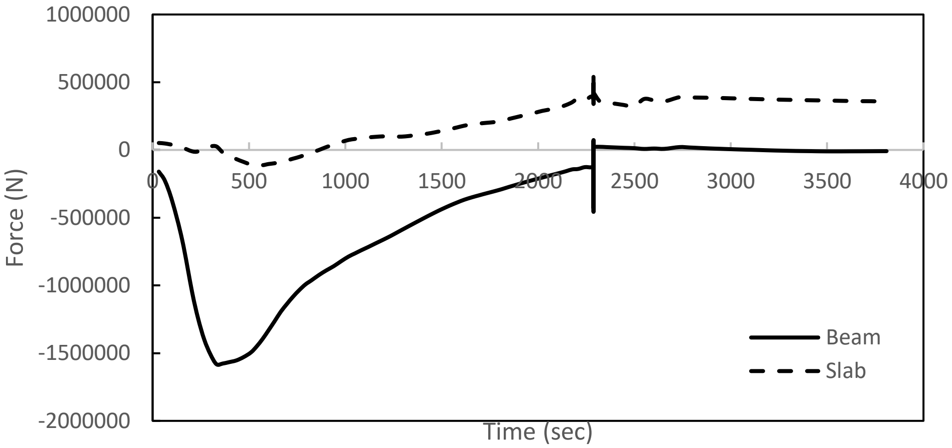

Figure 106 - Unprotected 20’ Fixed Beam End Reactions

www.manaraa.com

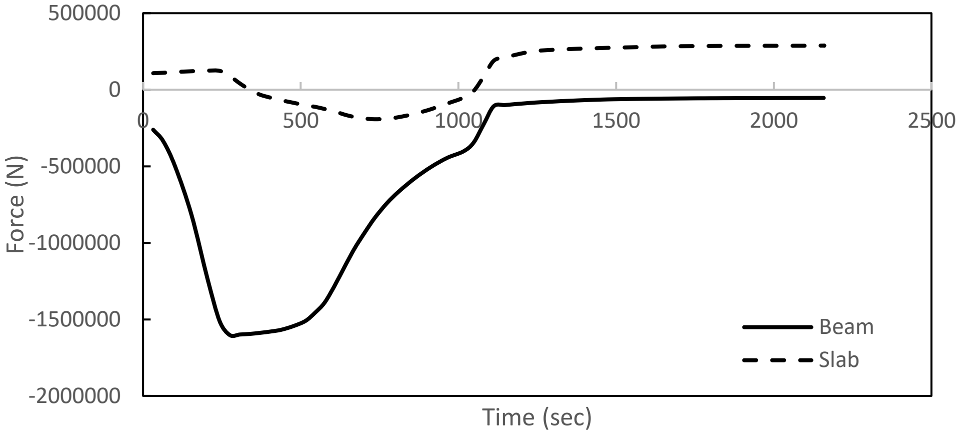

Figure 107 - Unprotected 20’ Pinned Beam End Reactions

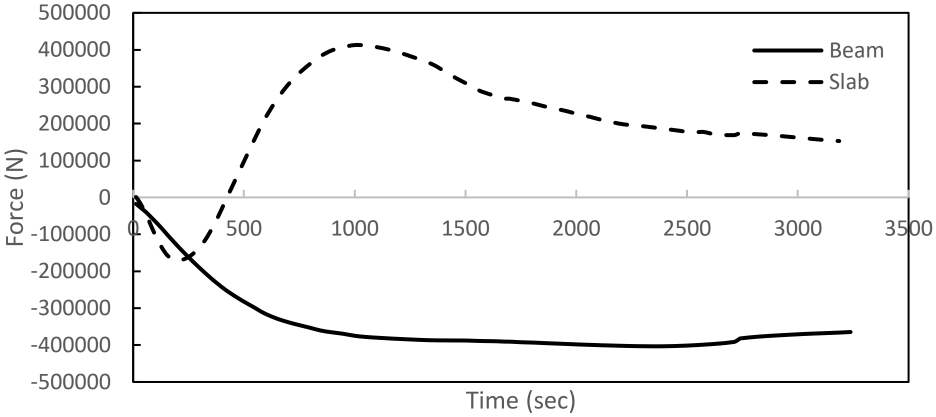

Figure 108 - Unprotected 20’ Shell Beam End Reactions

Figure 109 through Figure 111 are all protected beams. The protected beams are not able to fully transition back into tension. At failure, the beam still has some strength, but the slab has failed. The slab is heating up quicker than the steel, and therefore experiencing higher compression and tensile forces throughout the fire. The slab fails while the beam still holds strength. The beam forces plateau in the fixed and pinned beam models after about 1500 and 1000 seconds of loading, respectively. During this time, the beam is traveling along the yield line, signifying that it has reached a plastic state. Once again, the pinned and fixed behavior are

www.manaraa.com

very similar for the protected beams, shown in Figure 109 and Figure 110, but the pinned beam is able to slightly outlast the fixed. The slab on the fixed and pinned beams is able to fully transition back into tension but is able to hit the tensile strength boundary of the rebar only in the fixed model.

The shell model shows different behavior than the 3D beams. The slab hits a similar compressive force in both models, but is not able to reverse back into tension for the shell model. The beam has less drastic tensile forces in the shell model, which may be due to how the model is set up. As explained previously, a shear tab with three bolts is modeled as the connection. In order to get the axial force in the shell, the forces in the three bolts were summed. This is a bit different than the 3D beam models, where the full edge of the beam is modeled in one node and therefore the full beam end is captured in the axial force data.

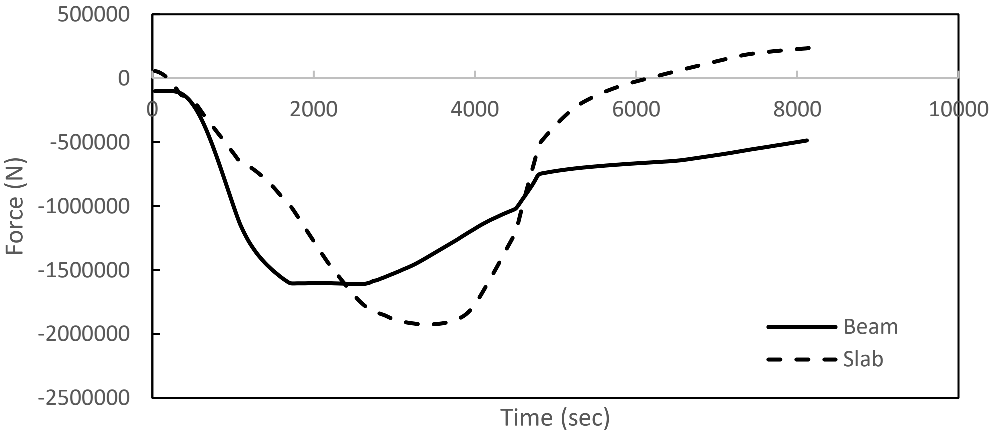

Figure 109 - Protected 20’ Fixed Beam End Reactions

www.manaraa.com

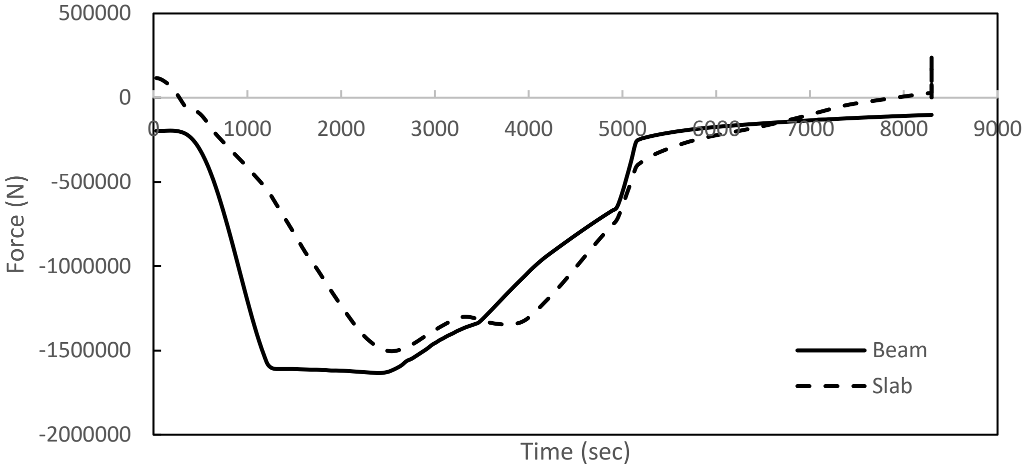

Figure 110 - Protected 20’ Pinned Beam End Reactions

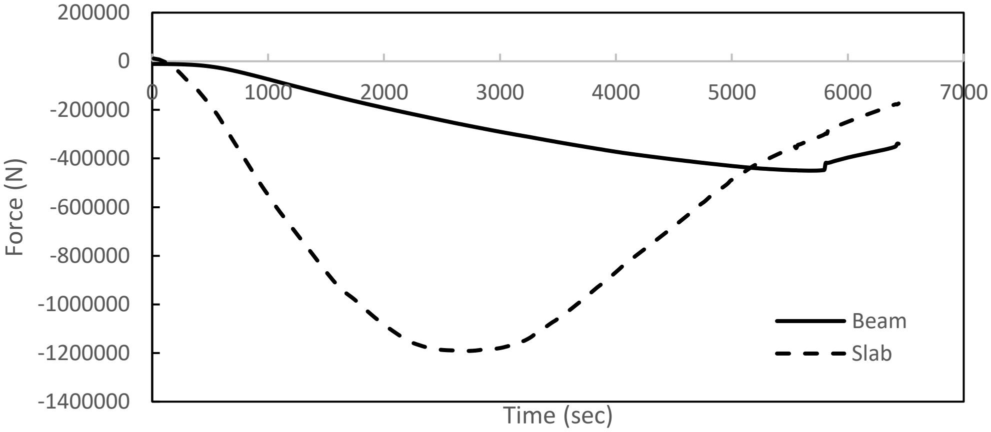

Figure 111 - Protected 20’ Shell Beam End Reactions

6.3 Discussion of 30’-0” Models

The same process was repeated for 30’-0” beam lengths. Comparison of the transverse midspan beam deflection of the three models is shown in Figure 112 and Figure 113 for the unprotected and protected cases, respectively.

المنارة للاستشارات
www.manaraa.com

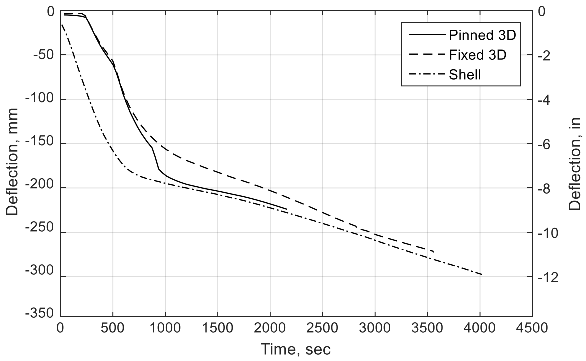

Figure 112 – Beam Deflection: 30’ Unprotected

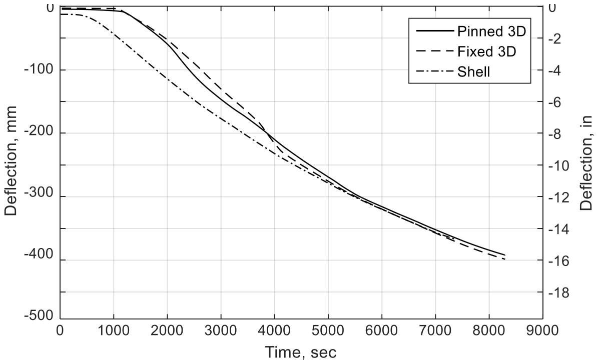

Figure 113 – Beam Deflection: 30’ Protected

Once again, the predictions of deflection and failure time agree better among the different models for the protected beam than the unprotected beam. This further suggests that the end condition has less effect on the beam when protected. The unprotected beam has a very large spread in the estimate of failure time, where the pinned model fails substantially earlier than the fixed or shell models. The protected beam has better convergence, with the failure times of the pinned and fixed being the same, and the shell model failing slightly earlier. Local buckling occurs in the shell models, but not as quickly when the beam lengths are extended. Since the instabilities occurs later, the shell model provides better predictions of failure time for these models. Previously, the shell models predicted early failure for the 11’-0” models. However, once the length of the model is extended, local buckling and instabilities are less pronounced due to lower axial stiffness, and the shell model provides improved numerical performance. Engineering judgement is necessary to determine whether the shell model can be relied upon for failure time prediction, but the trajectory of deflection compares well to the beam element models in all cases.

www.manaraa.com

The structural failure times from SAFIR are compared to the E119 thermal failure criteria previously described. This criteria is not based on beam length, only cross section, so it is the same for all the model lengths. The unprotected beam fails the thermal criteria at 15.5 minutes, and the protected beam fails the thermal criteria at 86 minutes. Table 9 and Table 10 show the structural failure times of the 30’-0” beam for each model, for the unprotected and protected beams respectively. The results once again show better convergence for the protected models than the unprotected models. All of the models predict failure times that are far greater than the E119 thermal criteria predictions. The performance based methods allow the true beam behavior to be captured and provide realistic failure times without the over-conservative tendencies of the prescriptive design methods.

Table 9– Unprotected 30’-0” 3D Beam Structural Failure Times

	Failure Time (min)
Fixed:	59.3
Pinned:	36.0
Shell:	67.0
Average:	**54.1**

Table 10– Protected 30’-0” 3D Beam Structural Failure Times

	Failure Time (min)
Fixed:	138.3
Pinned:	138.3
Shell:	122.5
Average:	**133.0**

The following Figure 114 through Figure 119 show the end reactions of the beam and the slab over time for the six models. Each figure has a caption that shows the protection, model type, and boundary condition for the analyzed beam.

www.manaraa.com

Figure 114 through Figure 116 display the reaction forces in the unprotected beams. The end reactions in the beam and slab differ from the shorter models in a couple ways. For the 30’-0” length, the beam isn’t able to transition back into tension for any of the models, indicating that catenary is not reached. It is commonly thought that composite beams will enter into a state of catenary where the forces are being held through tension instead of bending (Moss at el, 2004). However, the catenary phenomena is not occurring in these simulations.

The slab finishes in a state of tension for all of the models, and the behavior of the slab does not change significantly in each model. The slab is resisting less force for the longer beam models. All of the models show a force couple between the beam and slab reactions that are very similar in magnitude near the end of the simulation, with the beam holding compression and the slab holding tension. The pinned and fixed models also behave very similarly. The fixed model has smoother and more gradual transitions compared to the relatively jagged transitions in the pinned beam.

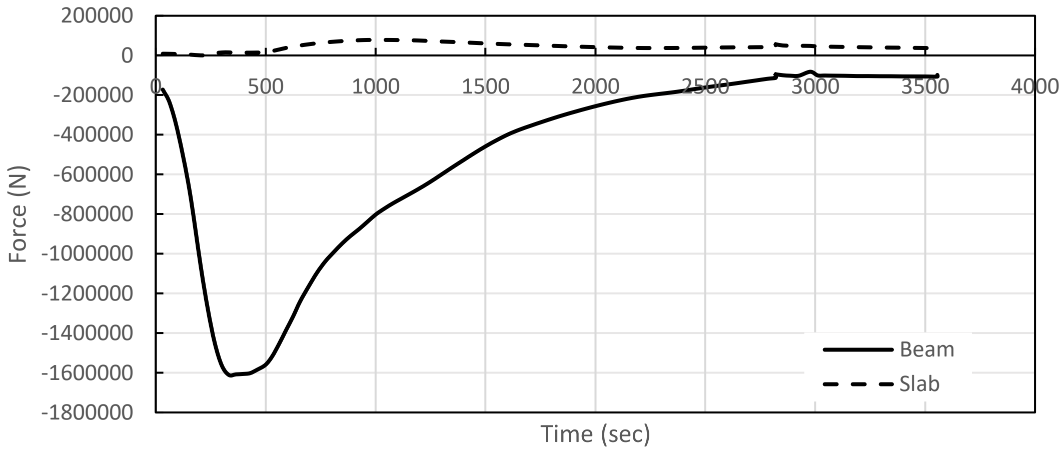

Figure 114 - Unprotected 30’ Fixed Beam End Reactions

المنارة للاستشارات
www.manaraa.com

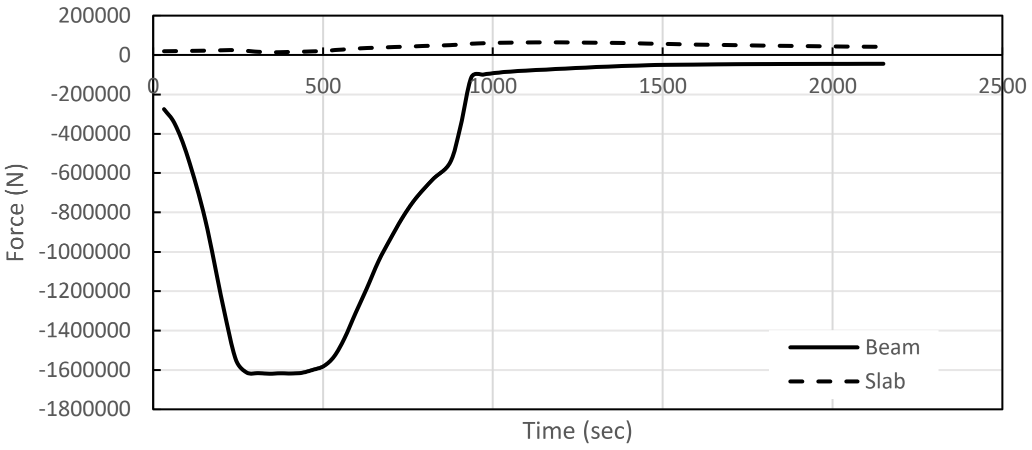

Figure 115 - Unprotected 30’ Pinned Beam End Reactions

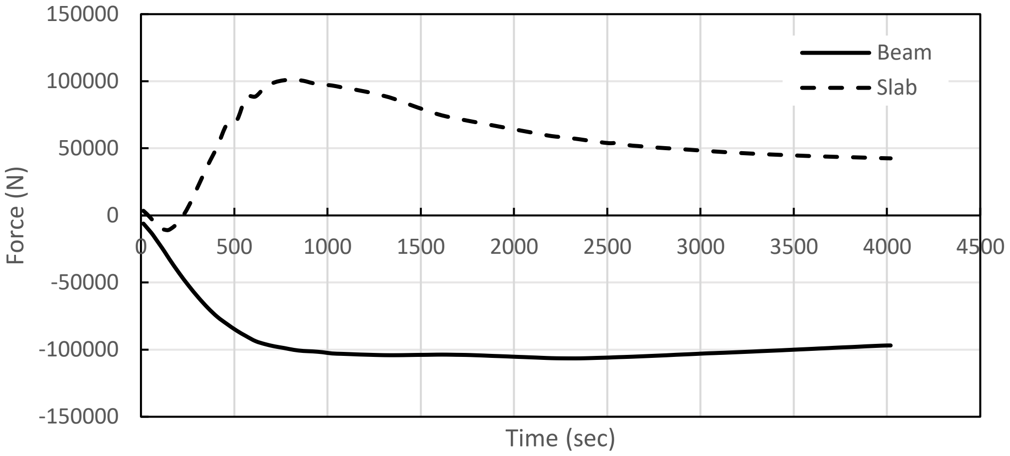

Figure 116 - Unprotected 30’ Shell Beam End Reactions

Figure 117 through Figure 119 show the forces in the protected beams. Once again, none of the protected beams are able to transition back into tension and reach catenary. The slab undergoes a larger transition in the protected beam models because the slab heats up quicker than the protected beam. The slab starts in tension due to the gravity loads, quickly transitions to compression as it begins to heat up, and then swings back into tension as the downward deflection increases. Once again, the pinned and fixed behavior are very similar for the protected beams, and the failure occurs at the same time in both models. The largest

www.manaraa.com

difference can be seen in the beam plateau, where the fixed beam flat-lines at a higher compressive force than the pinned beam.

The shell model exhibits different behavior than the beam models. The beam has less drastic tensile forces in the shell model, similar to the protected 20’-0” model. The beam is not able to go through a full sign reversal of slope, and crashes shortly after this slope change occurs. The model is not able to last quite as long as the beam models due to the local buckling that starts in the beam. The slab behaves very similar in all three models.

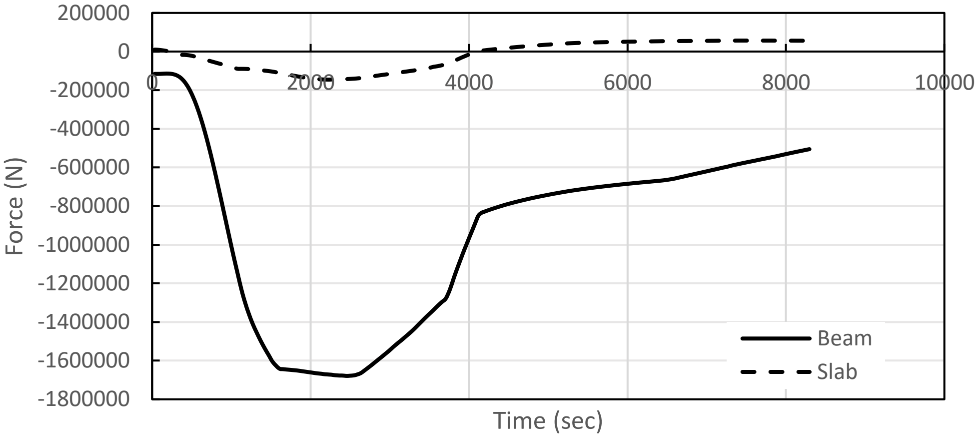

Figure 117 - Protected 30’ Fixed Beam End Reactions

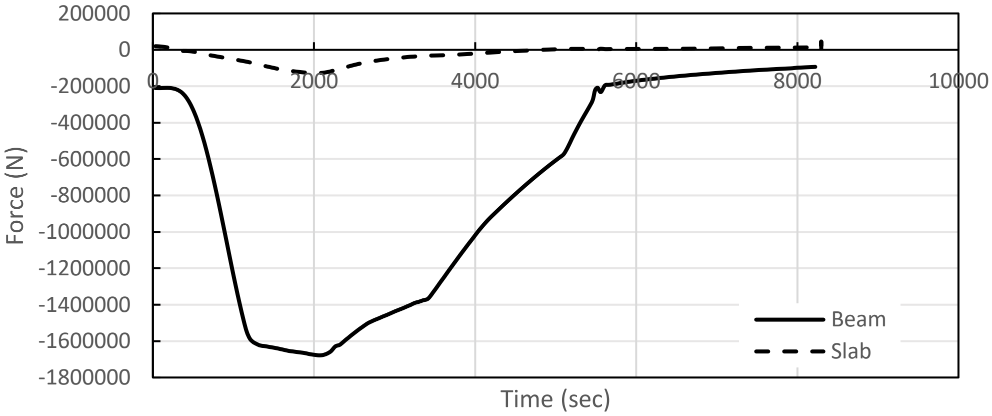

Figure 118 - Protected 30’ Pinned Beam End Reactions

www.manaraa.com

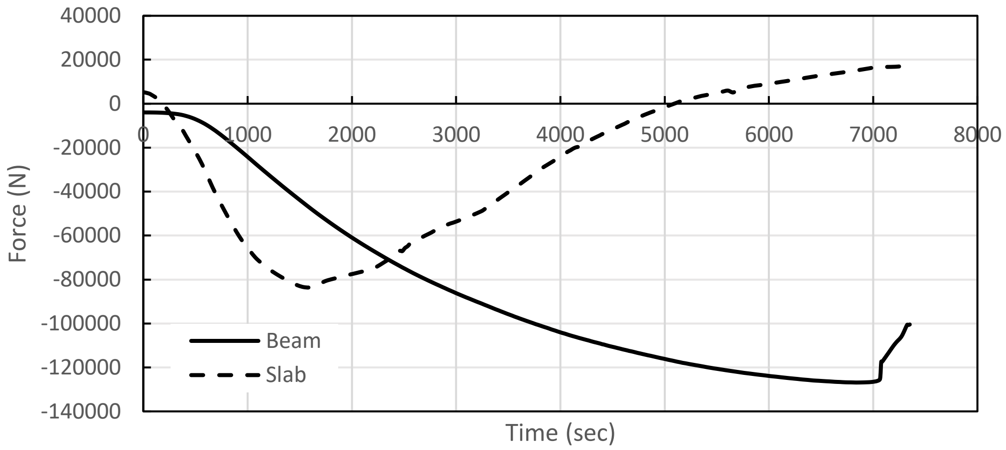

Figure 119 - Protected 30' Shell End Reactions

6.4 Slab Reinforcement Study

A further study was conducted to examine the effect of the reinforcement in the slab on the fire resistance of the composite beam. This study utilized the 20'-0" unprotected 3D beam models previously discussed, and the size of the rebar in the slab was varied. For all scenarios, the bars were set at 12" on center in both directions. The study was performed by varying the rebar size from no longitudinal reinforcement up to size 8 bars. For the case with no longitudinal reinforcement, size 2 bars were still used in the transverse direction in order to allow the model to converge. For all other cases, the bar sizes were the same in the both directions.

Figure 120 shows the failure times for the fixed and pinned cases based on the size of the rebar in the slab. The general trend is that more slab reinforcement leads to more fire resistance, but there are exceptions to the trend. The fixed beam follows this trend closer than the pinned beam, with a smoother trajectory compared to the large spikes in the pinned beams.

www.manaraa.com

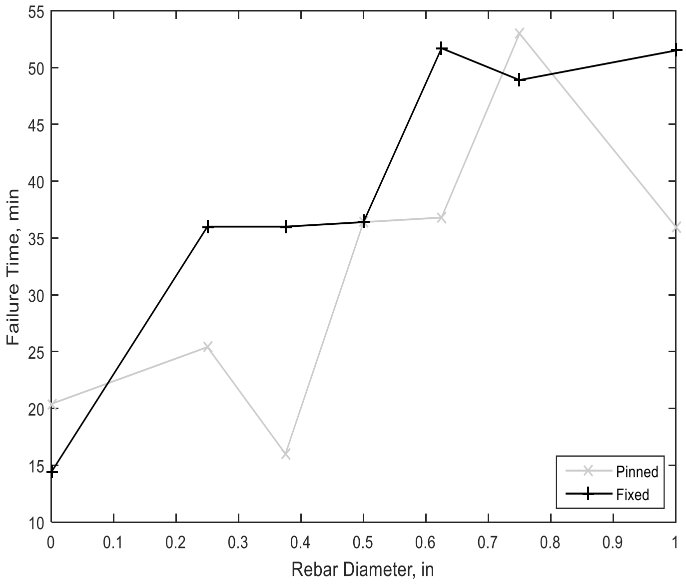

Figure 120 – Rebar Study Failure Times

The load in the edge of the slab verses the size of the rebar can be seen in Figure 121. As expected, the larger rebars are able to withstand a higher tensile reaction load up to the point of system failure. Figure 121 shows that once the rebar diameter increases to 1/2" (size 4 bars), the slab edge load begins to plateau. This is most likely occuring because the rebar gets to the point that it is strong enough to resist failure, and the system is failing due to other mechanisms within the beam or concrete crushing. It is important to note that the added material of increasing the size of the rebar is not providing an adequate increase in strength or system outcome past this point of 1/2" diameter bars. Often times, slabs designed for office buildings will use smaller than size 4 bars, or a smaller mesh size. This study shows that a slight increase in the bar size can provide a worthwhile increase in fire resistance. This idea is supported by Figure 122 , which shows the load in the edge of the slab verses the failure time of the system. There is a group of data points in the lower left quadrant of the graph that symbolize the

www.manaraa.com

smaller bars failing at an earlier time, and there is a group of data points in the upper right quadrant that symbolize the larger bars failing at a later time. There are 6 data points that fall between the 35-40 minute range that emphasize that once the rebar is large enough to not be critical in failure. The added reinforcement beyond the size 4 rebar therfore does very little to provide the system with increased fire resistance. More research needs to be performed on this topic to evaluate the fire resistance with multiple composite floor designs. It is expected that each design would have a different threshold for increased capacity from increased bar size.

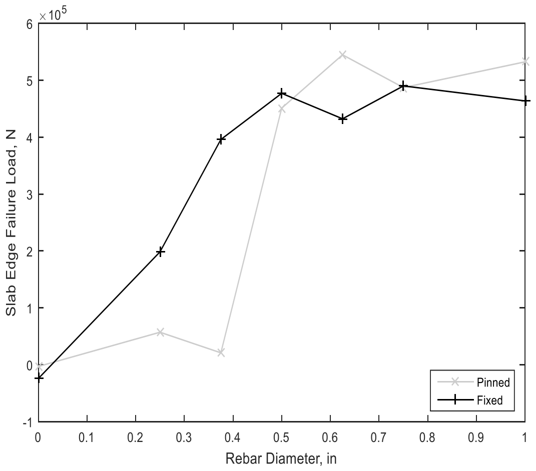

Figure 121 – Rebar Diameter vs. Slab Edge Load

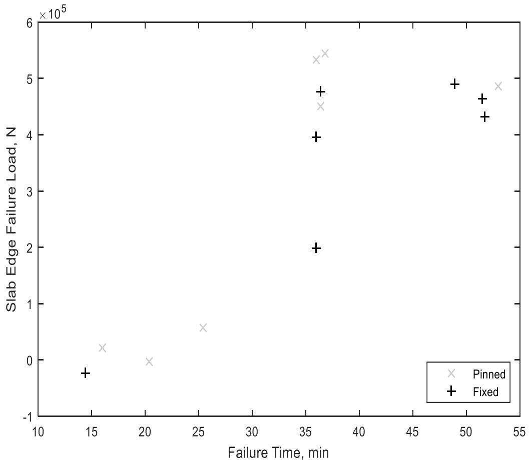

Figure 122 – Failure Time vs. Slab Edge Load

6.5 Conclusions

The parametric study shows that the longer beams deflect more during a standard fire but also are able to retain stability for longer duration. This is an important outcome when considering strength and serviceability requirements of a building after a fire. All of the beam lengths would not be considered serviceable after the fire due to the effects of the large deflections. However, the longer beams provide more stability, allowing people to have more

www.manaraa.com

time to get out of the building before collapse would occur. It is noted that different models provide different sets of outcomes for the length study.

It is commonly assumed that composite beams, similar to the ones studied here, will eventually enter into catenary response during the fire and allow the slab to provide a larger share of the assembly's fire resistance. However, this study shows that is not always the case, with just one of the beams swinging back into a tensile state before instability occurs (the fixed unprotected beam). Changing the size and strength of the slab and rebar has the potential to change this result.

The 2D beam models are not useful for this study. The 3D beam and shell models provide different insight into how the beam behaves. The beam models are able to closely predict failure times for all lengths, because local buckling cannot occur. The shell models are more reliable for longer beams where local buckling doesn't occur as severely due to the limitations of convergence within SAFIR after local buckling. The shell models are useful for monitoring where and when local buckling occurs, but they cannot typically provide much information regarding post-buckling behavior due to the onset of numerical instability. The shell models are also useful in the longer beams where local buckling is not a concern, and can provide further insight into the behavior of the system. Together the 3D beam and shell models provide a well-rounded perspective of fire-induced behavior.

The structural models were shown to outlast the E119 failure criteria for prescriptive design requirements. This shows that the prescriptive design is conservative and leaves room for improvement in terms of saving money, material, and construction time.

www.manaraa.com

A short slab reinforcement study was performed to investigate the relationship between the sizes of the reinforcement and the floor failure times. As expected, the larger reinforcement sizes increased the fire resistance by providing more capacity in tension at the slab edges. For the prototype beam, using size 4 rebar at 12” on center would be the most efficient, and larger bars may only provide minimal improvements for fire. This type of study could be conducive in practice to provide more fire resistance capacity in composite beams via structural mechanisms.

المنارة للاستشارات
www.manaraa.com

7.0 Conclusions and Future Work

Three experiments were performed in the ATLSS furnace at Lehigh University between March 2016 and February 2017. The first experiment used a realistic fire curve with a decay phase to examine the performance of a composite beam in a realistic fire scenario where active fire protection is triggered. This experiment was used to calibrate SAFIR models and show which types of models could be relied on for accurate information. The second and third experiments consisted of two composite beams that were designed to be the same except that one beam was bare steel and the other was coated with SFRM for a two hour fire rating. Both beams were tested with the full E119 curve until failure, the times for which were compared with failure times calculated according to prescriptive design techniques. The objective of these experiments, and future experiments on this fellowship, is to create opportunities for performance based structural-fire design of steel framed floor systems as a complementary alternative to current prescriptive design approaches. In all of the experiments and subsequent computational simulations, the composite beam specimens were able to far exceed the failure time that is prescribed by current design standards via structural performance. A performance based fire design can help save time, material, and money for a project by allowing the designer to tailor the fire protection to meet multiple design objectives.

The comparative beam study was furthered to a parametric study to examine how longer floor beams with realistic boundary conditions would perform when subjected to the standard fire. The models were extended to include 15, 20, 25, and 30 foot lengths for the protected and unprotected beams. The study showed that the longer beams were able to withstand the fire and remain stable for longer durations than the shorter beams. The longer

المنارة للاستشارات
www.manaraa.com

beams also deflected more in terms of total deflection, but deflected at a rate proportional to their length.

The experiments were critical in learning how to accurately model the thermal and structural aspects of structural fire. The steel was modeled thermally using two approaches: a MATLAB lumped mass calculation and a SAFIR finite element analysis. For each experiment the average temperature of the web and each flange was compared with the test data to show accuracy of the methods. The lumped mass calculation proved to be a much simpler way to determine steel temperature, and the equations can be more easily tailored to a variety of fire exposures than the SAFIR calculations. For example, the lumped mass calculation can be calibrated to more closely match the beam's fire exposure present when accounting for the corrugation of the metal decking. Both of these approaches are more accurate when the steel is left unprotected, and further research is needed to improve the accuracy of the thermal models when passive protection is present. The concrete temperatures were obtained using SAFIR, and have less of an effect on the structural model behavior. A thermal model of the corrugated slab was created to include the troughs and ridges of the concrete using GiD Software (CINME, 2016). This approach is more time consuming than using a flat slab, and further research is needed to scale the temperatures in a flat slab to simulate a ribbed slab in order to reduce modeling effort.

The first experiment with the realistic fire curve showed that the 2D structural models should not be relied upon when evaluating the behavior and fire resistance of composite beams. The 3D beam and shell models (both with the slab modeled with shell elements) are much more reliable and are able to provide different levels of information. The 3D beam

www.manaraa.com

models are simple, and not overly time consuming to create. These models are able to predict the failure time and final deflections with great accuracy, but they are not capable of demonstrating the onset of local buckling. The 3D shell models are more complex and cannot realistically be developed for most industry projects due to time constraints. These models prematurely fail due to local and global instability in the beam which creates numerical non-convergence before full system failure. However, these models can be helpful in showing what part of the beam is the most vulnerable to buckling and can indicate what time the instabilities in the beam will occur. Also, these models are shown to be much more reliable for longer beams where local buckling is less likely to occur. Moving forward, more research is needed to better evaluate damage in the 3D beam models so that the shell models will not be required. The beam models can predict final outcomes with very high levels of accuracy, but this is only part of the solution. In order to design a beam to withstand a fire, decisions need to be made on the allowable loss of safety or functionality in a floor system following the fire. Structural evaluations of the damage need to be included to enhance the impact of this study.

Moving forward, there are a few key questions that need to be examined to make performance based structural-fire design more usable and relevant in industry:

- Can the fire resistance of an unprotected composite beam be enhanced by strengthening the slab or the beam prior to the fire?
- Can we use numerical techniques to determine which beams require passive fire protection and which are able to be left unprotected?
- Can we accurately and conservatively predict fire-induced damage in order to improve the resilience of structures that have been exposed to fire?

المنارة للاستشارات
www.manaraa.com

Acknowledgements

The research presented in this thesis is sponsored by the American Institute of Steel Construction (AISC) Milek Fellowship program. Amy Kordosky's involvement with this research project began while on dual appointment as a Gibson Fellow and Teaching Assistant from the Department of Civil and Environmental (CE) Engineering in the P.C. Rossin College of Engineering and Applied Science at Lehigh University. Her second year in the Lehigh CEE MS program was funded through the AISC Milek Fellowship. All opinions, findings, and conclusions expressed in this paper are the views of the authors and do not necessarily represent the policies and views of the AISC or Lehigh University.

المنارة للاستشارات

www.manaraa.com

References

American Institute of Steel Construction. (2010). Specification for Structural Steel Buildings. *ANSI/ASCE Standard 360-10*.

American Society of Civil Engineers (2005). *ASCE/SEA/SFPE 29-05 Standard Calculation Methods for Structural Fire Protection.* Reston, VA.

ASCE. (2010). Minimum Design Loads for Buildings and Other Structures. *ASCE/SEI Standard 7-10*.

ASTM International. (2014). Standard Test Methods for Fire Tests of Building Construction and Meterials. *ASTM Designation E119 – 14.*

Bailey, C. (2004). Membrane action of slab/beam composite floor systems in fire. *Engineering Structures*, 1691-1703.

Banerjee, D. (2012). *A study of Thermal Behavior of a Composite Floor System in Standard Fire Resistance Tests.* National Institute of Standards and Technology Technical Note 1771.

Buchanan, A. (2002). *Structural Design for Fire Safety.* Chichester: John Wiley & Sons Ltd.

Cadorin, J., Pintea, D., Franssen, J. Technical reference of OZone V2. Rapport interne SPEC/2001_01, Department of Structures University of Liège, 2001.

Catella, N. (2008). *The Development of a Modular Furnace for Structural Fire Testing and a Study of Steel Shear Tab Connections' Behavior in Fire.* Bethlehem: Lehigh University.

CEN (2002). EN-1991-1-1:2002 – Eurocode 1: Actions on Structures. *European Committee for Standardization,* Brussels.

Chang, J., Buchanan, A., Moss, P. (2005). Effect of insulation on the fire behaviour of steel floor trusses. *Fire and Materials* 181-194.

CINME (2016). GiD: The Personal pre and post processor. *International Center for Numerical Methods in Engineering,* Barcelona.

Dwaikat, M., Kodur, V., Quiel, S., & Garlock, M. (2011). Experimental behavior of steel beam-columns subjected to fire-induced thermal gradients. *Journal of Constructional Steel Research*, 30-38.

Ellobody, E. (2011). Nonlinear behaviour of unprotected composite slim floor steel beams exposed to different fire conditions. *Thin-Walled Structures*, 762-771.

Franssen, J.-M. (2005). "SAFIR: A thermal/structural program for modeling structures under fire." Eng. J., 42(3), 143–158.

Garlock, M., & Quiel, S. (2007). Mechanics of Wide-flanged Steel Sections that Develop Thermal Gradients due to Fire Exposure. *Steel Structures*, 153-162.

Garlock, M., & Quiel, S. (2008). Plastic Axial Load and Moment Interaction Curves for Fire-Exposed Steel Sections with Thermal Gradients. *Journal of Structural Engineering*, 874-880.

Gewain, R., Iwankiw, N., & Alfawakhiri, F. (2003). Facts for Steel Buildings - Fire. *American Institute of Steel Construction*.

Gewain, R., & Troup, E. (2001). Restrained Fire Resistance Ratings in Structural Steel Buildings. *Engineering Journal Second Quarter,* 78-89.

Ghojel, J., & Wong, M. (2005). Three-sided heating of I-beams in composite construction exposed to fire. *Journal of Constructional Steel Research*, 834-844.

www.manaraa.com

Ioannides, S. & Mehta, S. (1997). Restrained Vs. Unrestrained Fire Ratings: A Practical Approach. *Modern Steel Construction.*

Isolatek International (2016). *CAFCO 300 Spray-Applied Fireproofing.* Technical Data Sheet C-TDS-09/16.

Johann, M., Albano, L., Fitzgerald, R., & Meacham, B. (2006). Performance-Based Structural Fire Safety. *Journal of Performance of Constructed Facilities,* 45-53.

Khorasani, E., Garlock, M., & Gardoni, P. (2014). Fire load: Survey data, recent standards, and probabilistic models for office buildings. *Engineering Structures,* 152-165.

Kodur, V., & Shakya, A. (2013). Effect of temperature on thermal properties of spray applied fire resistive materials. *Fire Safety Journal,* 314-323.

Lamont, S., Lane, B., Flint, G., & Usmani, A. (2006). Behavior of Strutures in Fire and Real Design - A Case Study. *Journal of Fire Protection Engineering*, 5-31.

Moss, P., Buchanan, A., Seputro, J., Wastney, C., & Welsh, R. (2004). Effect of support conditions in the fire behaviour of steel and composite beams. *Fire Mater*, 159-175.

Quiel, S., & Garlock, M. (2010). Closed-Form Prediction of the Thermal and Structural Response of a Perimeter Column in Fire. *The Open Construction and Building Technology Journal*, 64-78.

Quiel, S., & Garlock, M. (2010b). Parameters for Modeling a High-Rise Steel Building Frame Subject to Fire. *Journal of Structural Fire Engineering*, 115-134.

Rini, D., & Lamont, S. (2008). Performance Based Structural Fire Engineering for Modern Building Design*. Structures Congress 2008.*

Seputro, J. (2001). *Effect of Support Conditions on Steel Beams Exposed to Fire.* Christchurch: University of Canterbury.

The University of Edinburgh. (2000). *Behavior of steel framed structures under fire conditions.* Edinburgh: School of Civil and Environmental Engineering.

Underwriters Laboraties Inc. (2016). *Fire Resistance Directory Volume 1.* Northbrook: Underwriters Laboraties Inc.

Usmani, A., Rotter, J., Lamont, S., & Gillie, M. (2001). Fundamental principles of structural behaviour under thermal effects. *Fire Safety Journal,* 721-744.

Vinnakota, S., Foley, C., Vinnakota, M. (1988). Design of Partially or Fully Composite Beams, with Ribbed Metla Deck, Using LRFD Specifications. *Engineering Journal / American Institute of Steel Construction,* 60-78.

Wang, W., Huang, G., Li, G., Engelhardt, M. (2016). Behavior of Steel-Concrete Partially Composite Beams Subject to Fire - Part 1: Experimental Study. *Fire Technology.*

Wastney, C. (2002). *Performance of unprotected steel and composite steel frames exposed to fire.* Christchurch: University of Canterbury.

www.manaraa.com

Appendices

Appendix A – Beam Design Calculations

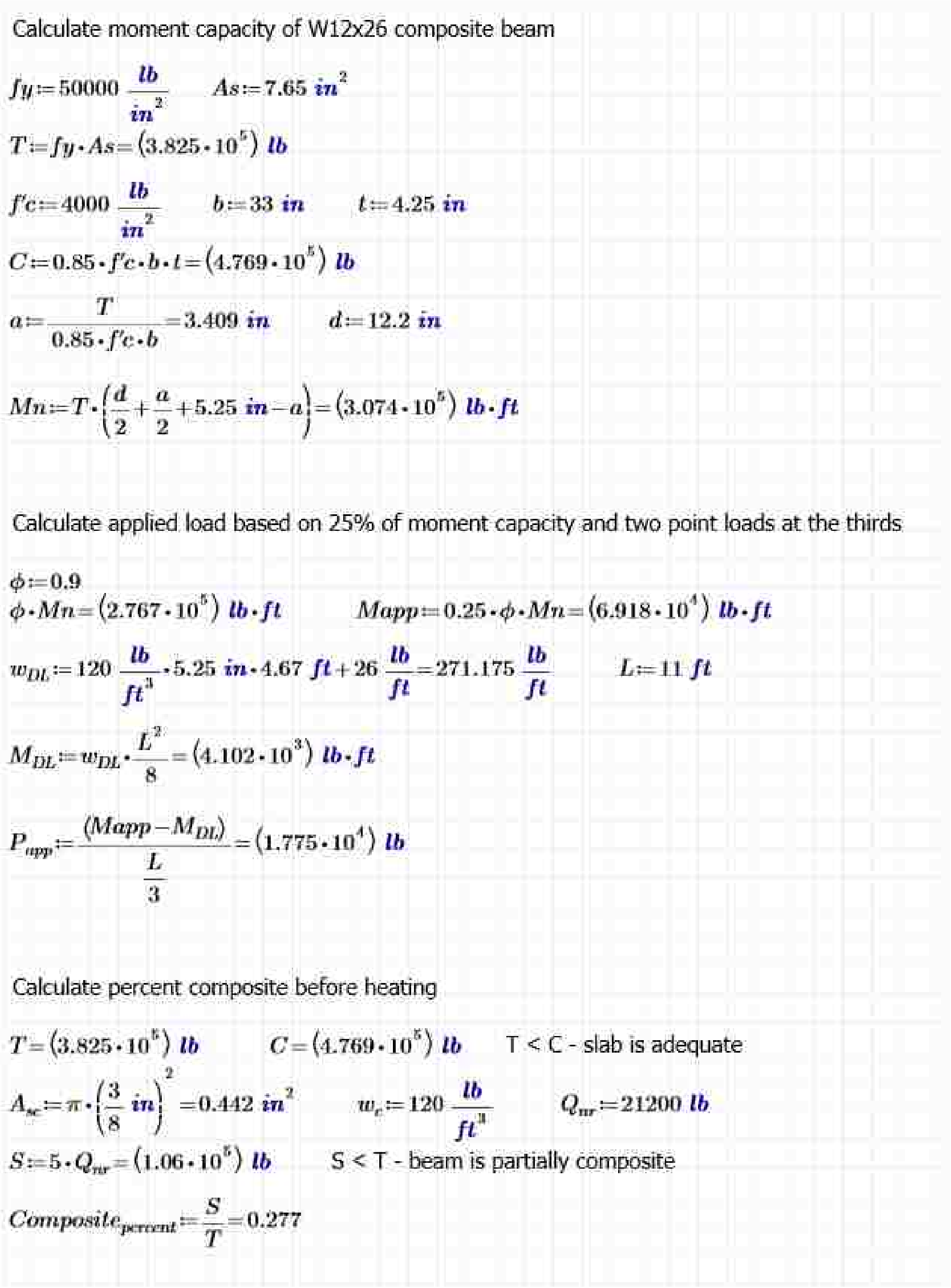

Calculate moment capacity of W12x26 composite beam

$fy := 50000\ \frac{lb}{in^2} \qquad As := 7.65\ in^2$

$T := fy \cdot As = \left(3.825 \cdot 10^5\right)\ lb$

$f'c := 4000\ \frac{lb}{in^2} \qquad b := 33\ in \qquad t := 4.25\ in$

$C := 0.85 \cdot f'c \cdot b \cdot t = \left(4.769 \cdot 10^5\right)\ lb$

$a := \frac{T}{0.85 \cdot f'c \cdot b} = 3.409\ in \qquad d := 12.2\ in$

$Mn := T \cdot \left(\frac{d}{2} + \frac{a}{2} + 5.25\ in - a\right) = \left(3.074 \cdot 10^5\right)\ lb \cdot ft$

Calculate applied load based on 25% of moment capacity and two point loads at the thirds

$\phi := 0.9$

$\phi \cdot Mn = \left(2.767 \cdot 10^5\right)\ lb \cdot ft \qquad Mapp := 0.25 \cdot \phi \cdot Mn = \left(6.918 \cdot 10^4\right)\ lb \cdot ft$

$w_{DL} := 120\ \frac{lb}{ft^3} \cdot 5.25\ in \cdot 4.67\ ft + 26\ \frac{lb}{ft} = 271.175\ \frac{lb}{ft} \qquad L := 11\ ft$

$M_{DL} := w_{DL} \cdot \frac{L^2}{8} = \left(4.102 \cdot 10^3\right)\ lb \cdot ft$

$P_{app} := \frac{\left(Mapp - M_{DL}\right)}{\frac{L}{3}} = \left(1.775 \cdot 10^4\right)\ lb$

Calculate percent composite before heating

$T = \left(3.825 \cdot 10^5\right)\ lb \qquad C = \left(4.769 \cdot 10^5\right)\ lb$ T < C - slab is adequate

$A_{sc} := \pi \cdot \left(\frac{3}{8}\ in\right)^2 = 0.442\ in^2 \qquad w_c := 120\ \frac{lb}{ft^3} \qquad Q_{nr} := 21200\ lb$

$S := 5 \cdot Q_{nr} = \left(1.06 \cdot 10^5\right)\ lb$ S < T - beam is partially composite

$Composite_{percent} := \frac{S}{T} = 0.277$

www.manaraa.com

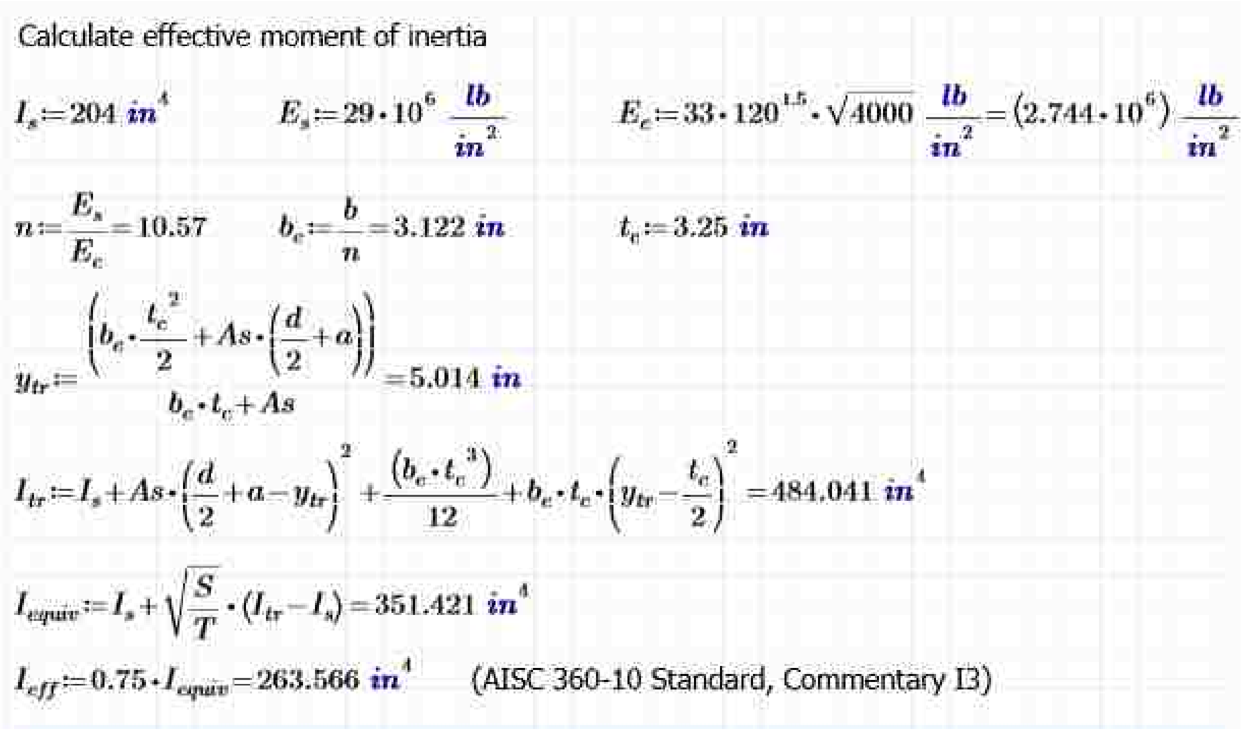

Calculate effective moment of inertia

$I_s := 204\ in^4$ $\quad E_s := 29 \cdot 10^6\ \frac{lb}{in^2}$ $\quad E_c := 33 \cdot 120^{1.5} \cdot \sqrt{4000}\ \frac{lb}{in^2} = \left(2.744 \cdot 10^6\right) \frac{lb}{in^2}$

$n := \frac{E_s}{E_c} = 10.57$ $\quad b_e := \frac{b}{n} = 3.122\ in$ $\quad t_c := 3.25\ in$

$$y_{tr} := \frac{\left(b_e \cdot \frac{t_c^{\,2}}{2} + As \cdot \left(\frac{d}{2} + a\right)\right)}{b_e \cdot t_c + As} = 5.014\ in$$

$$I_{tr} := I_s + As \cdot \left(\frac{d}{2} + a - y_{tr}\right)^2 + \frac{\left(b_e \cdot t_c^{\,3}\right)}{12} + b_e \cdot t_c \cdot \left(y_{tr} - \frac{t_c}{2}\right)^2 = 484.041\ in^4$$

$$I_{equiv} := I_s + \sqrt{\frac{S}{T}} \cdot \left(I_{tr} - I_s\right) = 351.421\ in^4$$

$I_{eff} := 0.75 \cdot I_{equiv} = 263.566\ in^4$ (AISC 360-10 Standard, Commentary I3)

www.manaraa.com

Appendix B – SFRM Thickness Calculation

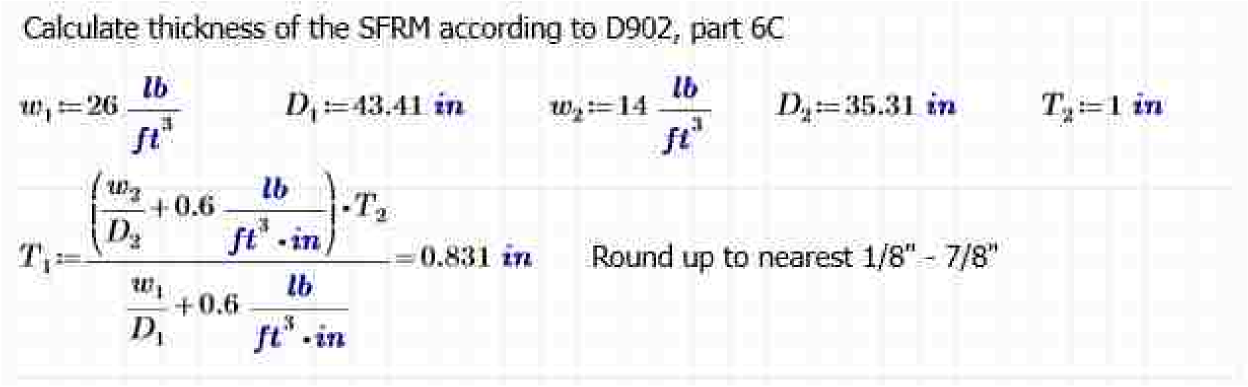

Calculate thickness of the SFRM according to D902, part 6C

$w_1 := 26 \frac{lb}{ft^3}$ $D_1 := 43.41\ in$ $w_2 := 14 \frac{lb}{ft^3}$ $D_2 := 35.31\ in$ $T_2 := 1\ in$

$$T_1 := \frac{\left(\frac{w_2}{D_2} + 0.6 \frac{lb}{ft^3 \cdot in}\right) \cdot T_2}{\frac{w_1}{D_1} + 0.6 \frac{lb}{ft^3 \cdot in}} = 0.831\ in$$

Round up to nearest 1/8" - 7/8"

www.manaraa.com

Appendix C – Concrete Strength

At 28 days after the pour:

Cylinder	f'c (psi)
1	3815.4
2	3723.0
3	3745.1

On the day of the protected beam test (about 6 months after the pour):

Cylinder	f'c (psi)
1	4345.1
2	4343.1
3	3992.8

On the day of the unprotected beam test (about 8 months after the pour):

Cylinder	f'c (psi)
1	4440.4
2	3994.2
3	4055.8

المنارة للاستشارات
www.manaraa.com

Appendix D– Furnace Outer Shell Temperature

For the unprotected test:

Time (min)	Temp at Location (F)					
	1	2	3	4	5	6
5	61	59	60	60	63	60
10	60	59	59	59	69	61
15	64	67	65	69	76	64
20				154	172	

Note: A fan was placed in front of spots 4 and 5 at 20 minutes, and left there until the furnace was shut off and cooled. This convective cooling greatly reduced the temperatures at this location, where the insulation was damaged.

Note: Temperatures were no longer recorded once the fan was placed in front of the "hot spot" due to personnel needed for other safety requirements near the end of the test.

For the protected test:

Time (min)	Temp at Location (F)					
	1	2	3	4	5	6
15	66	72	68	90	94	65
30	69	80	83	157	181	67
45	73	98	97	180	330	73
60	87	121	152	199	150	81
75	83	129	166	138	153	90
90	96	182	148	169	160	105
105	113	161	166	155	156	124
120	126	183	187	214	189	142
135	136	198	196	188	176	159

Note: A fan was placed in front of spots 4 and 5 at 45 minutes, and left there until the furnace was shut off and cooled. This convective cooling greatly reduced the temperatures at this location, where the insulation was damaged.

المنارة للاستشارات
www.manaraa.com

Appendix E– Matlab Scripts to Determine Temperature of Lumped Mass Steel Section

```
% Amy Kordosky
% Fire Research
% 10/12/2015

% Plot the temperature of the steel versus time for both protected and
% unprotected steel in a various fires curves and heating directions.

clc;
close all;
clear all;

Protection = input('Is the steel member protected? Enter 1 for no, and 2 for yes.');
Fire = input('What type of fire curve do you want? Enter 1 for E119, 2 for Euro Parametric. ');
Fiber = input('What number of lumped masses do you want to analyze? 1, 3 or 4?');

sf = 209.9; %shape factor for W12x26 with 3 sided heating (m^-1)
e = 0.5; %resultant emissivity
hc = 25; %convective heat transfer coefficient
dt = 1; %time step in minutes

k = 0.8; %thermal conductivity of fire compartment
ro = 2000; %density of fire compartment
cp = 840; %specific heat of fire compartment

Av = 3.6; %area of window (m^2)
Af = 25; %area of floor (m^2)
Hv = 1.5; %height of window (m)
At = 110; %area of internal surfaces (m^2)

ef = 800; %fuel load for floor area

%Create the vectors for all of the necessary variables
nsteps=length(0:dt:180); %number of steps we want (total time of fire)
Ts=zeros(nsteps,1); %Temperature of steel when one lumped mass is used
Tf=zeros(nsteps,1); %Temperature of fire
t=zeros(nsteps,1); %time
cs=zeros(nsteps,1); %specific heat of steel
ps=zeros(nsteps,1); %Density of steel
ks=zeros(nsteps,1); %thermal conductivity of steel
ys_reduce=zeros(nsteps,1); %reduction of yeild strength with temperature
E_reduce=zeros(nsteps,1); %reduction of stiffness with temperature
pl_reduce=zeros(nsteps,1); %reduction of proportional limit with temperature
Qin1=zeros(nsteps,1); %Heat flow into lumped mass 1
Qin2=zeros(nsteps,1); %Heat flow into lumped mass 2
Qin3=zeros(nsteps,1); %Heat flow into lumped mass 3
Qin4=zeros(nsteps,1); %Heat flow into lumped mass 4
Qout2=zeros(nsteps,1); %Heat flow out of lumped mass 2
Qout3=zeros(nsteps,1); %Heat flow out of lumped mass 3
Qout4=zeros(nsteps,1); %Heat flow out of lumped mass 4
```

www.manaraa.com

```
Q12=zeros(nsteps,1); %Heat flow tranfer from 1 to 2
Q23=zeros(nsteps,1); %Heat flow tranfer from 2 to 3
Q24=zeros(nsteps,1); %Heat flow tranfer from 2 to 4
Ts1=zeros(nsteps,1); %Temperature of steel section 1
Ts2=zeros(nsteps,1); %Temperature of steel section 2
Ts3=zeros(nsteps,1); %Temperature of steel section 3
Ts4=zeros(nsteps,1); %Temperature of steel section 4

%Create all of the variables at first time step
Ts(1,1) = 20; %initial temperature of steel/room
cs1(1,1) = 425+0.773*Ts(1,1)-.00169*(Ts(1,1))^2+(2.22*10^-6)*(Ts(1,1))^3; %initial value for
specific heat of steel in fiber 1
cs2(1,1) = 425+0.773*Ts(1,1)-.00169*(Ts(1,1))^2+(2.22*10^-6)*(Ts(1,1))^3; %initial value for
specific heat of steel in fiber 2
cs3(1,1) = 425+0.773*Ts(1,1)-.00169*(Ts(1,1))^2+(2.22*10^-6)*(Ts(1,1))^3; %initial value for
specific heat of steel in fiber 3
cs4(1,1) = 425+0.773*Ts(1,1)-.00169*(Ts(1,1))^2+(2.22*10^-6)*(Ts(1,1))^3; %initial value for
specific heat of steel in fiber 4
ks1(1,1) = 54-0.0333*Ts(1,1); %initial value for thermal conductivity of steel in fiber 1
ks2(1,1) = 54-0.0333*Ts(1,1); %initial value for thermal conductivity of steel in fiber 2
ks3(1,1) = 54-0.0333*Ts(1,1); %initial value for thermal conductivity of steel in fiber 3
ks4(1,1) = 54-0.0333*Ts(1,1); %initial value for thermal conductivity of steel in fiber 4
ys_reduce1(1,1) = 1; %initial value of yeild strength reduction in fiber 1
E_reduce1(1,1) = 1; %initial value of modulus of elasticity reduction in fiber 1
pl_reduce1(1,1) = 1; %initial value of proportionality limit reduction in fiber 1
Ts1(1,1) = 20; %initial temperature of steel section 1
Ts2(1,1) = 20; %initial temperature of steel section 2
Ts3(1,1) = 20; %initial temperature of steel section 3
Ts4(1,1) = 20; %initial temperature of steel section 4

if Fiber < 1.5
    if Protection < 1.5
    if Fire < 1.5
        for i = 1:nsteps-1
        t(i+1,1)=t(i,1)+dt;
        [Tf]=E119(Ts(1,1),dt,nsteps); %Fire curve function for E119

[cs1,ps,ks1,ys_reduce1,E_reduce1,pl_reduce1,cs2,ks2,ys_reduce2,E_reduce2,pl_reduce2,cs3,ks3,ys_re
duce3,E_reduce3,pl_reduce3,cs4,ks4,ys_reduce4,E_reduce4,pl_reduce4] = SteelProp( Ts(i,1),0,0,0 );
%Function for temperature dependent steel properties
        Ts(i+1,1)=Ts(i,1)+sf/(ps*cs1)*(hc*(Tf(i,1)-Ts(i,1))+(56.7*10^-9)*e*((Tf(i,1)+273)^4-
(Ts(i,1)+273)^4))*dt*60; %Final temperature of unprotected steel at each time step
        end
    elseif Fire > 1.5
        for i = 1:nsteps-1
        t(i+1,1)=t(i,1)+dt;
        [Tf]=EuroParametric(k,ro,cp,dt,Av,Af,Hv,At,ef,nsteps); %Fire curve function for euro
parametric fire

[cs1,ps,ks1,ys_reduce1,E_reduce1,pl_reduce1,cs2,ks2,ys_reduce2,E_reduce2,pl_reduce2,cs3,ks3,ys_re
duce3,E_reduce3,pl_reduce3,cs4,ks4,ys_reduce4,E_reduce4,pl_reduce4] = SteelProp( Ts(i,1),0,0,0 );
%Function for temperature dependent steel properties
        Ts(i+1,1)=Ts(i,1)+sf/(ps*cs1)*(hc*(((Tf(i,1)+Tf(i+1,1))/2)-Ts(i,1))+(56.7*10^-
9)*e*((((Tf(i,1)+273)+(Tf(i+1,1)+273))/2)^4-(Ts(i,1)+273)^4))*dt*60; %Final temperature of
```

www.manaraa.com

```
unprotected steel at each time step
        end
    end
    end

    if Protection > 1.5
    if Fire < 1.5
        for i = 1:nsteps-1
        t(i+1,1)=t(i,1)+dt;
        [Tf]=E119(Ts(1,1),dt,nsteps); %Fire curve function for E119

[cs1,ps,ks1,ys_reduce1,E_reduce1,pl_reduce1,cs2,ks2,ys_reduce2,E_reduce2,pl_reduce2,cs3,ks3,ys_re
duce3,E_reduce3,pl_reduce3,cs4,ks4,ys_reduce4,E_reduce4,pl_reduce4] = SteelProp( Ts(i,1),0,0,0 );
%Function for temperature dependent steel properties
        [pi,ci1,di,ki1,ci2,ki2,ci3,ki3,ci4,ki4] = InsulationProp( Ts(i,1),0,0,0 ); %Function for
temperature dependent insulation properties
        mu1(i,1)=(ci1*pi*di)/(cs1*ps)*sf;
        Ts(i+1,1)=((dt*60)*sf*(Tf(i,1)-Ts(i,1)))/((ps*cs1*di/ki1)*(1+mu1(i,1)/3))-(exp(-
mu1(i,1)/10)-1)*(Tf(i+1,1)-Tf(i,1))+Ts(i,1); %formulation from Zhang and Usmani 2015 paper
        end
    elseif Fire > 1.5
        for i = 1:nsteps-1
        t(i+1,1)=t(i,1)+dt;
        [Tf]=EuroParametric(k,ro,cp,dt,Av,Af,Hv,At,ef,nsteps); %Fire curve function for euro
parametric fire

[cs1,ps,ks1,ys_reduce1,E_reduce1,pl_reduce1,cs2,ks2,ys_reduce2,E_reduce2,pl_reduce2,cs3,ks3,ys_re
duce3,E_reduce3,pl_reduce3,cs4,ks4,ys_reduce4,E_reduce4,pl_reduce4] = SteelProp( Ts(i,1),0,0,0 );
%Function for temperature dependent steel properties
        [pi,ci1,di,ki1,ci2,ki2,ci3,ki3,ci4,ki4] = InsulationProp( Ts(i,1),0,0,0 ); %Function for
temperature dependent insulation properties

Ts(i+1,1)=Ts(i,1)+sf*ki1/(di*ps*cs1)*(ps*cs1/(ps*cs1+sf*(di*pi*ci1/2)))*((Tf(i,1)+Tf(i+1,1))/2-
Ts(i,1))*dt*60; %Final temperature of protected steel by spray-on insulation at each time step
        end
    end
    end

plot(t,Ts,t,Tf)
xlabel('Time, min')
ylabel('Temperature, C')
title('1 Lumped Mass Approach- Heated Uniformally')
legend('Steel', 'Fire');

end

if (1.5<Fiber) && (Fiber<3.5)
        Puin1=.343; %perimeter of section 1 that is exposed to fire (meters)
        Puin2=.514; %perimeter of section 2 that is exposed to fire (meters)
        Puin3=.178; %perimeter of section 3 that is exposed to fire (meters)
        Puout3=0; %perimeter of section 3 that is unexposed to fire (meters) (zero when
adiabatic)
        a1= .00159; %Cross sectional area of section 1 (meters^2)
        a2= .00150; %Cross sectional area of section 2 (meters^2)
```

www.manaraa.com

```
        a3= .00159; %Cross sectional area of section 3 (meters^2)
        tw= .00584; %thickness of web (meters)
        y12=.150; %distance between center of gravity of section 1 and 2 (meters)
        y23=.150; %distance between center of gravity of section 2 and 3 (meters)
    if Protection < 1.5
    if Fire < 1.5
        for i = 1:nsteps-1
        t(i+1,1)=t(i,1)+dt;
        [Tf]=E119(Ts(1,1),dt,nsteps); %Fire curve function for E119

[cs1,ps,ks1,ys_reduce1,E_reduce1,pl_reduce1,cs2,ks2,ys_reduce2,E_reduce2,pl_reduce2,cs3,ks3,ys_re
duce3,E_reduce3,pl_reduce3,cs4,ks4,ys_reduce4,E_reduce4,pl_reduce4] = SteelProp(
Ts1(i,1),Ts2(i,1),Ts3(i,1),0 ); %Function for temperature dependent steel properties
        Qin1(i,1)=Puin1*(hc*(Tf(i,1)-Ts1(i,1))+(56.7*10^-9)*e*((Tf(i,1)+273)^4-
(Ts1(i,1)+273)^4));
        Qin2(i,1)=Puin2*(hc*(Tf(i,1)-Ts2(i,1))+(56.7*10^-9)*e*((Tf(i,1)+273)^4-
(Ts2(i,1)+273)^4));
        Qin3(i,1)=Puin3*(hc*(Tf(i,1)-Ts3(i,1))+(56.7*10^-9)*e*((Tf(i,1)+273)^4-
(Ts3(i,1)+273)^4));
        Qout3(i,1)=Puout3*(hc*((Ts3(i,1)-20))+(56.7*10^-9)*e*((Ts3(i,1)+273)^4-(20+273)^4)); %use
if we have ambient temperature release or no temperature release
        Q12(i,1)=tw*(Ts1(i,1)-Ts2(i,1))/y12*(ks1+ks2)/2;
        Q23(i,1)=tw*(Ts2(i,1)-Ts3(i,1))/y23*(ks2+ks3)/2;
        Ts1(i+1,1)=(dt*60)/(ps*cs1*a1)*(Qin1(i,1)-Q12(i,1))+Ts1(i,1);
        Ts2(i+1,1)=(dt*60)/(ps*cs2*a2)*(Qin2(i,1)+Q12(i,1)-Q23(i,1))+Ts2(i,1);
        Ts3(i+1,1)=(dt*60)/(ps*cs3*a3)*(Qin3(i,1)+Q23(i,1)-Qout3(i,1))+Ts3(i,1);
        end
    elseif Fire > 1.5
        for i = 1:nsteps-1
        t(i+1,1)=t(i,1)+dt;
        [Tf]=EuroParametric(k,ro,cp,dt,Av,Af,Hv,At,ef,nsteps); %Fire curve function for euro
parametric fire

[cs1,ps,ks1,ys_reduce1,E_reduce1,pl_reduce1,cs2,ks2,ys_reduce2,E_reduce2,pl_reduce2,cs3,ks3,ys_re
duce3,E_reduce3,pl_reduce3,cs4,ks4,ys_reduce4,E_reduce4,pl_reduce4] = SteelProp(
Ts1(i,1),Ts2(i,1),Ts3(i,1),0 ); %Function for temperature dependent steel properties
        Qin1(i,1)=Puin1*(hc*(Tf(i,1)-Ts1(i,1))+(56.7*10^-9)*e*((Tf(i,1)+273)^4-
(Ts1(i,1)+273)^4));
        Qin2(i,1)=Puin2*(hc*(Tf(i,1)-Ts2(i,1))+(56.7*10^-9)*e*((Tf(i,1)+273)^4-
(Ts2(i,1)+273)^4));
        Qin3(i,1)=Puin3*(hc*(Tf(i,1)-Ts3(i,1))+(56.7*10^-9)*e*((Tf(i,1)+273)^4-
(Ts3(i,1)+273)^4));
        Qout3(i,1)=Puout3*hc*((Ts3(i,1)-20))+Puout3*(56.7*10^-9)*e*((Ts3(i,1)+273)^4-(20+273)^4);
%use if we have ambient temperature release or no temperature release (cap)
        Q12(i,1)=tw*(Ts1(i,1)-Ts2(i,1))/y12*(ks1+ks2)/2;
        Q23(i,1)=tw*(Ts2(i,1)-Ts3(i,1))/y23*(ks2+ks3)/2;
        Ts1(i+1,1)=(dt*60)/(ps*cs1*a1)*(Qin1(i,1)-Q12(i,1))+Ts1(i,1);
        Ts2(i+1,1)=(dt*60)/(ps*cs2*a2)*(Qin2(i,1)+Q12(i,1)-Q23(i,1))+Ts2(i,1);
        Ts3(i+1,1)=(dt*60)/(ps*cs3*a3)*(Qin3(i,1)+Q23(i,1)-Qout3(i,1))+Ts3(i,1);
        end
    end
    end

    if Protection > 1.5
```

المنارة للاستشارات
www.manaraa.com

```
    if Fire < 1.5
        for i = 1:nsteps-1
        t(i+1,1)=t(i,1)+dt;
        [Tf]=E119(Ts(1,1),dt,nsteps); %Fire curve function for E119

[cs1,ps,ks1,ys_reduce1,E_reduce1,pl_reduce1,cs2,ks2,ys_reduce2,E_reduce2,pl_reduce2,cs3,ks3,ys_re
duce3,E_reduce3,pl_reduce3,cs4,ks4,ys_reduce4,E_reduce4,pl_reduce4] = SteelProp(
Ts1(i,1),Ts2(i,1),Ts3(i,1),0 ); %Function for temperature dependent steel properties
        [pi,ci1,di,ki1,ci2,ki2,ci3,ki3,ci4,ki4] = InsulationProp( Ts1(i,1),Ts2(i,1),Ts3(i,1),0 );
%Function for temperature dependent insulation properties
        Qin1(i,1)=Puin1*ki1*(Tf(i,1)-Ts1(i,1))/di;
        Qin2(i,1)=Puin2*ki2*(Tf(i,1)-Ts2(i,1))/di;
        Qin3(i,1)=Puin3*ki3*(Tf(i,1)-Ts3(i,1))/di;
        Qout3(i,1)=Puout3*ki3*(Ts3(i,1)-20)/di; %use if we have ambient temperature release or no
temperature release (cap) and top surface is protected
        Q12(i,1)=tw*(Ts1(i,1)-Ts2(i,1))/y12*(ks1+ks2)/2;
        Q23(i,1)=tw*(Ts2(i,1)-Ts3(i,1))/y23*(ks2+ks3)/2;
        Ts1(i+1,1)=(dt*60)/(ps*cs1*a1+(pi*ci1*di*Puin1)/3)*(Qin1(i,1)-Q12(i,1))+Ts1(i,1); %DIVIDE
BY 3 FROM EUROCODE
        Ts2(i+1,1)=(dt*60)/(ps*cs2*a2+(pi*ci2*di*Puin2)/3)*(Qin2(i,1)+Q12(i,1)-
Q23(i,1))+Ts2(i,1); %DIVIDE BY 3 FROM EUROCODE
        Ts3(i+1,1)=(dt*60)/(ps*cs3*a3+(pi*ci3*di*Puin3)/3)*(Qin3(i,1)+Q23(i,1)-
Qout3(i,1))+Ts3(i,1); %DIVIDE BY 3 FROM EUROCODE
        end
    elseif Fire > 1.5
        for i = 1:nsteps-1
        t(i+1,1)=t(i,1)+dt;
        [Tf]=EuroParametric(k,ro,cp,dt,Av,Af,Hv,At,ef,nsteps); %Fire curve function for euro
parametric fire

[cs1,ps,ks1,ys_reduce1,E_reduce1,pl_reduce1,cs2,ks2,ys_reduce2,E_reduce2,pl_reduce2,cs3,ks3,ys_re
duce3,E_reduce3,pl_reduce3,cs4,ks4,ys_reduce4,E_reduce4,pl_reduce4] = SteelProp(
Ts1(i,1),Ts2(i,1),Ts3(i,1),0 ); %Function for temperature dependent steel properties
        [pi,ci1,di,ki1,ci2,ki2,ci3,ki3,ci4,ki4] = InsulationProp( Ts1(i,1),Ts2(i,1),Ts3(i,1),0 );
%Function for temperature dependent insulation properties
        Qin1(i,1)=Puin1*ki1*(Tf(i,1)-Ts1(i,1))/di;
        Qin2(i,1)=Puin2*ki2*(Tf(i,1)-Ts2(i,1))/di;
        Qin3(i,1)=Puin3*ki3*(Tf(i,1)-Ts3(i,1))/di;
        Qout3(i,1)=Puout3*ki3*(Ts3(i,1)-20)/di; %use if we have ambient temperature release or no
temperature release (cap)
        Q12(i,1)=tw*(Ts1(i,1)-Ts2(i,1))/y12*(ks1+ks2)/2;
        Q23(i,1)=tw*(Ts2(i,1)-Ts3(i,1))/y23*(ks2+ks3)/2;
        Ts1(i+1,1)=(dt*60)/(ps*cs1*a1+(pi*ci1*di*Puin1)/2)*(Qin1(i,1)-Q12(i,1))+Ts1(i,1);
        Ts2(i+1,1)=(dt*60)/(ps*cs2*a2+(pi*ci2*di*Puin2)/2)*(Qin2(i,1)+Q12(i,1)-
Q23(i,1))+Ts2(i,1);
        Ts3(i+1,1)=(dt*60)/(ps*cs3*a3+(pi*ci3*di*Puin3)/2)*(Qin3(i,1)+Q23(i,1)-
Qout3(i,1))+Ts3(i,1);
        end
    end
    end
plot(t*60,Ts1,t*60, Ts2,t*60,Ts3,t*60,Tf)
xlabel('Time, sec')
ylabel('Temperature, C')
title('3 Lumped Mass Approach- Gradient Induced on Strong Axis')
```

المنارة للاستشارات
www.manaraa.com

```
legend('Bottom Flange-Code','Web-Code','Top Flange-Code', 'Fire');
axis([0 11000 0 1200]);
end

if Fiber>3.5
        Puin1=.0719*2; %perimeter of section 1 that is exposed to fire (multiplied by two for
each flange) (meters)
        Puin2=.0531*2; %perimeter of section 2 that is exposed to fire (multiplied by two for
each flange) (meters)
        Puin3=.0334*2; %perimeter of section 3 that is exposed to fire (multiplied by two for
each flange) (meters)
        Puin4=.1651; %perimeter of section 4 that is exposed to fire (meters)
        Puout2=.0145*2; %perimeter of section 2 that is unexposed to fire(multiplied by two for
each flange) (meters) when assumed ambient temperature release
        Puout3=.0386*2; %perimeter of section 3 that is unexposed to fire (multiplied by two for
each flange) (meters) when assumed ambient temperature release
        Puout4=.1651; %perimeter of section 4 that is unexposed to fire (meters) when assumed
ambient temperature release
        a1= .000174*2; %Cross sectional area of section 1 (multiplied by two for each flange)
(meters^2)
        a2= .000174*2; %Cross sectional area of section 2 (multiplied by two for each flange)
(meters^2)
        a3= .000174*2; %Cross sectional area of section 3 (multiplied by two for each flange)
(meters^2)
        a4= .000713; %Cross sectional area of section 4 (meters^2)
        tw= .00432; %thickness of web (meters)
        tf= .00521; %thickness of flange (meters)
        y12=.0334; %distance between center of gravity of section 1 and 2 (meters)
        y23=.0334; %distance between center of gravity of section 2 and 3 (meters)
        y24=.085; %distance between center of gravity of section 2 and 4 (meters)
    if Protection < 1.5
    if Fire < 1.5
        for i = 1:nsteps-1
        t(i+1,1)=t(i,1)+dt;
        [Tf]=E119(Ts(1,1),dt,nsteps); %Fire curve function for E119

[cs1,ps,ks1,ys_reduce1,E_reduce1,pl_reduce1,cs2,ks2,ys_reduce2,E_reduce2,pl_reduce2,cs3,ks3,ys_re
duce3,E_reduce3,pl_reduce3,cs4,ks4,ys_reduce4,E_reduce4,pl_reduce4] = SteelProp(
Ts1(i,1),Ts2(i,1),Ts3(i,1),Ts4(i,1) ); %Function for temperature dependent steel properties
        Qin1(i,1)=Puin1*(hc*(Tf(i,1)-Ts1(i,1))+(56.7*10^-9)*e*((Tf(i,1)+273)^4-
(Ts1(i,1)+273)^4));
        Qin2(i,1)=Puin2*(hc*(Tf(i,1)-Ts2(i,1))+(56.7*10^-9)*e*((Tf(i,1)+273)^4-
(Ts2(i,1)+273)^4));
        Qin3(i,1)=Puin3*(hc*(Tf(i,1)-Ts3(i,1))+(56.7*10^-9)*e*((Tf(i,1)+273)^4-
(Ts3(i,1)+273)^4));
        Qin4(i,1)=Puin4*(hc*(Tf(i,1)-Ts4(i,1))+(56.7*10^-9)*e*((Tf(i,1)+273)^4-
(Ts4(i,1)+273)^4));
        Qout2(i,1)=Puout2*(hc*((Ts2(i,1)-20))+(56.7*10^-9)*e*((Ts2(i,1)+273)^4-(20+273)^4));
        Qout3(i,1)=Puout3*(hc*((Ts3(i,1)-20))+(56.7*10^-9)*e*((Ts3(i,1)+273)^4-(20+273)^4));
        Qout4(i,1)=Puout4*(hc*((Ts4(i,1)-20))+(56.7*10^-9)*e*((Ts4(i,1)+273)^4-(20+273)^4));
        Q12(i,1)=tf*(Ts1(i,1)-Ts2(i,1))/y12*(ks1+ks2)/2;
        Q23(i,1)=tf*(Ts2(i,1)-Ts3(i,1))/y23*(ks2+ks3)/2;
        Q24(i,1)=tw*(Ts2(i,1)-Ts4(i,1))/y24*(ks2+ks4)/2;
        Ts1(i+1,1)=(dt*60)/(ps*cs1*a1)*(Qin1(i,1)-Q12(i,1))+Ts1(i,1);
```

www.manaraa.com

```
        Ts2(i+1,1)=(dt*60)/(ps*cs2*a2)*(Qin2(i,1)+Q12(i,1)-Q23(i,1)-Q24(i,1)-
Qout2(i,1))+Ts2(i,1);
        Ts3(i+1,1)=(dt*60)/(ps*cs3*a3)*(Qin3(i,1)+Q23(i,1)-Qout3(i,1))+Ts3(i,1);
        Ts4(i+1,1)=(dt*60)/(ps*cs4*a4)*(Qin4(i,1)+2*Q24(i,1)-Qout4(i,1))+Ts4(i,1);
        end
    elseif Fire > 1.5
        for i = 1:nsteps-1
        t(i+1,1)=t(i,1)+dt;
        [Tf]=EuroParametric(k,ro,cp,dt,Av,Af,Hv,At,ef,nsteps); %Fire curve function for euro
parametric fire

[cs1,ps,ks1,ys_reduce1,E_reduce1,pl_reduce1,cs2,ks2,ys_reduce2,E_reduce2,pl_reduce2,cs3,ks3,ys_re
duce3,E_reduce3,pl_reduce3,cs4,ks4,ys_reduce4,E_reduce4,pl_reduce4] = SteelProp(
Ts1(i,1),Ts2(i,1),Ts3(i,1),Ts4(i,1) ); %Function for temperature dependent steel properties
        Qin1(i,1)=Puin1*(hc*(Tf(i,1)-Ts1(i,1))+(56.7*10^-9)*e*((Tf(i,1)+273)^4-
(Ts1(i,1)+273)^4));
        Qin2(i,1)=Puin2*(hc*(Tf(i,1)-Ts2(i,1))+(56.7*10^-9)*e*((Tf(i,1)+273)^4-
(Ts2(i,1)+273)^4));
        Qin3(i,1)=Puin3*(hc*(Tf(i,1)-Ts3(i,1))+(56.7*10^-9)*e*((Tf(i,1)+273)^4-
(Ts3(i,1)+273)^4));
        Qin4(i,1)=Puin4*(hc*(Tf(i,1)-Ts4(i,1))+(56.7*10^-9)*e*((Tf(i,1)+273)^4-
(Ts4(i,1)+273)^4));
        Qout2(i,1)=Puout2*(hc*((Ts2(i,1)-20))+(56.7*10^-9)*e*((Ts2(i,1)+273)^4-(20+273)^4));
        Qout3(i,1)=Puout3*(hc*((Ts3(i,1)-20))+(56.7*10^-9)*e*((Ts3(i,1)+273)^4-(20+273)^4));
        Qout4(i,1)=Puout4*(hc*((Ts4(i,1)-20))+(56.7*10^-9)*e*((Ts4(i,1)+273)^4-(20+273)^4));
        Q12(i,1)=tf*(Ts1(i,1)-Ts2(i,1))/y12*(ks1+ks2)/2;
        Q23(i,1)=tf*(Ts2(i,1)-Ts3(i,1))/y23*(ks2+ks3)/2;
        Q24(i,1)=tw*(Ts2(i,1)-Ts4(i,1))/y24*(ks2+ks4)/2;
        Ts1(i+1,1)=(dt*60)/(ps*cs1*a1)*(Qin1(i,1)-Q12(i,1))+Ts1(i,1);
        Ts2(i+1,1)=(dt*60)/(ps*cs2*a2)*(Qin2(i,1)+Q12(i,1)-Q23(i,1)-Q24(i,1)-
Qout2(i,1))+Ts2(i,1);
        Ts3(i+1,1)=(dt*60)/(ps*cs3*a3)*(Qin3(i,1)+Q23(i,1)-Qout3(i,1))+Ts3(i,1);
        Ts4(i+1,1)=(dt*60)/(ps*cs4*a4)*(Qin4(i,1)+2*Q24(i,1)-Qout4(i,1))+Ts4(i,1);
        end
    end
    end

    if Protection > 1.5
    if Fire < 1.5
        for i = 1:nsteps-1
        t(i+1,1)=t(i,1)+dt;
        [Tf]=E119(Ts(1,1),dt,nsteps); %Fire curve function for E119

[cs1,ps,ks1,ys_reduce1,E_reduce1,pl_reduce1,cs2,ks2,ys_reduce2,E_reduce2,pl_reduce2,cs3,ks3,ys_re
duce3,E_reduce3,pl_reduce3,cs4,ks4,ys_reduce4,E_reduce4,pl_reduce4] = SteelProp(
Ts1(i,1),Ts2(i,1),Ts3(i,1),Ts4(i,1) ); %Function for temperature dependent steel properties
        [pi,ci1,di,ki1,ci2,ki2,ci3,ki3,ci4,ki4] = InsulationProp(
Ts1(i,1),Ts2(i,1),Ts3(i,1),Ts4(i,1) ); %Function for temperature dependent insulation properties
        Qin1(i,1)=Puin1*ki1*(Tf(i,1)-Ts1(i,1))/di;
        Qin2(i,1)=Puin2*ki2*(Tf(i,1)-Ts2(i,1))/di;
        Qin3(i,1)=Puin3*ki3*(Tf(i,1)-Ts3(i,1))/di;
        Qin4(i,1)=Puin4*ki4*(Tf(i,1)-Ts4(i,1))/di;
        Qout2(i,1)=Puout2*ki2*(Ts2(i,1)-20)/di;
        Qout3(i,1)=Puout3*ki3*(Ts3(i,1)-20)/di;
```

www.manaraa.com

```
        Qout4(i,1)=Puout4*ki4*(Ts3(i,1)-20)/di;
        Q12(i,1)=tf*(Ts1(i,1)-Ts2(i,1))/y12*(ks1+ks2)/2;
        Q23(i,1)=tf*(Ts2(i,1)-Ts3(i,1))/y23*(ks2+ks3)/2;
        Q24(i,1)=tw*(Ts2(i,1)-Ts4(i,1))/y24*(ks2+ks4)/2;
        Ts1(i+1,1)=(dt*60)/(ps*cs1*a1+(pi*ci1*di*Puin1)/2)*(Qin1(i,1)-Q12(i,1))+Ts1(i,1);
        Ts2(i+1,1)=(dt*60)/(ps*cs2*a2+(pi*ci2*di*Puin2)/2)*(Qin2(i,1)+Q12(i,1)-Q23(i,1)-Q24(i,1)-
Qout2(i,1))+Ts2(i,1);
        Ts3(i+1,1)=(dt*60)/(ps*cs3*a3+(pi*ci3*di*Puin3)/2)*(Qin3(i,1)+Q23(i,1)-
Qout3(i,1))+Ts3(i,1);
        Ts4(i+1,1)=(dt*60)/(ps*cs4*a4+(pi*ci4*di*Puin4)/2)*(Qin4(i,1)+2*Q24(i,1)-
Qout4(i,1))+Ts4(i,1);
        end
    elseif Fire > 1.5
        for i = 1:nsteps-1
        t(i+1,1)=t(i,1)+dt;
        [Tf]=EuroParametric(k,ro,cp,dt,Av,Af,Hv,At,ef,nsteps); %Fire curve function for euro
parametric fire

[cs1,ps,ks1,ys_reduce1,E_reduce1,pl_reduce1,cs2,ks2,ys_reduce2,E_reduce2,pl_reduce2,cs3,ks3,ys_re
duce3,E_reduce3,pl_reduce3,cs4,ks4,ys_reduce4,E_reduce4,pl_reduce4] = SteelProp(
Ts1(i,1),Ts2(i,1),Ts3(i,1),Ts4(i,1) ); %Function for temperature dependent steel properties
        [pi,ci1,di,ki1,ci2,ki2,ci3,ki3,ci4,ki4] = InsulationProp(
Ts1(i,1),Ts2(i,1),Ts3(i,1),Ts4(i,1) ); %Function for temperature dependent insulation properties
        Qin1(i,1)=Puin1*ki1*(Tf(i,1)-Ts1(i,1))/di;
        Qin2(i,1)=Puin2*ki2*(Tf(i,1)-Ts2(i,1))/di;
        Qin3(i,1)=Puin3*ki3*(Tf(i,1)-Ts3(i,1))/di;
        Qin4(i,1)=Puin4*ki4*(Tf(i,1)-Ts4(i,1))/di;
        Qout2(i,1)=Puout2*ki2*(Ts2(i,1)-20)/di;
        Qout3(i,1)=Puout3*ki3*(Ts3(i,1)-20)/di;
        Qout4(i,1)=Puout4*ki4*(Ts3(i,1)-20)/di;
        Q12(i,1)=tf*(Ts1(i,1)-Ts2(i,1))/y12*(ks1+ks2)/2;
        Q23(i,1)=tf*(Ts2(i,1)-Ts3(i,1))/y23*(ks2+ks3)/2;
        Q24(i,1)=tw*(Ts2(i,1)-Ts4(i,1))/y24*(ks2+ks4)/2;
        Ts1(i+1,1)=(dt*60)/(ps*cs1*a1+(pi*ci1*di*Puin1)/2)*(Qin1(i,1)-Q12(i,1))+Ts1(i,1);
        Ts2(i+1,1)=(dt*60)/(ps*cs2*a2+(pi*ci2*di*Puin2)/2)*(Qin2(i,1)+Q12(i,1)-Q23(i,1)-Q24(i,1)-
Qout2(i,1))+Ts2(i,1);
        Ts3(i+1,1)=(dt*60)/(ps*cs3*a3+(pi*ci3*di*Puin3)/2)*(Qin3(i,1)+Q23(i,1)-
Qout3(i,1))+Ts3(i,1);
        Ts4(i+1,1)=(dt*60)/(ps*cs4*a4+(pi*ci4*di*Puin4)/2)*(Qin4(i,1)+2*Q24(i,1)-
Qout4(i,1))+Ts4(i,1);
        end
    end
    end
plot(t*60,Ts1,t*60,Ts2,t*60,Ts3,t*60,Ts4,t*60,Tf)
xlabel('Time, sec')
ylabel('Temperature, C')
title('4 Lumped Mass Approach- Gradient Induced on Weak Axis')
legend('Bottom of Flange','Middle of Flange','Top of Flange','Web','Fire');
end
```

Published with MATLAB® R2015a

www.manaraa.com

```
function [ Tf ] = E119( tsi,dt,nsteps )
%This function creates the fire curve for an E119 fire
%   This functions output is the temperature of the fire. It requires an
%   input of the initial room temperature(tsi), the time step (dt), and the
%   step chosen (nsteps)

Tf=zeros(nsteps,1);
t=zeros(nsteps,1);

for i = 1:nsteps-1
 t(i+1,1)=t(i,1)+dt;
 Tf(i,1)=750*(1-exp(-3.79553*sqrt(t(i,1)/60)))+170.41*sqrt(t(i,1)/60)+tsi; %The temperature of
the fire
 Tf(i+1,1)=750*(1-exp(-3.79553*sqrt(t(i+1,1)/60)))+170.41*sqrt(t(i+1,1)/60)+tsi; %For the last
point in the fire curve (approximate)
end

end
```

Published with MATLAB® R2015a

المنارة للاستشارات

www.manaraa.com

```
function [ pi,ci1,di,ki1,ci2,ki2,ci3,ki3,ci4,ki4 ] = InsulationProp( Ts1, Ts2, Ts3, Ts4 )
%This function creates the properties of the insulation material
%   Input the temperature of steel, and output is the density of the
%   insulation (pi), specific heat of the insulation (ci), thickness
%   of the insulation in meters (di), and thermal conductivity of the
%   insulation(ki).

pi = 240; %density of insulation (not temperature dependent) kg/m^3
di = 0.0222; %thickness of insulation (not temperature dependent) m

if Ts1<=20
   ki1=0.059;
elseif (20<Ts1) && (Ts1<=204)
   ki1=92.391*10^-6*Ts1+0.0571522;
elseif (204<Ts1) && (Ts1<=399)
   ki1=225.641*10^-6*Ts1+0.029969;
elseif (399<Ts1) && (Ts1<=1093)
   ki1=244.957*10^-6*Ts1+0.022262;
else
   ki1=0.290;
end
if Ts1<=20
   ci1=862;
elseif (20<Ts1) && (Ts1<=204)
   ci1=0.793478*Ts1+846.13;
elseif (204<Ts1) && (Ts1<=399)
   ci1=1.35385*Ts1+731.815;
elseif (399<Ts1) && (Ts1<=1093)
   ci1=0.276657*Ts1+1161.61;
else
   ci1=1464;
end
if Ts2<=20
   ki2=0.059;
elseif (20<Ts2) && (Ts2<=204)
   ki2=92.391*10^-6*Ts2+0.0571522;
elseif (204<Ts2) && (Ts2<=399)
   ki2=225.641*10^-6*Ts2+0.029969;
elseif (399<Ts2) && (Ts2<=1093)
   ki2=244.957*10^-6*Ts2+0.022262;
else
   ki2=0.290;
end
if Ts2<=20
   ci2=862;
elseif (20<Ts2) && (Ts2<=204)
   ci2=0.793478*Ts2+846.13;
elseif (204<Ts2) && (Ts2<=399)
   ci2=1.35385*Ts2+731.815;
elseif (399<Ts2) && (Ts2<=1093)
   ci2=0.276657*Ts2+1161.61;
else
   ci2=1464;
```

المنارة للاستشارات

www.manaraa.com

```
end
if Ts3<=20
   ki3=0.059;
elseif (20<Ts3) && (Ts3<=204)
   ki3=92.391*10^-6*Ts3+0.0571522;
elseif (204<Ts3) && (Ts3<=399)
   ki3=225.641*10^-6*Ts3+0.029969;
elseif (399<Ts3) && (Ts3<=1093)
   ki3=244.957*10^-6*Ts3+0.022262;
else
   ki3=0.290;
end
if Ts3<=20
   ci3=862;
elseif (20<Ts3) && (Ts3<=204)
   ci3=0.793478*Ts3+846.13;
elseif (204<Ts3) && (Ts3<=399)
   ci3=1.35385*Ts3+731.815;
elseif (399<Ts3) && (Ts3<=1093)
   ci3=0.276657*Ts3+1161.61;
else
   ci3=1464;
end
if Ts4<=20
   ki4=0.059;
elseif (20<Ts4) && (Ts4<=204)
   ki4=92.391*10^-6*Ts4+0.0571522;
elseif (204<Ts4) && (Ts4<=399)
   ki4=225.641*10^-6*Ts4+0.029969;
elseif (399<Ts4) && (Ts4<=1093)
   ki4=244.957*10^-6*Ts4+0.022262;
else
   ki4=0.290;
end
if Ts4<=20
   ci4=862;
elseif (20<Ts4) && (Ts4<=204)
   ci4=0.793478*Ts4+846.13;
elseif (204<Ts4) && (Ts4<=399)
   ci4=1.35385*Ts4+731.815;
elseif (399<Ts4) && (Ts4<=1093)
   ci4=0.276657*Ts4+1161.61;
else
   ci4=1464;
end

end
```

Published with MATLAB® R2015a

www.manaraa.com

```
function
[cs1,ps,ks1,ys_reduce1,E_reduce1,pl_reduce1,cs2,ks2,ys_reduce2,E_reduce2,pl_reduce2,cs3,ks3,ys_re
duce3,E_reduce3,pl_reduce3,cs4,ks4,ys_reduce4,E_reduce4,pl_reduce4] = SteelProp( Ts1,Ts2,Ts3,Ts4)
%This function creates the temperature dependent steel properties
%   Input the temperature of steel, and output is the specific heat(cs),
%   density(ps), thermal conductivity(ks), yeild strength (ys), modulus of
%   elasticity (E), and proportionality limit (pl) of steel.

ps=7850; %density of steel (not temperature dependent)

  if Ts1<600
     cs1=425+0.773.*Ts1-.00169.*(Ts1).^2+(2.22*10^-6).*(Ts1).^3;
 elseif (600<=Ts1) && (Ts1<735)
     cs1=666+13002/(738-Ts1);
 elseif (735<=Ts1) && (Ts1<900)
     cs1=545+17820/(Ts1-731);
 else
     cs1=650;
  end

 if Ts1<800
     ks1=54-0.0333.*Ts1;
 else
     ks1=27.3;
 end

 if Ts1<400
     ys_reduce1=1;
 elseif (400<=Ts1) && (Ts1<500)
     ys_reduce1=(-2.2*10^-3).*Ts1+1.88;
 elseif (500<=Ts1) && (Ts1<600)
     ys_reduce1=(-3.1*10^-3).*Ts1+2.33;
 elseif (600<=Ts1) && (Ts1<700)
     ys_reduce1=(-2.4*10^-3).*Ts1+1.91;
 elseif (700<=Ts1) && (Ts1<800)
     ys_reduce1=(-1.2*10^-3).*Ts1+1.07;
 elseif (800<=Ts1) && (Ts1<900)
     ys_reduce1=(-500*10^-6).*Ts1+.51;
 elseif (900<=Ts1) && (Ts1<1200)
     ys_reduce1=(-200*10^-6).*Ts1+.24;
 else Ts1>1200
     ys_reduce1=0;
 end

 if Ts1<100
     pl_reduce1=1;
 elseif (100<=Ts1) && (Ts1<200)
     pl_reduce1=(-1.93*10^-3).*Ts1+1.193;
 elseif (200<=Ts1) && (Ts1<300)
     pl_reduce1=(-1.94*10^-3).*Ts1+1.195;
 elseif (300<=Ts1) && (Ts1<400)
     pl_reduce1=(-1.93*10^-3).*Ts1+1.192;
 elseif (400<=Ts1) && (Ts1<500)
```

www.manaraa.com

```
    pl_reduce1=(-0.6*10^-3).*Ts1+0.66;
elseif (500<=Ts1) && (Ts1<600)
    pl_reduce1=(-1.8*10^-3).*Ts1+1.26;
elseif (600<=Ts1) && (Ts1<700)
    pl_reduce1=(-1.05*10^-3).*Ts1+.81;
elseif (700<=Ts1) && (Ts1<800)
    pl_reduce1=(-.25*10^-3).*Ts1+.25;
elseif (800<=Ts1) && (Ts1<1200)
    pl_reduce1=(-.125*10^-3).*Ts1+.15;
else Ts1>1200
    pl_reduce1=0;
end

if Ts1<100
    E_reduce1=1;
elseif (100<=Ts1) && (Ts1<500)
    E_reduce1=(-1.0*10^-3).*Ts1+1.1;
elseif (500<=Ts1) && (Ts1<600)
    E_reduce1=(-2.9*10^-3).*Ts1+2.05;
elseif (600<=Ts1) && (Ts1<700)
    E_reduce1=(-1.8*10^-3).*Ts1+1.39;
elseif (700<=Ts1) && (Ts1<800)
    E_reduce1=(-.4*10^-3).*Ts1+.41;
elseif (800<=Ts1) && (Ts1<1200)
    E_reduce1=(-.225*10^-3).*Ts1+.27;
else Ts1>1200
    E_reduce1=0;
end

 if Ts2<600
    cs2=425+0.773.*Ts2-.00169.*(Ts2).^2+(2.22*10^-6).*(Ts2).^3;
elseif (600<=Ts2) && (Ts2<735)
    cs2=666+13002/(738-Ts2);
elseif (735<=Ts2) && (Ts2<900)
    cs2=545+17820/(Ts2-731);
else
    cs2=650;
 end

if Ts2<800
    ks2=54-0.0333.*Ts2;
else
    ks2=27.3;
end

if Ts2<400
    ys_reduce2=1;
elseif (400<=Ts2) && (Ts2<500)
    ys_reduce2=(-2.2*10^-3).*Ts2+1.88;
elseif (500<=Ts2) && (Ts2<600)
    ys_reduce2=(-3.1*10^-3).*Ts2+2.33;
elseif (600<=Ts2) && (Ts2<700)
    ys_reduce2=(-2.4*10^-3).*Ts2+1.91;
elseif (700<=Ts2) && (Ts2<800)
```

www.manaraa.com

```
    ys_reduce2=(-1.2*10^-3).*Ts2+1.07;
elseif (800<=Ts2) && (Ts2<900)
    ys_reduce2=(-500*10^-6).*Ts2+.51;
elseif (900<=Ts2) && (Ts2<1200)
    ys_reduce2=(-200*10^-6).*Ts2+.24;
else Ts2>1200
    ys_reduce2=0;
end

if Ts2<100
    pl_reduce2=1;
elseif (100<=Ts2) && (Ts2<200)
    pl_reduce2=(-1.93*10^-3).*Ts2+1.193;
elseif (200<=Ts2) && (Ts2<300)
    pl_reduce2=(-1.94*10^-3).*Ts2+1.195;
elseif (300<=Ts2) && (Ts2<400)
    pl_reduce2=(-1.93*10^-3).*Ts2+1.192;
elseif (400<=Ts2) && (Ts2<500)
    pl_reduce2=(-0.6*10^-3).*Ts2+0.66;
elseif (500<=Ts2) && (Ts2<600)
    pl_reduce2=(-1.8*10^-3).*Ts2+1.26;
elseif (600<=Ts2) && (Ts2<700)
    pl_reduce2=(-1.05*10^-3).*Ts2+.81;
elseif (700<=Ts2) && (Ts2<800)
    pl_reduce2=(-.25*10^-3).*Ts2+.25;
elseif (800<=Ts2) && (Ts2<1200)
    pl_reduce2=(-.125*10^-3).*Ts2+.15;
else Ts2>1200
    pl_reduce2=0;
end

if Ts2<100
    E_reduce2=1;
elseif (100<=Ts2) && (Ts2<500)
    E_reduce2=(-1.0*10^-3).*Ts2+1.1;
elseif (500<=Ts2) && (Ts2<600)
    E_reduce2=(-2.9*10^-3).*Ts2+2.05;
elseif (600<=Ts2) && (Ts2<700)
    E_reduce2=(-1.8*10^-3).*Ts2+1.39;
elseif (700<=Ts2) && (Ts2<800)
    E_reduce2=(-.4*10^-3).*Ts2+.41;
elseif (800<=Ts2) && (Ts2<1200)
    E_reduce2=(-.225*10^-3).*Ts2+.27;
else Ts2>1200
    E_reduce2=0;
end

 if Ts3<600
    cs3=425+0.773.*Ts3-.00169.*(Ts3).^2+(2.22*10^-6).*(Ts3).^3;
elseif (600<=Ts3) && (Ts3<735)
    cs3=666+13002/(738-Ts3);
elseif (735<=Ts3) && (Ts3<900)
    cs3=545+17820/(Ts3-731);
else
```

www.manaraa.com

```
    cs3=650;
 end

if Ts3<800
    ks3=54-0.0333.*Ts3;
else
    ks3=27.3;
end

if Ts3<400
    ys_reduce3=1;
elseif (400<=Ts3) && (Ts3<500)
    ys_reduce3=(-2.2*10^-3).*Ts3+1.88;
elseif (500<=Ts3) && (Ts3<600)
    ys_reduce3=(-3.1*10^-3).*Ts3+2.33;
elseif (600<=Ts3) && (Ts3<700)
    ys_reduce3=(-2.4*10^-3).*Ts3+1.91;
elseif (700<=Ts3) && (Ts3<800)
    ys_reduce3=(-1.2*10^-3).*Ts3+1.07;
elseif (800<=Ts3) && (Ts3<900)
    ys_reduce3=(-500*10^-6).*Ts3+.51;
elseif (900<=Ts3) && (Ts3<1200)
    ys_reduce3=(-200*10^-6).*Ts3+.24;
else Ts3>1200
    ys_reduce3=0;
end

if Ts3<100
    pl_reduce3=1;
elseif (100<=Ts3) && (Ts3<200)
    pl_reduce3=(-1.93*10^-3).*Ts3+1.193;
elseif (200<=Ts3) && (Ts3<300)
    pl_reduce3=(-1.94*10^-3).*Ts3+1.195;
elseif (300<=Ts3) && (Ts3<400)
    pl_reduce3=(-1.93*10^-3).*Ts3+1.192;
elseif (400<=Ts3) && (Ts3<500)
    pl_reduce3=(-0.6*10^-3).*Ts3+0.66;
elseif (500<=Ts3) && (Ts3<600)
    pl_reduce3=(-1.8*10^-3).*Ts3+1.26;
elseif (600<=Ts3) && (Ts3<700)
    pl_reduce3=(-1.05*10^-3).*Ts3+.81;
elseif (700<=Ts3) && (Ts3<800)
    pl_reduce3=(-.25*10^-3).*Ts3+.25;
elseif (800<=Ts3) && (Ts3<1200)
    pl_reduce3=(-.125*10^-3).*Ts3+.15;
else Ts3>1200
    pl_reduce3=0;
end

if Ts3<100
    E_reduce3=1;
elseif (100<=Ts3) && (Ts3<500)
    E_reduce3=(-1.0*10^-3).*Ts3+1.1;
elseif (500<=Ts3) && (Ts3<600)
```

www.manaraa.com

```
    E_reduce3=(-2.9*10^-3).*Ts3+2.05;
elseif (600<=Ts3) && (Ts3<700)
    E_reduce3=(-1.8*10^-3).*Ts3+1.39;
elseif (700<=Ts3) && (Ts3<800)
    E_reduce3=(-.4*10^-3).*Ts3+.41;
elseif (800<=Ts3) && (Ts3<1200)
    E_reduce3=(-.225*10^-3).*Ts3+.27;
else Ts3>1200
    E_reduce3=0;
end

 if Ts4<600
    cs4=425+0.773.*Ts4-.00169.*(Ts4).^2+(2.22*10^-6).*(Ts4).^3;
elseif (600<=Ts4) && (Ts4<735)
    cs4=666+13002/(738-Ts4);
elseif (735<=Ts4) && (Ts4<900)
    cs4=545+17820/(Ts4-731);
else
    cs4=650;
 end

if Ts4<800
    ks4=54-0.0333.*Ts4;
else
    ks4=27.3;
end

if Ts4<400
    ys_reduce4=1;
elseif (400<=Ts4) && (Ts4<500)
    ys_reduce4=(-2.2*10^-3).*Ts4+1.88;
elseif (500<=Ts4) && (Ts4<600)
    ys_reduce4=(-3.1*10^-3).*Ts4+2.33;
elseif (600<=Ts4) && (Ts4<700)
    ys_reduce4=(-2.4*10^-3).*Ts4+1.91;
elseif (700<=Ts4) && (Ts4<800)
    ys_reduce4=(-1.2*10^-3).*Ts4+1.07;
elseif (800<=Ts4) && (Ts4<900)
    ys_reduce4=(-500*10^-6).*Ts4+.51;
elseif (900<=Ts4) && (Ts4<1200)
    ys_reduce4=(-200*10^-6).*Ts4+.24;
else Ts4>1200
    ys_reduce4=0;
end

if Ts4<100
    pl_reduce4=1;
elseif (100<=Ts4) && (Ts4<200)
    pl_reduce4=(-1.93*10^-3).*Ts4+1.193;
elseif (200<=Ts4) && (Ts4<300)
    pl_reduce4=(-1.94*10^-3).*Ts4+1.195;
elseif (300<=Ts4) && (Ts4<400)
    pl_reduce4=(-1.93*10^-3).*Ts4+1.192;
elseif (400<=Ts4) && (Ts4<500)
```

www.manaraa.com

```
     pl_reduce4=(-0.6*10^-3).*Ts4+0.66;
 elseif (500<=Ts4) && (Ts4<600)
     pl_reduce4=(-1.8*10^-3).*Ts4+1.26;
 elseif (600<=Ts4) && (Ts4<700)
     pl_reduce4=(-1.05*10^-3).*Ts4+.81;
 elseif (700<=Ts4) && (Ts4<800)
     pl_reduce4=(-.25*10^-3).*Ts4+.25;
 elseif (800<=Ts4) && (Ts4<1200)
     pl_reduce4=(-.125*10^-3).*Ts4+.15;
 else Ts4>1200
     pl_reduce4=0;
 end

 if Ts4<100
     E_reduce4=1;
 elseif (100<=Ts4) && (Ts4<500)
     E_reduce4=(-1.0*10^-3).*Ts4+1.1;
 elseif (500<=Ts4) && (Ts4<600)
     E_reduce4=(-2.9*10^-3).*Ts4+2.05;
 elseif (600<=Ts4) && (Ts4<700)
     E_reduce4=(-1.8*10^-3).*Ts4+1.39;
 elseif (700<=Ts4) && (Ts4<800)
     E_reduce4=(-.4*10^-3).*Ts4+.41;
 elseif (800<=Ts4) && (Ts4<1200)
     E_reduce4=(-.225*10^-3).*Ts4+.27;
 else Ts4>1200
     E_reduce4=0;
 end

end
```

Published with MATLAB® R2015a

www.manaraa.com